General Disclaimer

One or more of the Following Statements may affect this Document

- This document has been reproduced from the best copy furnished by the organizational source. It is being released in the interest of making available as much information as possible.

- This document may contain data, which exceeds the sheet parameters. It was furnished in this condition by the organizational source and is the best copy available.

- This document may contain tone-on-tone or color graphs, charts and/or pictures, which have been reproduced in black and white.

- This document is paginated as submitted by the original source.

- Portions of this document are not fully legible due to the historical nature of some of the material. However, it is the best reproduction available from the original submission.

DEPARTMENT OF MECHANICAL ENGINEERING AND MECHANICS
SCHOOL OF ENGINEERING
OLD DOMINION UNIVERSITY
NORFOLK, VIRGINIA

DEVELOPMENT OF A NONLINEAR VORTEX METHOD

By

Osama A. Kandil, Principal Investigator

Progress Report
For the period October 1, 1981 to March 31, 1982

Prepared for the
National Aeronautics and Space Administration
Langley Research Center
Hampton, Virginia

Under
Research Grant NSG 1560
E. Carson Yates, Jr., Technical Monitor
Structures and Dynamics Division

June 1982

DEPARTMENT OF MECHANICAL ENGINEERING AND MECHANICS
SCHOOL OF ENGINEERING
OLD DOMINION UNIVERSITY
NORFOLK, VIRGINIA

DEVELOPMENT OF A NONLINEAR VORTEX METHOD

By

Osama A. Kandil, Principal Investigator

Progress Report
For the period October 1, 1981 to March 31, 1982

Prepared for the
National Aeronautics and Space Administration
Langley Research Center
Hampton, Virginia 23665

Under
Research Grant NSG 1560
E. Carson Yates, Jr., Technical Monitor
Structures and Dynamics Division

Submitted by the
Old Dominion University Research Foundation
P.O. Box 6369
Norfolk, Virginia 23508-0369

June 1982

DEVELOPMENT OF A NONLINEAR VORTEX METHOD

By

Osama A. Kandil*

This semi-annual report covers the progress of the research work conducted under this grant from October 1, 1980 to March 31, 1981. During this period, the following tasks have been accomplished:

1. Development of the Modified Nonlinear Discrete Vortex (MNDV) method has been completed. The method is complemented by a viscous model for the vortex core based on the first-order boundary-layer-like equations. (Viscous analysis is supported under a separate contract from the Naval Air Development Center, Warminster, Pa.). The results of the inviscid and viscous methods have been reported in the AIAA paper No. 81-1263 titled "Recent Improvements in the Prediction of the Leading and Trailing Edge Vortex Cores of Delta Wings." A copy of this paper is enclosed in Appendix A. This paper has been submitted for publication in the Journal of Aircraft.

2. Development of the Nonlinear Hybrid-Vortex (NHV) method for wings with side-edge separation in steady and unsteady flows has been completed. The steady and unsteady results of this method have been reported in the AIAA paper No. 82-0351 titled "Steady and Unsteady Nonlinear Hybrid Vortex Method for Lifting Surfaces at Large Angles of Attack." A copy of this paper is also enclosed in Appendix A. This paper has been submitted for publication in the AIAA Journal.

3. The principal investigator has been invited as a lecturer in a short course on "Computational Methods in Potential Aerodynamics," organized by the International Center for Transportation Studies (ICTS) in Amalfi, Italy, in the period from May 31 to June 5, 1982. The lecture is titled "Steady and Unsteady Incompressible Free-Wake Analysis." The lecture covers the state of the art of free-wake analysis including a detailed presentation

---

*Associate Professor, Department of Mechanical Engineering and Mechanics, Old Dominion University, Norfolk, Virginia 23508.

of the work developed so far under this grant. A copy of the lecture is also included in Appendix A. The lecture will appear in the proceedings of the course, an ICTS publication.

The following tasks are to be completed by September 30, 1982:

1. The Inverse Hybrid-Vortex Method; Accurate Near-Field Calculations. For accurate near-field calculations in the MNDV method, the lumped vortex filaments, representing the wing and its wake, are redistributed on the corresponding surface panels. This modification guarantees the accuracy of the MNDV method and moreover maintains the efficiency of this method over the expensive panel methods. To eliminate any leapfrogging at the location of trailing-edge core and to expedite the convergence, functions of helical curves are used to fit the computed nodes of the free-vortex segments after each iteration cycle.

2. Steady and Unsteady Nonlinear Hybrid-Vortex Method for Leading-Edge Separation. The present NHV-method (covered in AIAA Paper No. 82-0351) is currently extended to treat wings with leading-edge separation. The computer code is very general; it can treat combined-edge separation (LE & TE), general planforms, and cambered wings. The solenoidal property of vorticity is also enforced across the edges of vortex panels. This eliminates (on the average, since the vorticity distribution is assumed to be linear) the discontinuity in the vorticity gradient.

3. The steady part of the NHV-method completed in item 2 will be used to develop the unsteady NHV-method for the frequency domain approach.

4. The NHV-method for bodies of revolution with prescribed separation lines is being completed.

Mr. Li-Chuan Chu is working on the NHV-method reported in items 2 and 3 above for his Ph.D. dissertation while Mr. Cheng is working on the NHV-method reported in item 4.

APPENDIX A

1. AIAA Paper No. 81-1263.

2. AIAA Paper No. 82-0351.

3. Lecture presented at the International School of Applied Aerodynamics, Amalfi, Italy, May 29-June 5, 1982.

AIAA-82-0351
Steady and Unsteady Nonlinear Hybrid Vortex Method for Lifting Surfaces at Large Angles of Attack

O.A. Kandil, L.C. Chu, and T. Tureaud,
Old Dominion Univ., Norfolk, VA

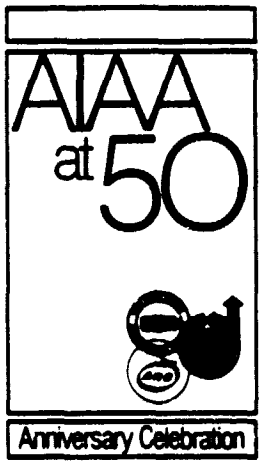

AIAA 20th Aerospace Sciences Meeting

January 11-14, 1982/Orlando, Florida

STEADY AND UNSTEADY NONLINEAR HYBRID VORTEX METHOD FOR LIFTING SURFACES AT LARGE ANGLES OF ATTACK†

Osama A. Kandil*, Li-Chuan Chu** and Thomas Tureaud**
Old Dominion University, Norfolk, VA. 23508

Abstract

Steady and unsteady Nonlinear Hybrid Vortex (NHV) method, for low aspect ratio wings at large angles of attack, is developed. The method uses vortex panels with first-order vorticity distribution (equivalent to second-order doublet distribution) to calculate the induced velocity in the near field using closed form expressions. In the far field, the distributed vorticity is reduced to concentrated vortex lines and the simpler Biot-Savart's law is employed. The method is applied to rectangular wings in steady and unsteady flows without any restriction on the order of magnitude of the disturbances in the flow field. The numerical results show that the method accurately predicts the distributed aerodynamic loads and that it is of acceptable computational efficiency.

I. Introduction and Background

In recent years, development of numerical methods for predicting the steady and unsteady aerodynamic characteristics of lifting surfaces exhibiting leading- and/or side-edge separations has received considerable attention.

For the steady-flow problems several numerical techniques have been developed. These include the Nonlinear Discrete-Vortex[1-6] (NDV) methods, high-order doublet panel methods[7-9] and Nonlinear Hybrid-Vortex (NHV) methods.[10-11] For the unsteady-flow problems, the literature shows fewer numerical techniques which include the NDV-methods[12-15] and constant doublet panel methods[16-17]. The literature lacks high-order panel methods for the unsteady flow problems.

For this reason and because of the success of the high-order panel methods in steady-flow problems, we are presenting in this paper an efficient and accurate method for the steady- and unsteady-flow problems of lifting surfaces at large angles of attack.

In this method, vortex panels with first-order vorticity distribution is used in the near-field calculations. In the far field calculations, the distributed vorticity over each far-field panel is lumped into equivalent concentrated vortex lines. In this way, accuracy is satisfied in the near field while computational efficiency is maintained in the far field. The coupling of a continuous vortex-sheet representation and a concentrated vortex-line representation for solving the nonlinear lifting-surface problem is called the "Nonlinear Hybrid Vortex (NHV)" method.

II. Formulation of the Problem

The problem is formulated relative to a wing-fixed frame of reference xyz. The x-axis is the wing centerline and the xy-plane is the wing plane of symmetry. The wing is rotating at the angular velocity $\bar{\Omega}$ and the freestream velocity is $\bar{U}_\infty$. The general orientation of the wing is described using the Eulerian angles α, β, and γ, figure 1, which refer to the angles of attack, yaw and roll; respectively. In terms of these angles and their time rate of change, the dimensionless freestream velocity and the angular velocity are expressed by

$$\bar{e}_\infty = \cos\alpha\cos\beta\,\bar{I} + (-\sin\alpha\cos\gamma + \cos\alpha\sin\beta\sin\gamma)\bar{J} + (\sin\alpha\sin\gamma + \cos\alpha\sin\beta\cos\gamma)\bar{k} \quad (1)$$

$$\bar{\Omega} = (-\dot{\alpha}\sin\beta + \dot{\gamma})\bar{I} + (\dot{\alpha}\cos\beta\sin\gamma + \dot{\beta}\cos\gamma)\bar{J} + (\dot{\alpha}\cos\beta\cos\gamma - \dot{\beta}\sin\gamma)\bar{k} = \Omega_x\bar{I} + \Omega_y\bar{J} + \Omega_z\bar{k} \quad (2)$$

where $\bar{I}$, $\bar{J}$ and $\bar{k}$ are the base unit vectors of the xyz-frame of reference .

The unsteady irrotational ideal flow in the region outside of the wing and its separated vortex sheets is governed by the Laplace's equation

$$\nabla^2\phi = 0 \quad (3)$$

where $\phi(\bar{r},t)$ is the perturbation velocity potential. The no-penetration condition on the wing $s(\bar{r},t)$, relative to the wing fixed frame of reference, is given by

$$\frac{\partial s}{\partial t} + (\bar{e}_\infty + \nabla\phi - \bar{\Omega}\times\bar{r})\cdot\nabla s = 0 \quad \text{on } s(\bar{r},t) = 0 \quad (4\text{-a})$$

For a rigid wing, $\frac{\partial s}{\partial t} = 0$ and equation (4-a) reduces to

$$(\bar{e}_\infty + \nabla\phi - \bar{\Omega}\times\bar{r})\cdot\bar{n}_s = 0 \quad \text{on } s(\bar{r}) = 0 \quad (4\text{-b})$$

On the separated free-vortex sheet $w(\bar{r},t)$, the no-penetration condition is given by

$$\frac{\partial w}{\partial t} + (\bar{e}_\infty + \nabla\phi - \bar{\Omega}\times\bar{r})\cdot\nabla w = 0 \quad \text{on } w(\bar{r},t) = 0 \quad (5)$$

The no-pressure jump condition on $w(\bar{r},t)$ is obtained from the unsteady Bernoulli's equation

$$C_p(\bar{r},t) = -\nabla\phi\cdot[\nabla\phi + 2(\bar{e}_\infty - \bar{\Omega}\times\bar{r})] - 2\frac{\partial\phi}{\partial t} \quad (a)$$

where $C_p(\bar{r},t)$ is the pressure coefficient at any point $\bar{r}$ and at any time t. Forming the pressure jump from equation (a) and equating the result to zero, we obtain

$$\Delta C_p = C_{p_1} - C_{p_2} = -(\nabla\phi_1 - \nabla\phi_2)\cdot[\nabla\phi_1 + \nabla\phi_2 + 2(\bar{e}_\infty - \bar{\Omega}\times\bar{r})] - 2\frac{\partial(\phi_1 - \phi_2)}{\partial t} = 0 \quad (b)$$

† This research work is supported by NASA Langley Research Center under Grant No. NSG 1560 and by the Naval Air Development Center under Contract No. N62269-80-C-0704.

* Associate Professor of Mechanical Engineering and Mechanics, AIAA Member
** Graduate Research Assistant, AIAA Member

where the subscripts 1 and 2 refer to the upper and lower surfaces of the wing; respectively. Rearranging equation (b) and setting

$$\phi_1 - \phi_2 = \Delta\phi \qquad (c)$$

one obtains

$$\Delta C_p = -2\left(\frac{\partial}{\partial t} + \bar{v}_w \cdot \nabla\right)(\Delta\phi) = -2\,\frac{D(\Delta\phi)}{Dt} = 0 \qquad (d)$$

where $\bar{v}_w$ = velocity of a wake element relative to the xyz-frame of reference

$$= \frac{1}{2}\,(\nabla\phi_1 + \nabla\phi_2) + \bar{e}_\infty - \bar{\Omega}\times\bar{r}$$

Equation (d) represents the theorems of Kelvin and Helmholtz

$$\frac{D\Gamma}{Dt} = \frac{D}{Dt}\iint \bar{\omega}\cdot\bar{n}_A\, dA = 0 \quad \text{on } w(\bar{r},t) = 0 \qquad (6)$$

of conservation of the circulation and the outflow of vorticity; respectively. In equation (6), $\bar{n}_A$ is a unit normal to the surface A bounded by a closed curve around which the circulation Γ is calculated. Equation (6) simply states that the rate of change of circulation around a closed curve or the rate of change of outflow of vorticity through the surface bounded by this closed curve is zero (following the same fluid particles.)

For uniqueness of the solution, one has to impose the Kutta condition along the edges of separation. Here, Kutta condition is represented by

$$\Delta C_p \Big|_{TE,LE,SE} = 0 \qquad (7)$$

Finally, the infinity condition requires that

$$\nabla\phi \to 0 \quad \text{away from s and w} \qquad (8)$$

Equation (1) - (8) are the required equations for the general unsteady flow problem.

III. Nonlinear Hybrid-Vortex Method for Steady Flows

III.1. Governing Equations

The research effort in this paper is concentrated on the symmetric-flow problems. For a steady-symmetric flow, the governing equations are obtained from the general equation (1) - (8) by setting $\bar{\Omega} = 0$, $\beta = \gamma = 0$ and dropping the time dependent terms. The resulting equations are

$$\bar{e}_\infty = \cos\alpha\,\bar{I} - \sin\alpha\,\bar{J} \qquad (9)$$

$$\nabla^2\phi = 0 \qquad (10)$$

$$(\bar{e}_\infty + \nabla\phi)\cdot\bar{n}_s = 0 \qquad \text{on } s(\bar{r}) = 0 \qquad (11)$$

$$(\bar{e}_\infty + \nabla\phi)\cdot\bar{n}_w = 0 \qquad \text{on } w(\bar{r}) = 0 \qquad (12)$$

$$\Delta C_p = -2(\bar{n}_w\times\bar{\omega})\cdot(\bar{e}_\infty + \nabla\phi) = 0 \qquad \text{on } w(\bar{r}) = 0 \qquad (13)$$

$$\Delta C_p \Big|_{TE,LE,SE} = 0 \qquad (14)$$

$$\nabla\phi \to 0 \quad \text{away from s and w} \qquad (15)$$

III.2. Method of Solution of the Steady Flow Problem

Equation (12) requires the flow to be tangent to w while equation (13) requires this tangential flow to be parallel to the vorticity direction. Therefore, if the flow direction is forced to be parallel to the vorticity direction on the surface w, the boundary conditions of equations (12) and (13) are automatically satisfied. Next, we outline the method of solution.

Once the wing and its free-shear layers are represented by vortex sheets, equations (10) and (15) are automatically satisfied. The basic unknowns in the present problem are the vorticity distribution ω and the free-vortex sheet w. They are determined by satisfying the remaining boundary conditions, equations (11)-(14), through a finite-element type approach.

In this approach, the bound-vortex sheet (representing the wing) is divided into quadrilateral bound-vortex panels while the free-vortex sheets (representing the free-shear layers) are divided into triangular free-vortex panels, see figure 2. On each vortex panel (bound or free), a local vorticity distribution with undetermined coefficients is defined in a local-coordinate system. The local distribution is selected such that the solenoidal property of vorticity is satisfied. The continuity of vorticity (a compatibility condition) is enforced at certain nodes on the interelement boundaries of adjacent panels.

The remaining boundary conditions, equations (11)-(14), are enforced at certain nodes of the vortex panels to obtain the undetermined coefficents of the local vorticity distribution and the shape of the free-vortex panels. Kutta condition, equation (14), is enforced at the nodes of the bound-vortex panels along the edges of separation. The no-penetration condition, equation (11), is enforced at the average points of the bound-vortex panels. The no-penetration and no-pressure-jump conditions, equations (12) and (13), are simultaneously satisfied at the nodes of the free-vortex panels.

To satisfy these conditions, an iterative technique is followed which alternatively yields the local vorticity distribution on the bound-vortex panels and the shape of the free-vortex panels. During a typical iterative cycle, an overdetermined set of algebraic equations are solved for the undetermined coefficients of the local vorticity distributions. This is followed by adjusting the surface w such that $\bar{\omega}$ and $(\bar{e}_\infty + \nabla\phi)$ at the nodes of the free-vortex panels become parallel. The overdetermined set of equations consists of the equations obtained from the continuity of vorticity condition, Kutta condition, the no-penetration condition on the wing, and a symmetry condition applied at the nodes along the line of symmetry. This set is solved by a least-square technique.

Once the iterative technique converges, the pressure distribution is calculated and this is followed by calculating the total aerodynamic characteristics. Convergence of the technique is expedited by using an initial guess for w provided by the Nonlinear Discrete-Vortex method[4-6] (NDV-method).

In the next subsections, the basic equations required at each step of the solution are given.

III.2.1. Quadrilateral Panel

Quadrilateral vortex panels are used to represent the bound-vortex sheet. On each panel, a local first-order vorticity distribution is specified. For the kth panel, the vorticity distribution is given by

$$\omega_\zeta(k) = a_1(k) + a_2(k)\,\zeta(k) + a_3(k)\,\xi(k) \tag{16}$$

$$\omega_\xi(k) = -a_2(k)\,\xi(k) - a_4(k) - a_5(k)\,\zeta(k) \tag{17}$$

which contain five undetermined coefficients; a_1-a_5. It should be noted that a first order vorticity distribution is equivalent to a second-order doublet distribution. The distributions given by equations (16) and (17) satisfy the solenoidal property of $\bar{\omega}$

$$\nabla \cdot \bar{\omega} = 0 \tag{18}$$

The four corners of the panel serve as nodal points where continuity of vorticity condition, Kutta condition, and/or symmetry condition are satisfied. The ζ and ξ axes are located in the panel plane such that the ζ- axis coincides with the 1-4 side of the panel. The η-axis is perpendicular to the panel such that ζ, ξ, and η axes form a right-handed local coordinate system. The average point of the four nodes serves as the control point where the no-penetration condition is enforced, see figure 3a.

In the near-field, the induced velocity at any field point $\hat{x}$, $\hat{y}$, $\hat{z}$ is calculated by

$$\bar{v}(\hat{x},\hat{y},\hat{z}) = \frac{-1}{4\pi}\sum_{i=1}^{2,3}\int_{\zeta_i}^{\zeta_{i+1}}\int_{0}^{\xi(\zeta)} \frac{\hat{y}\,\omega_\zeta\bar{e}_\xi + [(\hat{z}-\zeta)\omega_\xi - (\hat{x}-\xi)\omega_\zeta]\bar{e}_\eta - \hat{y}\omega_\xi\,\bar{e}_\zeta}{[(\hat{x}-\xi)^2+\hat{y}^2+(\hat{z}-\zeta)^2]^{3/2}}\,d\xi\,d\zeta \tag{19}$$

where the summation over i indicates that the panel is divided into two (in the case of a triangular panel, see sec. III.2.2.) or three subpanels. Substituting equations (16) and (17) into equation (19), we integrate the resulting expression in the ξ-direction analytically. The resulting equations are given in Appendix A. The integration in the ζ-direction is performed numerically. Currently, complete analytical integrations in both directions are developed, Appendix B.

In the far-field, the vorticity distribution is lumped into concentrated vortex lines and the simpler Biot-Savart's law is used to calculate the induced velocity. The locations of the concentrated vortex lines are the lines connecting the mid-points of opposite sides of the panel. The far-field equation of the induced velocity is given by

$$\bar{V} = \frac{\Gamma_\zeta}{4\pi h_\zeta}(\cos\theta_{1\zeta} + \cos\theta_{2\zeta})\bar{e}_{v\zeta} + \frac{\Gamma_\xi}{4\pi h_\zeta}(\cos\theta_{1\xi} + \cos\theta_{2\xi})\bar{e}_{v\xi} \tag{20}$$

where

$$\Gamma_\zeta = (\bar{\omega}_\zeta \sin\gamma_2 - \bar{\omega}_\xi \cos\gamma_2)\ell_2/(\cos\gamma_1 \sin\gamma_2 - \sin\gamma_1 \cos\gamma_2) \tag{21}$$

$$\Gamma_\xi = (\bar{\omega}_\xi \cos\gamma_1 - \bar{\omega}_\zeta \sin\gamma_1)\ell_1/(\cos\gamma_1 \sin\gamma_2 - \sin\gamma_1 \cos\gamma_2) \tag{22}$$

$$\bar{\omega}_\zeta = \frac{1}{A}\sum_{i=1}^{3}\int_{\zeta_i}^{\zeta_{i+1}}\int_{0}^{\xi(\zeta)} \omega_\zeta\,d\zeta\,d\xi \tag{23}$$

$$\bar{\omega}_\xi = \frac{1}{A}\sum_{i=1}^{3}\int_{\zeta_i}^{\zeta_{i+1}}\int_{0}^{\xi(\zeta)} \omega_\xi\,d\zeta\,d\xi \tag{24}$$

and A is the panel area. Figure 3.b. shows the different parameters used in equations (20) - (22).

III.2.2. Triangular Panels

Triangular panels model nonplanar and twisted surfaces more accurately than quadrilateral planar panels. Therefore, they are used to represent the free-vortex sheets where highly nonplanar and twisted surfaces are encountered. The local vorticity distributions are still given by equations (16) and (17). The corners of this panel serve as nodal points where certain boundary conditions are enforced. The ζ-axis coincides with the 1-3 side of the panel, the ξ- axis is in the panel plane, and the η-axis is perpendicular to the panel such that ζ, ξ, and η axes form a right-handed local coordinate system, figure 4a.

In the near field, the induced velocity at any point is given by equation (19), where k = 1,2. In the far field, the vorticity distribution on the panel is lumped into concentrated vortex lines so that Biot-Savart's law can be used to calculate the induced velocity. The locations of the two concentrated vortex lines are chosen to be the line connecting the midpoints of sides 1-2 and 2-3 and the line connecting node 2 to the midpoint of side 1-3. The far-field equations of the induced velocity are given by equations (20)-(24), where $\gamma_1 = 0$ and k = 1,2.

III.2.3. Boundary Conditions

At each control point of the bound-vortex panels, we satisfy equation (11). For the mth control point (a receiver panel), equation (11) gives

$$\sum_{k=1}^{N} \bar{v}(m,k)\cdot\bar{n}_s(m) = -\bar{e}_\infty\cdot\bar{n}_s(m) \tag{25}$$

where N is the total number of bound- and free-vortex panels (k refers to a sender panel), and

$$\bar{v}(m,k) = \sum_{j=1}^{5}[\bar{u}_j(m,k)\bar{e}_\xi(k) + \bar{v}_j(m,k)\bar{e}_\eta(k) + \bar{w}_j(m,k)\bar{e}_\zeta(k)]a_j(m,k) \tag{26}$$

The coefficients of $\tilde{u}_j$, $\tilde{v}_j$, and $\tilde{w}_j$ are given by the equations of Appendix (A) or Appendix (B).

The unit normal $\bar{n}_s(m)$ of a bound-vortex panel and the base-unit vectors $\bar{e}_\xi(k)$, $\bar{e}_\eta(k)$ and $\bar{e}_\zeta(k)$ of the local coordinates of the k th strip panel (bound or free) are expressed in terms of the base-unit vectors of the global wing-fixed coordinate system $\bar{I}$, $\bar{J}$ and $\bar{K}$ as follows:

$$\bar{n}_s(m) = d_{nx}(m)\,\bar{I} + d_{ny}(m)\,\bar{J} + d_{nz}(m)\,\bar{K} \qquad (27)$$

$$\bar{e}_\xi(k) = d_{\xi x}(k)\,\bar{I} + d_{\xi y}(k)\,\bar{J} + d_{\xi z}(k)\,\bar{K}$$

$$\bar{e}_\eta(k) = d_{nx}(k)\,\bar{I} + d_{ny}(k)\,\bar{J} + d_{nz}(k)\,\bar{K} \qquad (28)$$

$$\bar{e}_\zeta(k) = d_{\zeta x}(k)\,\bar{I} + d_{\zeta y}(k)\,\bar{J} + d_{\zeta z}(k)\,\bar{K}$$

where d refer to the direction cosine .

Substituting equation (28) into (26) and substituting the resulting equation and equation (27) into equation (25), the no-penetration at any mth point reduces to

$$\sum_{k=1}^{N}\sum_{j=1}^{5} \begin{Bmatrix} d_{nx} \\ d_{ny} \\ d_{nz} \end{Bmatrix}_m^T \begin{bmatrix} d_{\xi x} & d_{nx} & d_{\zeta x} \\ d_{\xi y} & d_{ny} & d_{\zeta y} \\ d_{\xi z} & d_{nz} & d_{\zeta z} \end{bmatrix}_k \begin{Bmatrix} \tilde{u}_j \\ \tilde{v}_j \\ \tilde{w}_j \end{Bmatrix}_{m,k}$$

$$a(j,k) = -\begin{Bmatrix} \cos\alpha \\ -\sin\alpha \\ 0 \end{Bmatrix}^T \begin{Bmatrix} d_{nx} \\ d_{ny} \\ d_{nz} \end{Bmatrix}_m \qquad (29)$$

It should be noted here that the number of unknown coefficients a(j,k) are reduced from 5N (5x total number of bound- and free-vortex panels) to 5 N_b (5x total number of bound-vortex panels) by equating the outflow of vorticity from the bound-vortex panels to the inflow of vorticity into the free-vortex panels along the separation edges. Moreover, the vorticity vector is aligned with one side of the triangular free-vortex panels. Once this is accomplished, the free argument m has the range 1 to N_b and thus we obtain N_b unknowns.

In addition, we write equations of vorticity continuity at each common node of the bound-vortex panels. A typical couple of equations written at the (I+1,J) global node, corresponding to the two local nodes (2,k) and (1,k+1) between panels number k and k+1 is given by (see figure 9)

$$\begin{aligned} \omega_z(I+1,J) &= \omega_\zeta(2,k)d_{\zeta z}(k) + \omega_\xi(2,k)d_{\xi z}(k) \\ &= \omega_\zeta(1,k+1)d_{\zeta z}(k+1) + \omega_\xi(2,k+1)d_{\xi z}(k+1) \end{aligned} \qquad (30)$$

$$\begin{aligned} \omega_x(I+1,J) &= \omega_\zeta(2,k)d_{\zeta x}(k) + \omega_\xi(2,k)d_{\xi x}(k) \\ &= \omega_\zeta(1,k+1)d_{\zeta x}(k+1) + \omega_\xi(1,k+1)d_{\xi x}(k+1) \end{aligned}$$

where ω_ξ and ω_ζ are expressed in terms of the undetermined coefficients a(j,k) using equations (16) and (17).

Kutta condition, equation (14), is satisfied at the nodes of bound-vortex panels along the edges of separation. At a typical global node (I+2,J), equation (14) gives

$$\omega_x(I+2,J)\,v_z(I+2,J) - \omega_z(I+2,J)\,v_x(I+2,J) = 0 \qquad (31)$$

Since ω_x, ω_z, v_x and v_z are functions of the undermined coefficients, equation (31) is a nonlinear equation in a(j,k). Adding equations of this type to equations (29) and (31) disturbs the linearity of the resulting set of equations. Therefore, we enforce equation (31) in a linearized approach. We divide equation (31) by v(I+2,J) and let

$$v_z(I+2,J)/v(I+2,J) = \cos\beta(I+2,J)$$

$$\text{and } v_x(I+2,J)/v(I+2,J) = \sin\beta(I+2,J) \qquad (32)$$

Thus, equation (32) becomes

$$\omega_x(I+2,J)\cos\beta(I+2,J) - \omega_z(I+2,J)\sin\beta(I+2,J) = 0 \qquad (33)$$

Assuming that $\beta(I+2,J)$ is initially known, equation (33) becomes a linear equation in a(m). In the subsequent iterative steps, the angle β is calculated by equations (32) using the m values of the preceding iterative step.

The last set of linear equations are obtained from the symmetry condition (for symmetric flow) along the root chord. A typical symmetry condition written at a global node $(\hat{I},\hat{J})$, corresponding to a local node $(1,\hat{k})$, is given by

$$\omega_x(\hat{I},\hat{J}) = \omega_\zeta(1,\hat{k})d_{\zeta x}(\hat{k}) + \omega_\xi(1,\hat{k})d_{\xi x}(\hat{k}) = 0 \qquad (34)$$

The resulting set of equations obtained from equations (29), (30), (33) and (34) are solved for the coefficients a(m) by a least square solver (overdetermined set of equations).

Once the coefficients are determined, equations (12) and (13) are enforced by aligning sides 1-3 of the triangular free-vortex panels with the local flow directions. Equations of the following form are used to calculate the new global downstream nodes of these sides:

$$\begin{aligned} x(L+1,J) &= x(L,J) + \bar{b}v_{mx}(L,J)/v_m(L,J) \\ y(L+1,J) &= y(L,J) + \bar{b}v_{my}(L,J)/v_m(L,J) \\ z(L+1,J) &= z(L,J) + \bar{b}v_{mz}(L,J)/v_m(L,J) \end{aligned} \qquad (35)$$

where (L,J) and (L+1,J) refer to the upstream and downstream nodes of side (1-3), $\bar{b}$ is the length of this side, and v_m is the velocity calculated at the upstream node (L,J).

III.2.4. Pressure Distribution

The net-pressure coefficient is calculated at the no-penetration control point of a bound-vortex

panel. At the m th control point, the net-pressure coefficient is given by

$$\Delta C_p(m) = 2(\omega_x(m) \sum_{k=1}^{N} v_z(m,k) - \omega_z(m)[\sum_{k=1}^{N} v_x(m,k) + \cos\alpha]) \quad (36)$$

where $\omega_x(m) = \omega_\zeta(m)d_{\zeta x}(m) + \omega_\xi(m)d_{\xi x}(m)$

$$\omega_z(m) = \omega_\zeta(m)d_{\zeta z}(m) + \omega_\xi(m)d_{\xi z}(m)$$

Equations (16), (17), and (26) give ω_ξ, ω_ζ and v in terms of the coefficients a. The normal force coefficient is then calculated by

$$C_n = \sum_{m=1}^{N_b} \Delta C_p(m)\, A(m) / \sum_{m=1}^{N_b} A(m) \quad (37)$$

where A(m) is the area of m th panel. A more accurate calculation of C_n is obtained by fitting a surface to discrete of values of $\Delta C_p(m)$. The resulting function $\Delta C_p(x,z)$ is then used to obtain

$$C_n = \iint_A \Delta C_p(x,z)\, dA / \iint_A dA \quad (38)$$

IV.1. Nonlinear Hybrid-Vortex Method for Unsteady Flows

For unsteady symmetric flow, we set $\beta = \gamma = \delta = \varepsilon = 0$ in equations (1) and (2). The resulting equations are

$$\bar{e}_\infty = \cos\alpha\, \bar{I} - \sin\alpha\, \bar{J} \quad (39)$$

$$\bar{\Omega} = \Omega_z \bar{k} = \dot{\alpha}\, \bar{k} \quad (40)$$

$$\nabla^2\phi = 0 \quad (41)$$

$$(\bar{e}_\infty + \nabla\phi - \bar{\Omega}_z \times \bar{r}) \cdot \bar{n}_s = 0 \qquad \text{on } s(\bar{r})=0 \quad (42)$$

$$\frac{\partial w}{\partial t} + (\bar{e}_\infty + \nabla\phi - \bar{\Omega}_z \times \bar{r}) \cdot \nabla w = 0 \qquad \text{on } w(\bar{r},t)=0 \quad (43)$$

$$\frac{D\Gamma}{Dt} = 0 \qquad \text{on } w(\bar{r},t)=0 \quad (44)$$

$$\Delta C_p \Big|_{TE,LE,SE} = 0 \quad (45)$$

$$\nabla\phi \to 0 \qquad \text{away from s and w} \quad (46)$$

IV.2. Method of Solution of the Unsteady-Flow Problem

The source of flow unsteadiness in this problem can be a time dependent angle of attack or a time-dependent freestream speed, Figure 6. In the time domain approach of this problem, we divide the function of angle of attack into discrete changes in the angle of attack corresponding to discrete changes in time; i.e., at $t=t_0$, $\alpha=\alpha_0$ and at $t=t_0 + \Delta t$, $\alpha_0+\Delta\alpha$ etc. The problem is then solved at each time step where the solution of the preceding time step serves as the initial condition for the present time step.

This approach can treat problems where the flow unsteadiness starts (at $t = t_0$) from a steady flow or where the flow unsteadiness starts impulsively from rest. The former problem initially requires the steady-flow solution to be known; equations (9)-(15), while the latter problem initially requires the solution of the flow over a wing without a wake surface.

Once the initial condition is obtained, we march step by step in time satisfying equations (42) - (45). At each time step, the basic unknowns $w(\bar{r},t)$ and $w(\bar{r},t)$ are obtained.

Next, we discuss the boundary conditions and the calculations of the pressure distribution at each step.

IV.2.1. Boundary Conditions

Although the developed time-domain technique is a general one and moreover is not restricted to any particular source of flow unsteadiness, the case of an impulsively started wing from rest is considered for the purpose of explaining the details of the technique. In this case, we set $\alpha=0$ and replace $\bar{e}_\infty$ by $-\bar{e}_\infty$ in equations (39), (40) and (42)-(45). The following steps explain the procedure to enforce the boundary conditions of equations (42)-(45) and to obtain $w(\bar{r},t)$ and $w(\bar{r},t)$:

a. The initial condition, at $t=t_0$, is considered to be a wing without a wake surface having a velocity of $-\bar{e}_\infty$. At this instant, we assume that not enough time has passed for the vorticity to be convected from the separation edges. The initial vorticity distribution on the wing $w(\bar{r},t)$ is obtained from the least-square solution of an over-determined set of linear algebraic equations in the unknown coefficients (a). The set of equations consists of the no-penetration conditions, equation (42), the continuity of vorticity conditions, equation(30), the Kutta conditions, equation (45), and the symmetry conditions, equation (34).

It should be noted that the initial vorticity distribution on the wing is such that the circulation around any closed curve embracing a wing section or equivalently the outflow of vorticity from a surface enclosed by this curve is zero. Consequently, a starting vortex of opposite strength to that of the vorticity on the wing develops at the edges of separation. The starting vortex is then convected downstream with the local particle velocity, the flow existing at the preceding instant is disturbed, and the vorticity distribution on the wing changes creating a new starting vortex to be downstream.

This process continues and by the end of the first time step, at $t=t_0+\Delta t$, a free-vortex strip, consisting of triangular free-vortex panels attached to the separation edges, is created. The free-vortex strip obeys the conditions given by equations (43) and (44) and its upstream edge satisfies Kutta condition at the separation edges, equation (45).

b. At $t=t_0+\Delta t$, one needs $\bar{v}(\bar{r},t_0+\Delta t)$ to determine the width of the vortex strip. Since this velocity is unknown so far, a good estimate is taken as the velocity at the preceding time step $\bar{v}(r,t_0)$, which

is completely known from the solution corresponding to the initial condition. Within the time step Δt, the displacement $\Delta\bar{r}$ of any panel node is found from

$$\Delta\bar{r} = \bar{r}(t_o + \Delta t) - \bar{r}(t_o) = \Delta t \cdot \bar{v}(\bar{r},t_o) \qquad (47)$$

where

$$\bar{v}(\bar{r},t_o) = -\bar{e}_\infty + \nabla\phi(\bar{r},t_o)$$

($\dot{a}$=o for the considered case) (48)

$$\nabla\phi(\bar{r},t_o) = \sum_{k=1}^{N_b} \bar{v}_k(\bar{r},t_o) \qquad (49)$$

$\bar{v}_k(\bar{r},t_o)$ is given by equation (19) (50)

and N_b is the total number of panels on the wing.

At $t=t_o+\Delta t$, one also needs the vorticity of the triangular vortex panels forming the free-vortex strip, $\bar{\omega}(\bar{r},t_o+\Delta t)$. For each triangular panel, we express its five unknown coefficients (a_1)-(a_5), describing its linear vorticity distribution, in terms of the five unknown coefficients of the adjacent bound-vortex panel, at the separation edges, at $t=t_o$ (a_1-a_5 of the bound panel are already known) and at $t=t_o+\Delta t$ (a_1-a_5 of the bound panel are still unknown). This is achieved by satisfying the following conditions. At $t=t_o+\Delta t$, the vorticity is continuous at the global nodes (on the separation edge) between the bound- and free-vortex panels. At $t=t_o+\Delta t$, the fluid particles along the downstream edges of the triangular panels are the same particles which existed at the edge of separation at $t=t_o$. According to Helholtz theorem $[\frac{D\bar{\omega}}{Dt} = (\bar{\omega}\cdot\nabla)\bar{v}]$, the vorticity of these particles changes as they are convected downstream. But according to Kelvin theorem ($\frac{D\Gamma}{Dt} = o$), the circulation around these particles remains constant and hence additional equations are written to satisfy Kelvin theorem between $t=t_o$ and $t=t_o+\Delta t$.

Next, the vorticity distribution on the wing $\bar{\omega}(r,t_o+\Delta t)$ is obtained from the overdetermined set of algebraic equations.

c. At $t=t_o+2\Delta t$, a new free-vortex strip is created along the separation edges, the first shed free-vortex strip is convected downstream under the condition $\frac{D\Gamma}{Dt} = o$, and step (b) is repeated to find the locations of the free-panels nodes and $\bar{\omega}(r,t_o+2\Delta t)$.

d. The steady state is reached once the change in the vorticity distribution is less than a prescribed error.

IV.2.2. Pressure Distribution

To calculate the net-pressure coefficient at any point on the wing surface r at any time $t_k = t_o + k\cdot\Delta t$, we apply the unsteady Bernoulli's equation

$$\Delta C_p(\bar{r},t_k) = -2\bar{V}_j(\bar{r},t_k)\cdot[\nabla\phi(\bar{r},t_k) + (\bar{e}_\infty - \bar{\omega}\times\bar{r})] - 2\frac{\partial\Delta\phi(\bar{r},t_k)}{\partial t} \qquad (51)$$

where $\bar{V}_j(\bar{r},t_k)$ is the jump in the tangential velocity across the wing, which is completely known from the vorticity vector at this location, $\bar{\omega}(\bar{r},t_k)$. The first term in the brackets $\nabla\phi(\bar{r},t_k)$ is calculated from equation (19). The last term on the right-hand side is calculated as follows:

$$\frac{\partial\Delta\phi(\bar{r},t_k)}{\partial t} = \frac{\Delta\phi(\bar{r},t_k) - \Delta\phi(\bar{r},t_{k-1})}{\Delta t} = \frac{\Gamma(\bar{r},t_k) - \Gamma(\bar{r},t_{k-1})}{\Delta t} \qquad (52)$$

V. Computer Program

A computer program is developed to implement the methods of solution of the steady and unsteady flow problems. The program is divided into three major parts and each part consists of several subroutines.

The first part deals with the wing geometry, wing panelling (bound-vortex panels) and wake panelling (free-vortex panels). Usage of initial wake panelling depends on the initial conditions of the unsteady problem. No wake panelling is considered if the unsteady problem starts from rest. For the unsteady problem with steady-state initial condition, wake panelling is considered. Several subruotines are used to generate the global and local coordinates of the panels and the direction cosines of the local coordinate systems.

The second part deals with the initial conditions. For the unsteady problem with steady-state initial condition, the steady-flow problem is initially solved. The boundary conditions on the bound- and free-vortex panels are satisfied (Section III.2.3.) through several subroutines. For $\bar{\omega}(F)$, these subroutines fill a rectangular matrix [N_{BC} (number of boundary-condition equations) x N_b (number of undetermined coefficients of the bound-vorticity distribution)] with the coefficients of the boundary-condition equations; no-penetration conditions, continuity of vorticity conditions, Kutta conditions, and symmetry conditions. The overdetermined set of equations is then solved using a least-square solver. For $W(\bar{r})$, the boundary conditions on the free-vortex panels are enforced using a separate subroutine. Once the boundary conditions are satisfied, the net-pressure coefficients are calculated as given in Section III.2.4. If the initial condition is rest, the problem is solved without any free-vortex panels.

The third part of the program deals with the problem at $t > t_o$. Several subroutines are used to satisfy the boundary conditions (Section IV.2.1.) at the subsequent time steps $t_k=t_o+k\cdot t$; k=1,2,... One subroutine is used to generate a new shed free-vortex strip and another subroutine is used to convect the previously shed free-vortex strips. The vorticity distribution of the panels forming the previously shed free-vortex strips

$\bar{\omega}_w(\bar{r},t_k)$ is found from another subroutine which enforces Kelvin theorem. The unknown vorticity coefficients of the panels forming the newly shed vortex-sheet strip are related to those coefficients of the wing panels existing at the separation edges.

Other subroutines are used to fill the matrix representing the wing boundary conditions; no-penetration condition, continuity of vorticity condition, unsteady Kutta condition and symmetry condition. The least-square solver is used to obtain the vorticity distribution at this time step, $\bar{\omega}(\bar{r},t_k)$.

The unsteady Bernoulli's equation, Equation (51), is then used through a separate subroutine to calculate the net-pressure coefficient. Figure 7 shows a flow chart of the computer program.

VI. Numerical Examples

VI.1. Steady Flow

The developed computer program is used to solve for the steady flow past a rectangular wing having side-edge separation. The wing is of aspect ratio of one at 9.7° angle of attack. The wing is divided into 6x6 quadrilateral bound-vortex panels, the trailing edge free-vortex sheet is divided into 6x6 quadrilateral free-vortex panels, and the side edge free-vortex sheet is divided into 6 vortex strips and each is divided into a different number of quadrilateral free-vortex panels such that the last panel in each strip occupy the same chordwise station as that of the last panel of the trailing edge free-vortex panel.

Figure 5 shows a typical converged solution of the spanwise and cordwise components of vorticity at the local nodes of the quadrilateral vortex panels. At any node, the upper number is the spanwise component ω_ζ and the lower number is the cordwise component ω_ξ. It is seen that the continuity of vorticity condition, Kutta condition and the symmetry condition are satisfied at the common nodes, at the nodes of the trailing and side edges, and at the notes of the line of symmetry; respectively.

Figure 9 shows the spanwise variation of the section normal-force coefficient at three iteration steps. The solution converges in the third iteration step and is in good agreement with the experimental data of Scholtz[18]. The figure also shows the solution of the same case obtained by the NDV-method with 6x6 bound-vortex lines. One can conclude that the NDV-method underestimates the normal-force coefficient near the wing tip. If the number of bound-vortex lines of the NDV-method is increased to 9x7[4], the solution agrees with that obtained by the NHV-method with 6x6 bound-vortex panels. This clearly shows that a less number of vortex panels gives the same accuracy as that obtained by a large number of bound-vortex lines.

Figure 10 shows the converged solution of the spanwise variation of the section pitching-moment coefficient for the wing. The results of the NDV-method with 6x6 and 9x7 bound-vortex lines are also included in the figure.

Figure 11 shows the spanwise variation of the net-pressure coefficient at different chord stations with different number of panels for a rectangular wing at 15° angle of attack. The corresponding results of the NDV-method are also shown in the figure.

The present computer program is computationally efficient when it is compared with other existing codes which use high-order doublet distribution. The CPU time on the CYBER 175 for this case is about 200 seconds.

VI.2. Unsteady Flow

Next, the developed computer program is used to solve for the unsteady flow past impulsively started wings from rest without side edge separation. In the two examples, the wing is divided into 5x5 quadrilateral bound-vortex panels with a sine distribution in the chordwise direction and a cosine distribution in the spanwise direction. In the present cases, the dimensionless time step is equivalent to 0.48 while the root-chord length is 5 units.

Figure 12 shows the distribution of the lift coefficient for a rectangular wing of aspect ratio of three at 5° angle of attack for t=2 and t=22. The present results are compared with the steady numerical data of reference (19) where 196 panels of constant potential function are used. It is also compared with the experimental data of Reference (20). Although we used 25 panels in the present case, the results compares well with the other numerical and experimental data.

Figure 13 compares the growth of indicial lift for the same wing considered above with the numerical data of reference (17) where 100 panels of constant doublets are used.

Although we used 25 panels in the present case the results compare well with the other numerical data.

Figure 14 shows the distribution of net pressure coefficient for a rectangular wing of aspect ratio of two at 20.5° angle of attack for t=2, 10, 21 and 22. On the CYBER 175 computer, the CPU time for each case with 5x5 bound panels and 22 time steps is about 10 minutes.

Currently, work is underway to increase the number of panels, use the efficient far field calculations, and calculate cases with side- and leading-edge separations.

VII. Concluding Remarks

Steady and unsteady Nonlinear Hybrid Vortex Method for low aspect ratio wings at large angles of attack is developed. The method uses vortex panels with first-order vorticity distribution (equivalent to second-order doublet distribution) in the near field calculations. In the far-field, the distribution vorticity is reduced to concentrated vortex lines where the simpler Biot-Savart's law is employed for the velocity-field calculations. The method is applied to steady and unsteady flow problems without any restrictions on the order of

magnitude of the disturbances in the flow field. The presented numerical results show that the method produces accurate results and it is computationally efficient.

References

[1]Belotserkovskii, S. M., "Calculation of the Flow Around Wings of Arbitrary Planforms Over a Wide Range of Angles of Attack," NASA TT F-12, 391, 1969.

[2]Rehbach, C., "Calculation of Flow Around Zero-Thickness Wings with Evolute Vortex Sheets," NASA TT F-15, 183, 1973.

[3]Rehbach, C., "Numerical Investigation of Vortex Sheets Issuing from Separation Line Near the Leading Edge," NASA TT F-15, 530, 1974.

[4]Kandil, O. A., Mook, D. T., and Nayfeh, A. H., "Nonlinear Prediction of the Aerodynamic Loads on Lifting Surfaces," Journal of Aircraft, Vol. 13, No. 1, January 1976, pp. 27-28.

[5]Kandil, O. A., "Numerical Prediction of Vortex Cores from the Leading and Trailing Edges of Delta Wings," ICAS paper No. 14.2, The 12th Congress of the International Council of the Aeronautical Sciences, Munich, Germany, October 1980.

[6]Kandil, O. A., and Balakrishnan L., "Recent Improvements in the Prediction of the Leading and Trailing Edge Vortex Cores of the Delta Wings," AIAA Paper 81-1263, 1981.

[7]Johnson, R. T. and Rubbert, P. E., "Advanced Panel-Type Influence Coefficient Methods Applied to Subsonic Flows," AIAA paper 75-50, 1975.

[8]Weber, J. A., Brune, G. W., Johnson, F. T., Lu, P. and Rubbert, P. E., "Three Dimensional Solution of Flows Over Wings with Leading Edge Vortex Separation," AIAA Journal, Vol. 14, 1976, pp. 519-525.

[9]Johnson, F. T., Lu, P., Brune, G. W., Weber, J. A. and Rubbert, P. E., "An Improved Method for the Prediction of Completely Three-Dimensional Aerodynamic Load Distributions on Configurations with Leading-Edge Separation," AIAA paper 76-417, 1976.

[10]Kandil, O. A., Chu, L. and Yates, Jr., E. C., "Hybrid Vortex-Method for Lifting Surfaces with Free Vortex Flow," AIAA paper 80-0070, 1980.

[11]Chu, L., "Nonlinear Hybrid-Vortex Method for Wings Having Side-Edge Separations," M.S. thesis Old Dominion University, Norfolk, VA, December 1980.

[12]Atta, E. H., Kandil O. A., Mook, D. T. and Nayfeh, A. H., "Unsteady Aerodynamic Loads on Arbitrary Wings Including Wing-Tip and Leading-Edge Separations, AIAA Paper 77-156, 1977.

[13]Kandil, O. A., Atta, E. H., and Nayfeh, A. H., "Three Dimensional Steady and Unsteady Asymmetric Flow Past Wings of Arbitrary Planforms," AGARD CP No. 227, Unsteady Aerodynamics, 1978, pp. 2.1-2.19.

[14]Belotserkovskii, S. M. and Nisht, M. I., "Nonstationary Nonlinear Theory of a Thin Wing of Arbitrary Planform," Mechanika Zhidkosti Gasa, No. 4, 1974, pp. 100-108.

[15]Lavin, D. and Katz, J., "Vortex-Lattice Method for the Calculation of the Nonsteady Separated Flow over Delta Wings," Journal of Aircraft, Vol. 18, No. 12, December 1931, pp. 1032-1037.

[16]Summa, J. M., "Potential Flow About Three-Dimensional Lifting Cofigurations with Application to Wings and Rotors," AIAA Paper 75-126, 1975.

[17]Summa, J. M., "A Numerical Method for the Exact Calculation of Airloads Associated with Impulsively Started Wings," AIAA Paper 77-002, 1977.

[18]Scholz, Von N., "Kraft und Druckverteilungsmessungen an Tragflächen Kleiner Streckung," Forscharb. Ing. Wes., No. 16, 1949, pp. 85-92.

[19]Morino, L. and Tseng, K., "Time-Domain Green's Function Method for Three-Dimensional Nonlinear Subsonic Flows," AIAA paper No. 78-1204, 1978.

[20]Lessing, H. C., Troutman, J. C., and Menees, G. P., "Experimental Determination of the Pressure Distribution on a Rectangular Wing Oscillating in the First Bending Mode for Mach numbers from 0.24 to 1.30," NASA TN D-344, 1960.

APPENDIX A
SEMI-ANALYTICALLY INTEGRATED EXPRESSIONS OF THE INDUCED VELOCITY FIELD

$$\bar{V} = u_\xi \bar{e}_\xi + v_n \bar{e}_n + w_\zeta \bar{e}_\zeta \tag{A.1}$$

$$= \sum_{j=1}^{5} (\tilde{u}_j \bar{e}_\xi + \tilde{v}_j \bar{e}_n + \tilde{w}_j \bar{e}_\zeta)\, a_j \tag{A.2}$$

$$= \frac{1}{4\pi} \sum_{j=1}^{5} \sum_{i=1}^{2,3} \int_{\zeta_i}^{\zeta_{i+1}} (u_j \bar{e}_\xi + v_j \bar{e}_n + w_j \bar{e}_\zeta)\, d\zeta\, a_j \tag{A.3}$$

where

$$u_1 = \hat{y}(F/G_3 - \hat{x}/G_2)/G_1 \tag{A.4}$$

$$u_2 = \zeta u_1 \tag{A.5}$$

$$u_3 = \hat{y}[(\hat{x}F + G_1)/G_3 - G_2]/G_1 \tag{A.6}$$

$$u_4 = 0 \tag{A.7}$$

$$u_5 = 0 \tag{A.8}$$

$$v_1 = 1/G_3 - 1/G_2 \tag{A.9}$$

$$v_2 = \zeta v_1 - (\hat{z} - \zeta)u_3 \tag{A.10}$$

$$v_3 = \ln[(G_2 - \hat{x})/(G_3 - F)] + (\hat{x} - F)/G_3 \tag{A.11}$$

$$v_4 = -(\hat{z} - \zeta)u_1 \tag{A.12}$$

$$v_5 = \zeta v_4 \tag{A.13}$$

$$w_1 = 0 \tag{A.14}$$

$$w_2 = u_3 \tag{A.15}$$

$$w_3 = 0 \tag{A.16}$$

$$w_4 = u_1 \tag{A.17}$$

$$w_5 = u_2 \tag{A.18}$$

$$F = \hat{x} - s_i\zeta - b_i \tag{A.19}$$

$$G_1 = \hat{y}^2 + (\hat{z} - \zeta)^2 \tag{A.20}$$

$$G_2 = (\hat{x}^2 + G_1)^{1/2} \tag{A.21}$$

$$G_3 = (F^2 + G_1)^{1/2} \tag{A.22}$$

$$s_i = \frac{\xi_{i+1} - \xi_i}{\zeta_{i+1} - \zeta_i} \tag{A.23}$$

$$b_i = \xi_i - s_i\zeta_i \tag{A.24}$$

APPENDIX B
ANALYTICALLY INTEGRATED EXPRESSIONS OF THE INDUCED VELOCITY FIELD

$$\bar{V} = u_\xi \bar{e}_\xi + v_n \bar{e}_n + w_\zeta \bar{e}_\zeta \tag{B.1}$$

$$= \sum_{j=1}^{5} (\tilde{u}_j \bar{e}_\xi + \tilde{v}_j \bar{e}_n + \tilde{w}_j \bar{e}_\zeta)a_j \tag{B.2}$$

where

$$u_\xi = \frac{1}{4\pi}\Big[\Big(\frac{-\hat{y}}{|\hat{y}|}A_1\Big)a_1 + \Big(\frac{-\hat{z}\hat{y}}{|\hat{y}|}A_1 - \frac{\hat{y}}{M_1^{1/2}}A_2\Big)a_2 + \Big(\frac{-\hat{y}}{2}A_3 - \frac{\hat{x}\hat{y}}{|\hat{y}|}A_1 + \frac{\hat{y}t}{M_1^{1/2}}A_2\Big)a_3\Big]_{\zeta_{in},\xi_{in}}^{\zeta_{fn},\xi_{fn}} \tag{B.3}$$

$$v_n = \frac{1}{4\pi}\Big\{\Big(1/2\,A_3 - \frac{t}{M_1^{1/2}}A_2\Big)a_1 + \Big[\frac{\hat{z}}{2}A_3 + \frac{2r}{M_1} - \frac{t(\hat{x}t+I-\hat{z}) + t(I-\hat{z}t^2)-\hat{x}}{M_1^{3/2}}A_2\Big]a_2 + \Big[\frac{\hat{x}}{2}A_3 - |\hat{y}|\,A_1 - \frac{tr}{M_1} - \frac{\hat{x}t\,M_1 + (I-\hat{z}+\hat{x}t)}{M_1^{3/2}}A_2\Big]a_3 + \Big(\frac{1}{M_1^{1/2}}A_2\Big)a_4 + \Big[\Big(\frac{\hat{x}}{2}A_3 - |\hat{y}|\,A_1 + \xi + \frac{\hat{x}}{2}\ln[(\hat{x}-\xi)^2 + \hat{y}^2] - \hat{y}\tan^{-1}\frac{\xi-\hat{x}}{\hat{y}} + \frac{tr}{M_1} + \frac{t^2(2\hat{z}-I-\hat{x}t)}{M_1^{3/2}}A_2 - \xi\ln[2(t\xi+I-\hat{z}) + 2r]\Big]a_5\Big\}_{\zeta_{in},\xi_{in}}^{\zeta_{fn},\xi_{fn}} \tag{B.4}$$

$$w_\zeta = -\frac{1}{4\pi}\Big[\Big(\frac{-\hat{y}}{2}A_3 - \frac{\hat{x}\,\hat{y}}{|\hat{y}|}A_1 + \frac{\hat{y}\,t}{M_1^{1/2}}A_2\Big)a_2 + \Big(\frac{-\hat{y}}{|\hat{y}|}A_1\Big)a_4 + \Big(\frac{-\hat{z}\hat{y}}{|\hat{y}|}A_1 - \frac{\hat{y}}{M_1^{1/2}}A_2\Big)a_5\Big]_{\zeta_{in},\xi_{in}}^{\zeta_{fn},\xi_{fn}} \tag{B.5}$$

$$r = [(\hat{x}-\xi)^2 + \hat{y}^2 + (\hat{z}-\zeta)^2]^{1/2} \tag{B.6}$$

$$M_1 = 1 + t^2 \tag{B.7}$$

$$A_1 = \tan^{-1}\frac{(\hat{z}-I-\hat{x}t)(\xi-\hat{x}) + \hat{y}^2 t}{\hat{y}r} \tag{B.8}$$

$$A_2 = \ln[2\,M_1^{1/2}r + 2M_1\xi + 2t(I-\hat{z}) - 2\hat{x}] \tag{B.9}$$

$$A_3 = \ln \frac{\bar{z}-\bar{I}-t\xi-r}{\bar{z}-\bar{I}-t\xi+r} \qquad (B.10)$$

$$\varsigma_{fn} = t_{fn}\xi + I_{fn} \quad , \quad \varsigma_{in} = t_{in}\xi + I_{in} \qquad (B.11)$$

$$\xi_{fn} = \varsigma_2 \quad , \quad \varsigma_{in} = \varsigma_1 \qquad (B.12)$$

$$t_{in} = \frac{\varsigma_2 - \varsigma_1}{\xi_2 - \xi_1} \quad , \quad I_{in} = \frac{\varsigma_1 \xi_2 - \varsigma_2 \xi_1}{\xi_2 - \xi_1} \qquad (B.13)$$

For a triangular panel:

$$t_{fn} = \frac{\varsigma_3 - \varsigma_2}{\xi_3 - \xi_2} \quad , \quad I_{fn} = \frac{\varsigma_2 \xi_3 - \varsigma_3 \xi_2}{\xi_3 - \xi_2} \qquad (B.14)$$

For a trapezoidal panel:

$$t_{fn} = \frac{\varsigma_4 - \varsigma_3}{\xi_4 - \xi_3} \quad , \quad I_{fn} = \frac{\varsigma_3 \xi_4 - \varsigma_4 \xi_3}{\xi_4 - \xi_3} \qquad (B.15)$$

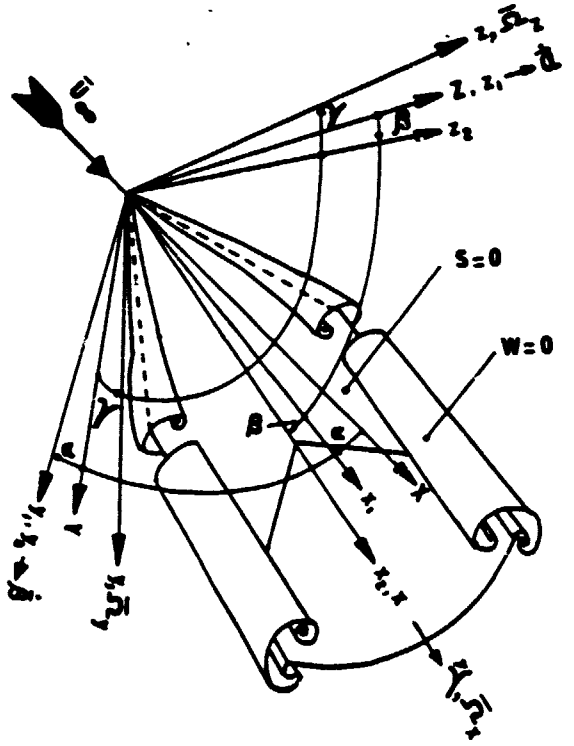

Figure 1. Space-Fixed Coordinates XYZ, Wing-Fixed Coordiantes xyz, and Eulerian's Anyles αβγ.

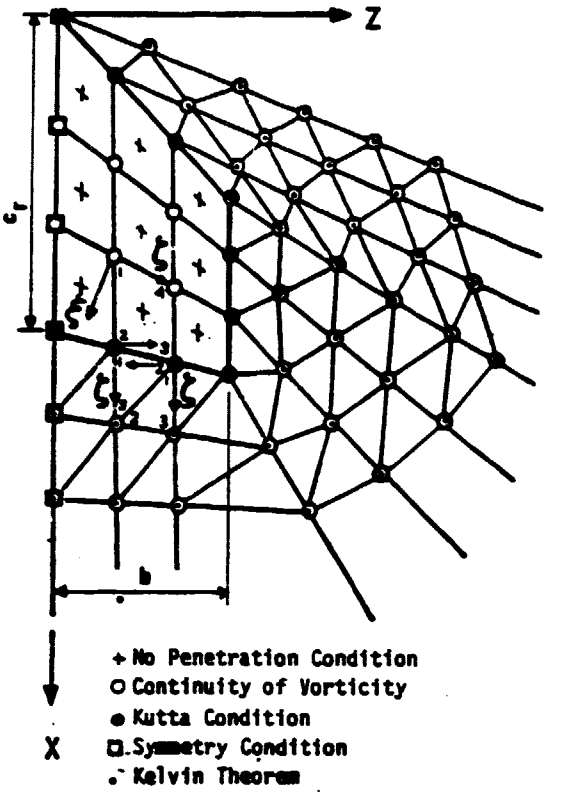

Figure 2. Boundary Conditions and Arrangement of Bound- and Free-Vortex Panels

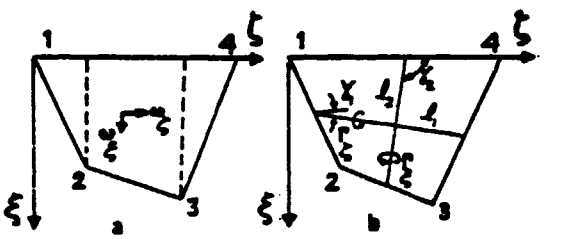

a. Quadrilateral Panel With Distributed Vorticity for the Near-Field Calculations

b. Equivalent Concentrated Vortex Lines for the Far-Field Calculations

Figure 3. Quadrilateral Vortex Panel Used on the Bound-Vortex Sheet

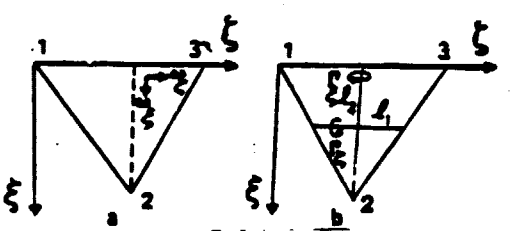

a. Triangular Panel With Distributed Vorticity for the Near-Field Calculations

b. Equivalent Concentrated Vortex Lines for the Far-Field Calculations

Figure 4. Triangular Vortex Panel Used on the Free-Vortex Sheet

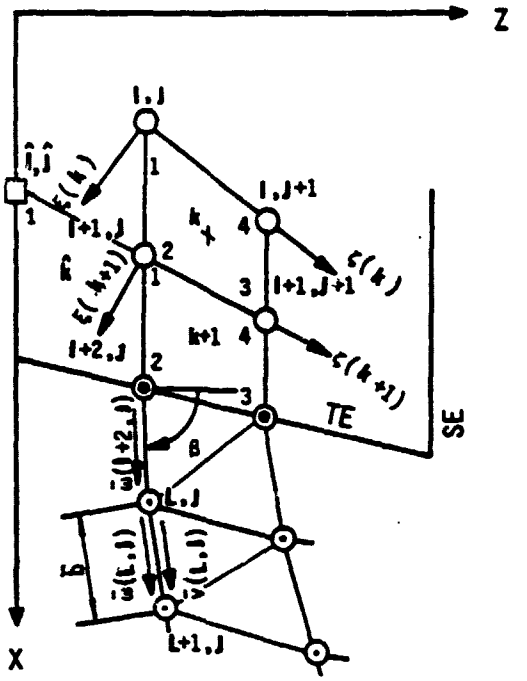

+ No-Penetration Condition, Eq. (29)
O Continuity of Vorticity Condition, Eq. (30)
● Kutta Condition, Eq. (33)
□ Symmetry Condition, Eq. (34)
• Kinematic and Dynamic Conditions, Eq. (35)

Figure 5. Details of the Boundary Conditions for the Steady-Flow Problem.

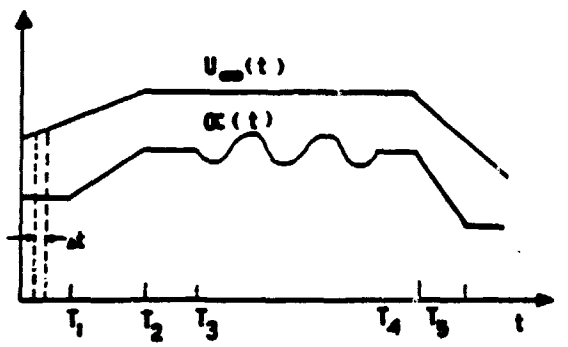

Figure 6. Typical Sources of Unsteadiness for the Unsteady Symmetric Flow Problem

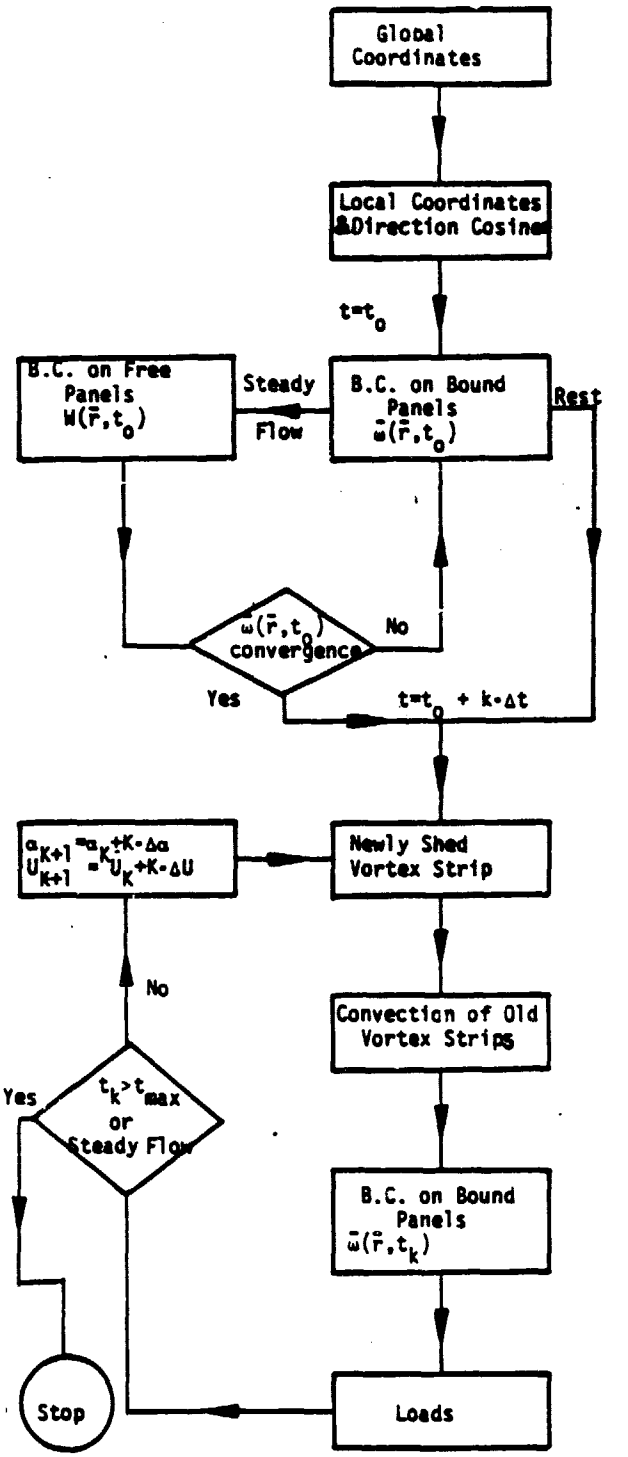

Figure 7. Flow Chart of the Computer Program For the Steady and Unsteady (Time Domain Approach) Flow Problems.

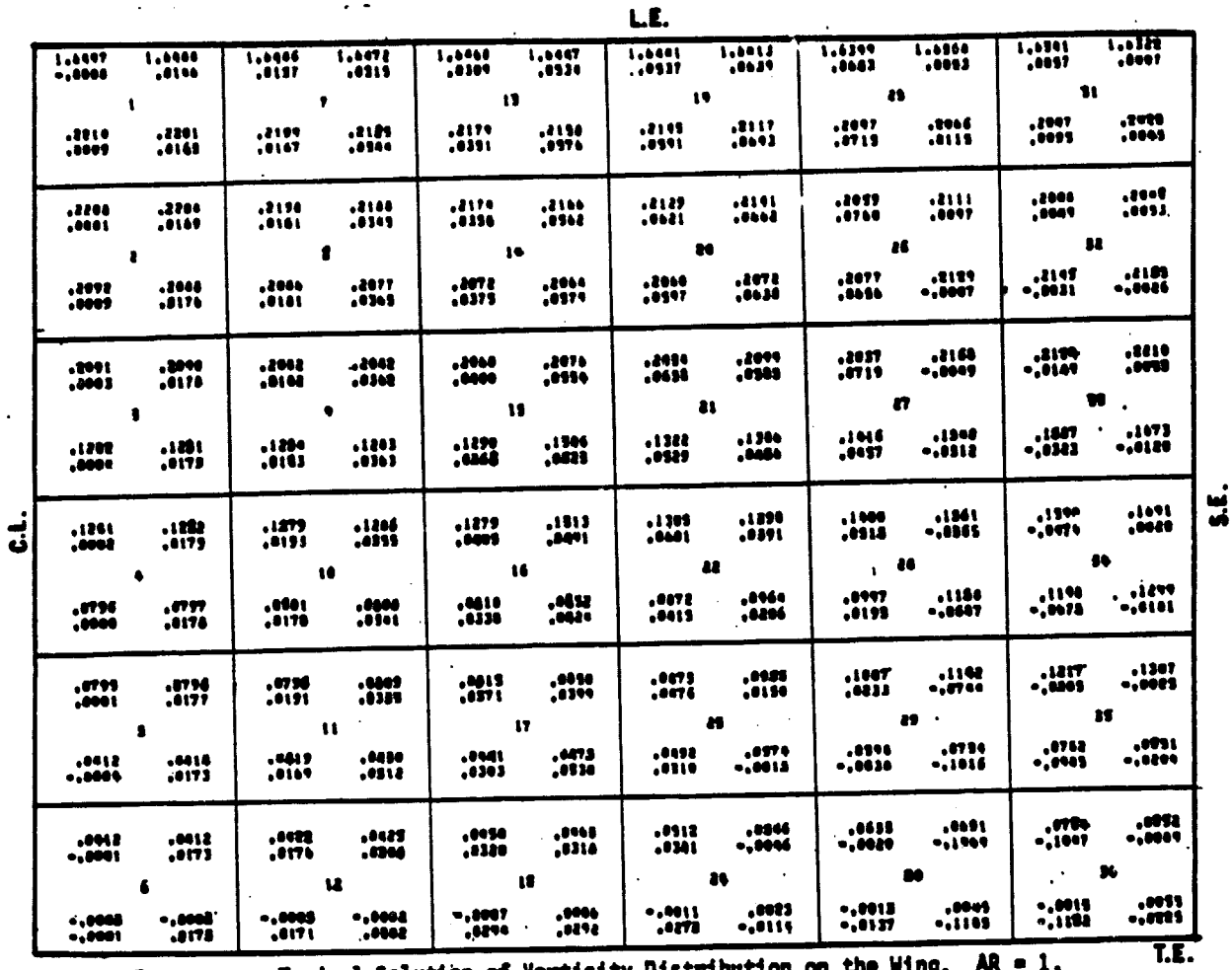

Figure 8. Typical Solution of Vorticity Distribution on the Wing, AR = 1, α = 9.7°, 6 x 6 panels.

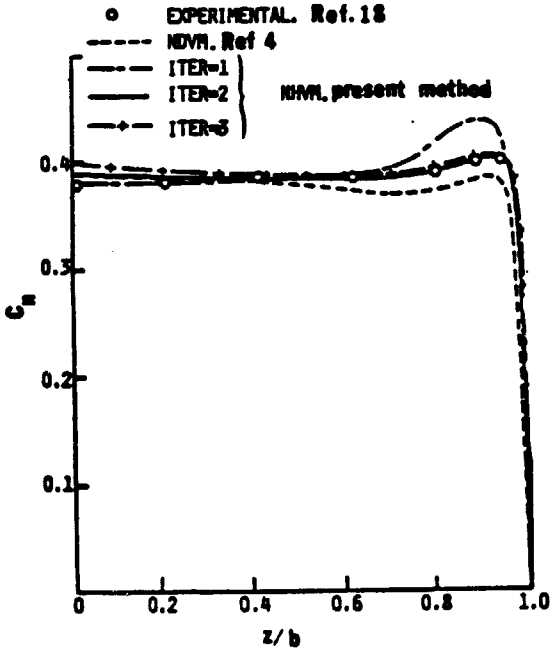

Figure 9. Spanwise variation of the section normal-force coefficient for a rectangular wing at 3 iteration steps, AR = 1, α = 9.7°, 6 x 6 panels.

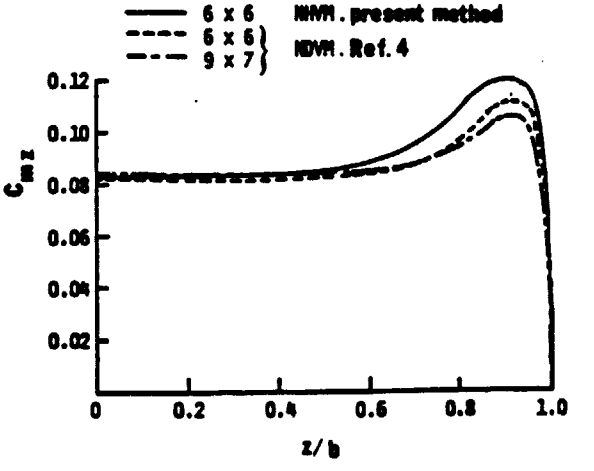

Figure 10. Spanwise variation of the pitching moment coefficient for a rectangular wing. AR = 1, α = 9.7°, 6 x 6 panels.

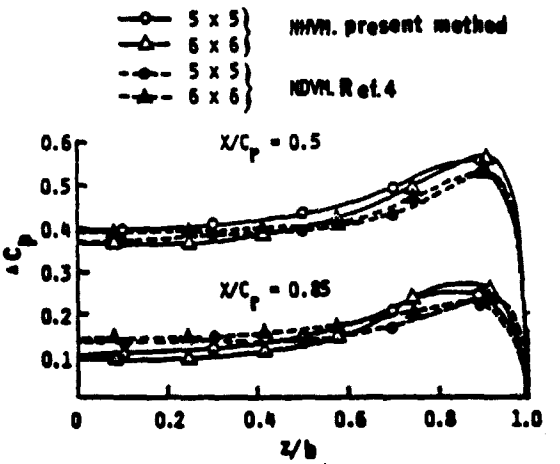

Figure 11. Spanwise variation of net pressure at different chordwise stations for a rectangular wing, AR = 1, α = 15°, 5 x 5 and 6 x 6 panels

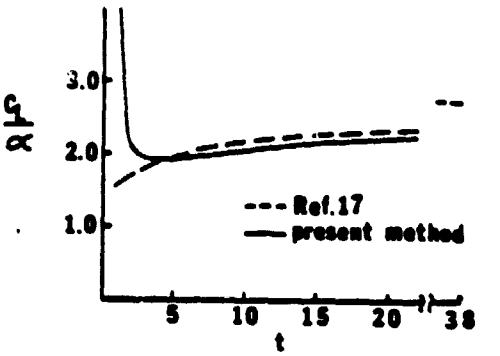

Figure 13. Growth of Indicial Lift for a Rectangular Wing, AR=3, α=5°, 5x5 Bound Panels, zero Thickness, No Tip Separation.

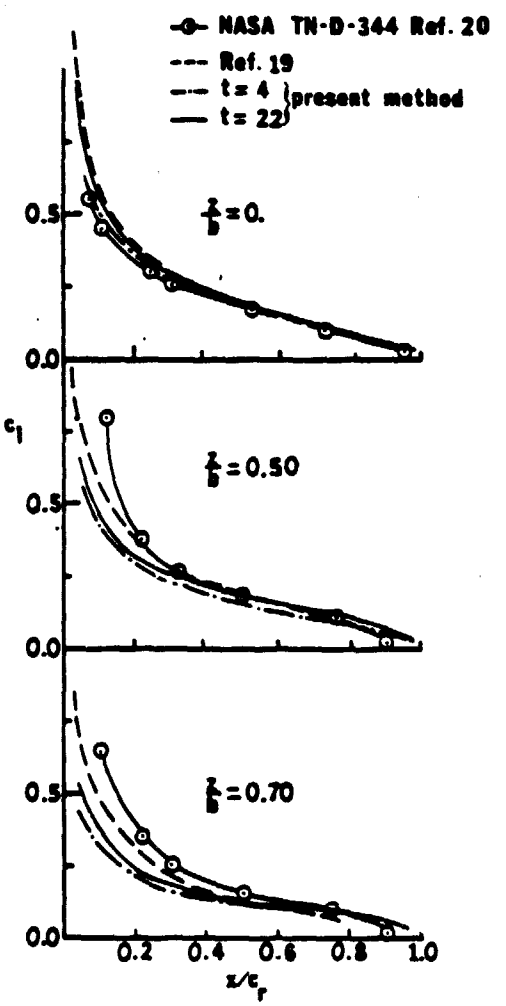

Figure 12. Chordwise Variation of the Lift Coefficient at Various Spanwise Stations for a Rectangular Wing, AR=3, α=5° 5x5 Bound Panels, zero thickness, No Tip Separation.

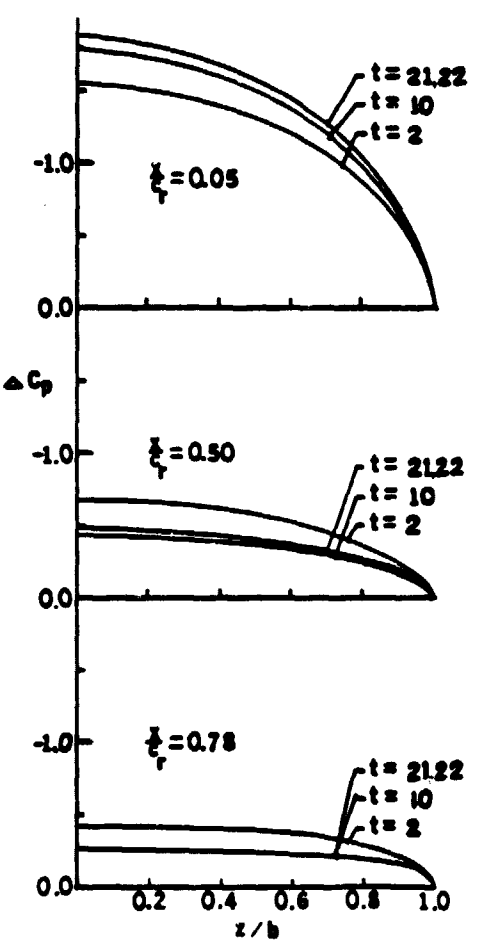

Figure 14. Spanwise Variation of net pressure coefficient at different chordwise station for a Rectangular Wing, AR=2, α=20.5°, 5x5 Bound Panels, zero-Thickness, No Tip Separation.

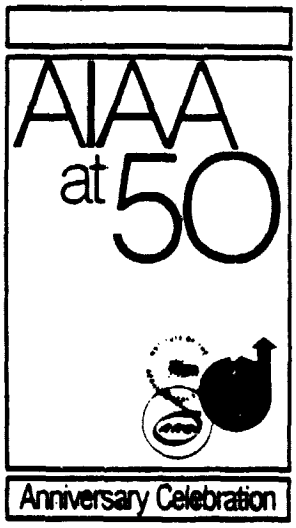

AIAA-81-1263
Recent Improvements in the Prediction of the Leading and Trailing Edge Vortex Cores of Delta Wings

O. A. Kandil, Old Dominion University, Norfolk, VA

AIAA 14th Fluid and Plasma Dynamics Conference

June 23-25, 1981/Palo Alto, California

RECENT IMPROVEMENTS IN THE PREDICTION OF THE LEADING AND TRAILING EDGE VORTEX CORES OF DELTA WINGS

Osama A. Kandil* and Lakshmanan Balakrishnan**
Department of Mechanical Engineering and Mechanics
Old Dominion University, Norfolk, VA

Abstract

The recently Modified Nonlinear Discrete-Vortex (MNDV) method has shown a remarkable success in predicting, for the first time, the latest experimental data published by Hummel on vortex formation behind a slender delta wing at an angle of 20.5°.

This paper presents the recent developments in the MNDV-method in order to accurately predict the location of the trailing-edge vortex core and the surface pressure distribution.

Moreover, a Viscous Core model, based on the boundary-layer-like approximations (quasi-cylindrical approximations), is presented. The resulting parabolic equations, with the outer-edge boundary conditions obtained from the inviscid-model solution using the MNDV-method, are integrated using a finite-difference marching technique. Typical velocity profiles of the leading and trailing vortex cores have been used to initiate the step-by-step marching technique.

I. Background

I.1 Existing Experimental Data and Concluding Remarks

The separated free-shear layers emanating from the leading edges of highly sweptback wings roll up spirally into two counter rotating vortex cores. The vortex cores are fed, through the free-shear layers, with vorticity shed along the wing leading edges from the boundary-layer flow on the wing surfaces. This flow separation is known as the "primary separation" and it has a dominant effect on the wing aerodynamic characteristics due to the large strength of its vortex cores and their proximity to the upper surface under the primary vortex core.

The adverse spanwise pressure gradient due to the primary vortex core induces "secondary separation" of the boundary-layer flow on the upper surface. Depending on the angle of attack and the wing aspect ratio, the secondary separated flow forms either an additional free-shear layer or a bubble. In the range of moderate to large angles of attack, a secondary free-shear layer develops, rolls up spirally in an opposite sense to that of the primary free-shear, and forms a secondary-vortex core of much smaller strength than that of the primary-vortex core[1-4].

Depending on the type of boundary-layer flow on the upper surface, the secondary-vortex core may affect the pressure distribution on this surface. For a laminar boundary-layer flow, a small pressure peak is produced between the secondary and primary lines of separation while for a turbulent boundary-layer flow, such a peak is hardly noticed and the pressure peak corresponding to the primary-vortex core is larger than that of the laminar boundary-layer flow[5]. A third type of flow involving a "tertiary" separation may occur between the lines of primary and secondary separations due to the adverse spanwise pressure gradient generated by the secondary-vortex core[1,5].

It is seen from the description given above that secondary and tertiary separations are viscous phenomena and cannot be modeled by using inviscid analysis only. However, their effects are small particularly when turbulent boundary-layer flow exists on the upper surface of the wing and hence they are neglected. Therefore, when inviscid analysis is used to predict pressure distributions, one must compare the surface pressure distributions with those experimental data corresponding to turbulent boundary-layer flows[6].

The free-shear layer emanating from the trailing edge is of opposite strength to that of the primary free-shear layer. Within a short distance behind the trailing edge (a distance of a 1/4 root-chord length for a delta wing of aspect ratio of one at 20.5° angle of attack[5]), the trailing free-shear layer rolls up spirally in an opposite sense to that of the primary free-shear layer and forms two counter rotating vortex cores. The trailing-edge vortex core has the same sense of rotation and almost the same spanwise location as those of the secondary vortex core, although each originates from a different phenomenon. The former is due to an edge separation while the latter is due to a surface separation. Hummel[5] concluded from his latest experimental measurements for turbulent boundary layers at the trailing edge that the secondary-vortex core decays rapidly behind the trailing edge and its remains roll up into the trailing vortex.

Figure 1 (reproduced from Reference 5) shows the vortex formation behind a slender delta wing. Figure 1b corrects the location of the trailing-edge core as given earlier[7-9] by Figure 1a. It also shows that the secondary-vortex core has the same spanwise location as that of the trailing-edge vortex core but it does not show their interaction which is still unknown.

Predicting the correct formation of the trailing-edge vortex core is essential for predicting the correct aerodynamic loads near the wing trailing edge due to its proximity to this edge. Moreover, a correct prediction is of paramount importance to problems involving high-angle-of-attack aerodynamics for the canard-wing configurations. Consequently, one concludes that any prediction method which employs a prescribed shape of the trailing-edge vortex sheet (the so-called "fixed design wake"[10, 11]) will be strictly limited to isolated-wing problems away from the trailing-edge region.

The size of the primary-vortex core and

*Associate Professor, Member AIAA
**Graduate Student, Member AIAA

viscosity of the flow within a narrow region around the core centerline play important roles in the aerodynamic characteristics of low-aspect ratio wings at large angles of attack. For these types of wings, it is well known that the lift coefficient increases nonlinearly with the increase in the angle of attack. This is attributed to the increase of the strength of the primary vortex core. However, the increase in the lift coefficient is limited by the occurrence of vortex-core breakdown over the wing and hence there exists a maximum angle of attack corresponding to the maximum lift.

The phenomenon of vortex-core breakdown is defined as an abrupt increase in the core diameter. It occurs due to the adverse swirl-induced pressure gradients along the core axis[12, 13]. Using the radial component of the momentum equation of the boundary-layer like equations (for quasi-cylindrical vortex cores), one can show that an increase in the swirl velocity of the flow, due to an increase in the core strength, increases the axial pressure gradient along the core axis. Therefore, the flow near the core axis loses its axial momentum and swelling of the vortex core develops.

For moderate angles of attack, vortex-core breakdown develops far downstream from the wing trailing edge. As the angle of attack increases, vortex-core strength increases and the breakdown point travels upstream toward the trailing edge. As the breakdown point approaches the trailing edge, the slope of the lift versus angle of attack curve decreases until the maximum lift is reached. Thereafter, the lift coefficient drops sharply, the breakdown point crosses the trailing edge and the wing stalls.

To account for all these changes, one has to include the viscosity within the vortex core in order to have a realistic model in this region.

I.2.Existing Inviscid Models and Concluding Remarks

In most of the existing inviscid analyses, primary flow separation is only considered. The attached boundary layers are replaced with bound-vortex sheets while the free-shear layers are replaced with free-vortex sheets. Accordingly, the inviscid region representing the vortex core should be represented by a conical spiral vortex sheet which ends with a concentrated vortex line along the core centerline. Although this theoretical representation of the vortex-core is ideal for the inviscid model, the usage of many turns within the core region creates numerical problems in a three-dimensional model which does not assume slender-body approximations. The numerical problems arise due to the proximity of the vortex layers of the spiral and due to the large number of small-size panels needed to accurately model the turns. However, it was found, according to the numerical results and their excellent comparison with the experimental data, that only one turn of the spiral need to be accurately modeled while the remaining turns of the spiral are replaced by a cut ending with a concentrated vortex line along its edge.

In all the inviscid models, the wing edges, where separation occurs, are assumed to be sharp so that the separation lines are known a priori and hence viscous modeling is not needed to determine the lines of separations. However, for wings with round edges, viscous modeling is needed to determine these lines[14]. Moreover, vortex-breakdown points are assumed to be far downstream so that the variations in the size of the primary-vortex core can be neglected. In fact, this assumption limits the large angles of attack at which inviscid modeling is applicable. With the vorticity confined to the inner boundary of the flow region (bound- and free-vortex sheets), the resulting model is a potential-flow model governed by Laplace's equation and certain boundary conditions[15].

The existing inviscid models can be divided into four main groups. Next, each group is presented and evaluated.

The first group of models uses slender body and conical flow assumptions[16, 23]. Modeling of the primary-vortex core and its feeding sheet was first introduced by Brown and Michael[17]. However, the feeding sheet in their model was taken as a planar surface and hence it did not represent the real rolled-up vortex sheet. Mangler and Smith[18] introduced the first realistic model of the primary-vortex core and its feeding sheet. However, this model does not account for the feeding-sheet deformation in the chordwise direction due to the slender-body assumption. These models satisfactorily predict the pressure distribution on the front portion of the wing surface. In the rear portion, the models fail to predict satisfactory pressure distributions because Kutta condition cannot be satisfied at the trailing edge. Such models were limited to slender delta planforms.

The second group of models uses the old NDV-method[24-36]. The most obvious drawback of the old model is the lack of a realistic model of the primary-vortex core and its feeding sheet. The primary-vortex sheet was modeled by a system of segmented vortex lines which were rendered force-free during the course of solution and no attempt was made to lump these lines into a concentrated primary-vortex core. Although the agreement between the calculated and experimental total aerodynamic loads was excellent, the agreement between the calculated and experimental pressure coefficients was less than satisfactory in particular for highly sweptback wings.

The third group of models employs doublet-panels[10, 11, 37-39]. In this method, the wing and its free-vortex sheets are divided into networks of quadrilateral panels. Each panel of the networks representing the wing has a biquadratic local doublet distribution and a bilinear local source distribution. The panels of networks representing the free-vortex sheets have biquadratic local doublet distributions. Source and doublet splines are used to express the distributions of singularities on the networks in terms of discrete values of singularity strength at certain standard points on each network. The boundary conditions and continuity of singularity strengths across abutting networks are enforced at certain standard points on each network. The results of this method[40, 41] are generally good when the solution converges. Apparently, the difficulty in obtaining convergence is due to the failure in satisfying the continuity of the derivatives of the doublet strength across abutting networks. This is equivalent to the existence of concentrated vortex lines between abutting

networks.

The doublet panel method was extended[42] to include the effect of entrainment of the primary vortex cores through an emptrical approach. The results indicated that the entrainment increased the normal-force coefficient substantially over the experimental values.

This group of models do not account for the chordwise deformation of the primary-vortex sheet. Consequently, the primary vortex sheet cannot be fed three-dimensionally with the shed vorticity. Moreover, the trailing-edge free-vortex sheet was represented by a "fixed design wake."

Therefore, none of the models given in the first and third groups is capable of predicting the deformation and interaction of the trailing-edge vortex sheet and its vortex core. Additional references of the three groups given above can be found in references 43 and 44.

The fourth group of models employs a nonlinear hybrid vortex method[15, 45]. In this method, continuous-vorticity and vortex-line representations of the wing and its separated free-shear layers are used. Continuous vorticity is used in the near-field calculations while discrete vortex-lines are used in the far-field calculations.

The wing and its free-shear layers are divided into planar quadrilateral panels having first-order vorticity distribution. The aerodynamic boundary conditions and continuity of the vorticity distributions are imposed at certain nodal points on the panels. To satisfy these conditions, an iterative technique is followed which alternatively yields the local vorticity distribution on the bound-vortex panels and the shape of the free-vortex panels. This method has been used to calculate the steady distributed and total loads on planar-low-aspect-ratio rectangular wings. The results have shown that the spanwise variations of the load coefficients are in good agreement with the experimental data. Comparisons of the results with those of the NDV-method have shown that the hybrid method requires less number of vortex panels for the same accuracy. Currently the method is extended to include leading and side-edge separations for steady-flow problems and for unsteady-flow problems due to small oscillations of wings around large mean angles of attack (flutter applications) and due to general nonstationary wing motions (dynamical applications). Work is underway to use this technique to predict the details of the flow field including the primary and trailing-edge vortex core interactions.

Although the old NDV-method, used in the second group of models, was almost abandoned in predicting the flow details and the distributed aerodynamic characteristics, the modified NDV-method pinpointed and cured most of the problems encountered with the old method[40]. It enjoyed a remarkable success in predicting, for the first time, the latest experimental results of Hummel[5].

I.3. Existing Viscous-Core Models and Concluding Remarks

In this paper, we only consider existing viscous-core models which adopt the quasi-cylindrical approximations. In the quasi-cylindrical approximations, we assume that the axial gradients are small compared with the radial gradients and that the streamsufaces be cylindrical. These boundary-layer-like assumptions simplify Navier-Stokes equations and reduce them to a parabolic set of equations. Approximations of this type have been used by Gartshore[47], Hall[48,49], Bossel[13], Raat[50] and Wilson[51] to predict the locations of the vortex-core breakdown. Gartshore and Hall used the differential form of the equations while Bossel, Raat and Wilson used the integral form of the equations.

The numerical results obtained from the quasi-cylindrical equations have shown good agreement with the experimental data particularly for the vortex core behavior. For the locations of the breakdown points, the difference between the predicted and measured locations was within two diameters of the viscous core.

In this paper, we use the quasi-cylindrical approximations for the narrow viscous region around the core centerline. Outside the viscous region, one can treat the flow as a potential flow only or as a rotational inviscid flow followed by an outer potential flow. Hence two models with various degrees of accuracy emerge. In the first model, the vortex core is represented by a narrow axisymmetric viscous region around the core axis. This viscous core is fed with vorticity shed from the wing edges through a vortex sheet with only one turn and a cut. The flow outside the viscous core and the vortex sheet is a potential flow. Figure 2.a. shows a schematic of this model. In the second model, the vortex core region is divided into an inner narrow viscous part and an outer inviscid and rotational part. In each part the flow is axisymmetric. Outside the core region, a potential flow is assumed. Figure 2.b. shows a schematic of this model. In this paper, only the first model is considered.

II. Steady Inviscid Model and Prediction of the Inviscid Cores

II.1. Nomenclature

AR	wing aspect ratio
b	wing half span
b(x)	local half span
c_p	static pressure
Δc_p	net surface pressure
c_r	wing root chord
ITER	iteration Number
LE	Leading Edge
LEC	Leading Edge core
TE	Trailing Edge
TEC	Trailing Edge core
xyz	wing-fixed coordinates, origin at wing vertex, x-axis is along the root chord, y-axis is perpendicular to wing
$\bar{x}\bar{y}\bar{z}$	wind-fixed coordinates, origin at the trailing edge, $\bar{x}$-axis is parallel to the freestream direction
$\bar{Q}_\infty$	freestream velocity
$\bar{V}$	velocity at any field point
$V_{\bar{x}}, V_{\bar{y}}, V_{\bar{z}}$	components of $\bar{V}$ in the wind coordinate system
$V_{\bar{z}\bar{y}}$	component of $\bar{V}$ in planes $\bar{x}$ = constant,

$V_{\bar{z}\bar{y}}=(V_{\bar{z}}^2 + V_{\bar{y}}^2)^{\frac{1}{2}}$

α angle of attack

ξ,η,ζ dimensionless coordinates, $\xi=\bar{x}/b$, $\eta=\bar{y}/b$, $\zeta=\bar{z}/b$

II.2. Existing NDV-Method and Its Drawbacks

In this section, a critical evaluation of the existing NDV-Method is given in order to pinpoint its drawbacks. In this method, the bound-vortex sheet is replaced by a bound-vortex lattice and the free-vortex sheets are replaced by segmented free-vortex lines.

Starting with an initial guess for the inclination of the free-vortex lines, the no-penetration condition is satisfied at certain control points on the bound-vortex lattice. The resulting set of linear algebraic equations is solved for the circulation distribution. Next, with the known circulation distribution, the positions of the vortex segments of the free-vortex lines are calculated by simultaneously enforcing the no-penetration and no-pressure jump conditions at certain control points on these segments. These two steps of calculations represent one iterative cycle. Several iterative cycles are performed until the positions of the free-vortex segments or the circulation distributions converge.

Figure 3 shows a typical converged solution of the system of free-vortex lines in three views for a delta wing of aspect ratio of unity and 15^0 angle of attack. The plan view also shows the arrangement of bound-vortex lattice. In the three dimensional view the leading-edge core (LEC) is shown. This core is calculated after the solution converges and it represents the centroid of the leading-edge vortex system.

Comparison of height and spanwise position of the calculated centroid with those of the measured leading-edge core[1,4] is given in figure 4. Although this comparison was encouraging, the calculated centroid does not model the physical vortex core where the vortex core is continuously fed with vorticity from the leading edge through the free-shear layers. Using the system of free-vortex lines, the total-aerodynamic loads were accurately calculated but the calculated surface pressure distribution was unsatisfactory. On the other hand, using the centroid of the leading-edge vortex system instead of the leading-edge vortex system itself, the calculated surface pressure improved[36] (this does not satisfy the no-penetration condition on the wing since the centroid is calculated after the solution converges.) It should also be noted here that replacing the leading-edge vortex system by its centroid is similar to the model used by Legendre[16].

Figure 5 shows a recent converged solution of the system of free-vortex lines with a long deformed wake. It can be seen that the trace of the trailing-edge vortex system in cross planes indicates that the sheet tends to deform upwards showing a tendency to form a trailing-edge vortex core. However, the cross-flow planes taken further downstream show that the free-vortex lines leap-frog. This does not represent the real flow. Figure 6 shows four of this cross-flow planes taken perpendicular to the wind direction.

It is clearly seen from the few examples given above, that the existing model of the NDV-method does not realistically model the leading- and trailing-edge vortex cores. Therefore, the model and the numerical technique must be modified in order to obtain realistic vortex-core modeling.

II.3. The MNDV-Method and Modeling of the Primary-Vortex Core

In the MNDV-Method a realistic modeling of the primary-vortex core region is introduced. The old NDV-method is only used in the first iterative cycle to initiate the roll-up process and to calculate the centroid of the leading-edge vortex system. Next, the leading- and trailing-edge vortex segments are replaced by smaller segments. Then, the iterative cycles proceed.

In a typical iterative cycle, each free-vortex line of the leading-edge vortex system is allowed three-dimensionally to rotate around the most recently calculated centroid a prescribed portion of a turn (1/4, 1/2, 3/4, or 1 turn). This is done by continuously checking the coordinates of the free-vortex segments (as they are adjusted) with the location of the calculated centroid. Once this is achieved, the remaining free-vortex segments of each line are dumped into the calculated centroidal line of the vortex system. The iterative technique is followed until the circulation distribution converges.

Figure 7 shows typical solutions at different iterative cycles. It can be seen that after one iterative cycle, the system of free-vortex lines shows good roll-up. The converged solution, indicated by ITER=6, shows the leading-edge core and its feeding free-vortex lines. It can also be seen that the free-vortex lines continues to feed the LEC beyond the trailing edge. The trailing-edge core is also indicated on the figure. This will be clearly seen in the cross-flow planes discussed in the next section.

Figures 8 and 9 show converged solutions using a 12 x 12 bound-vortex lattice for 1/4 and 1/2 turns of the free-vortex lines.

II.4. Numerical Examples and Comparisons with Hummel's Experimental Results

The calculated circulations around the free-vortex lines emanating from the wing trailing edge was found to be of opposite sign to that of the free-vortex lines emanating from the wing leading edge. This is in agreement with Hummel's measurements. The difference in the signs can be explained as follows:

The primary-vortex core creates large suction pressure peak and hence the pressure continuously rises in the spanwise direction from the wing axis to the location of the suction peak (this is completely opposite to the spanwise variation of pressure for wings with large aspect ratio and small angles of attack.) Consequently, the circulation of the spanwise bound-vortex segments increases in the spanwise direction. In order to satisfy the spatial conservation of circulation at the nodes of the bound-vortex lattice, the spanwise increase of

circulation requires the circulation of the chordwise bound-vortex segments to be of opposite sign. In the present model, the leading-edge vortex system originates from spanwise-vortex segments at the leading edge while the trailing-edge vortex system originates from chordwise-vortex segments.

According to the difference in sign of the circulation of the trailing-edge vortex system from that of the leading-edge vortex system, one expects the trailing-edge vortex system to roll up in an opposite sense to the roll-up of the leading-edge vortex system.

In reference 46, the results of the MNOV-method using 1/4 and 1/2 turns only for the leading-edge vortex lines were presented. In this paper, we add to these cases the results of the 3/4 turn. The latest results clearly show the capability of the MNOV-method in reproducing and confirming the experimental results of Hummel[5].

Figures 10-12 show comparisons between the experimental and numerical results for leading- and trailing-edge vortex sheets and flow directions in cross-flow planes perpendicular to the wind direction. The numerical results are drawn at the same scale as that of the experimental results. The predicted sizes and locations of the leading- and trailing-edge vortex sheets are in excellent agreement with the measured ones. The results of the 3/4 turn show the the correct roll-up of the trailing-edge vortex sheet and the correct locations of the LEC and TEC. This is exactly what we expected when we increased the roll-up from 1/2 to 3/4 turn. With the 3/4 turn of the leading-edge vortex system, the roll-up tightens and larger velocities are induced at the trailing-edge vortex sheet which cause it to deform upwards and leftwards. Due to the large curvature of the trailing-edge vortex sheet (Figure 12, 3/4 turn case), one can see a small leapfrog at the TEC location. This is attributed to the insufficient number of vortex lines used to model this large curvature.

Figure 13 shows the results for an aspect ratio of 1.45. It is seen, by comparing these results with the corresponding results for the aspect ratio of one, that the TEC develops earlier than that of the aspect ratio of one.

Figure 14 shows comparions between the predicted and measured static-pressure contours in different cross-flow planes. The predicted sizes, locations, and levels of the pressure contours are in good agreement with those of the measured data.

Figure 15 shows comparisons of the predicted and measured spanwise net surface pressure variation at difference chordwise stations. It is seen that the results of the 3/4 turn are more accurate than that of the 1/2 turn. With 3/4 turn, the roll-up of the leading-edge vortex system tightens and produces better predicted distribution than that of the 1/2 turn.

The developed computer program of the MNOV-method is computationally efficient. On a CYBER-175 machine, a typical solution using a 12 x 12 lattice and including the cross-flow planes calculation takes 10 minutes of CPU time.

Currently the technique is modified for accurate near-field calculations by replacing the concentrated vortex segments with vortex panels having linear vorticity distributions. The vorticity functions are expressed in terms of the unknown circulations of the original concentrated vortex segments. This is the opposite process currently used in the Nonlinear Hybrid-Vortex Method[15,45].

III. Steady Viscous Model of the Vortex Core

III.1. Nomenclature

A_r	grid aspect ratio = $\Delta\xi/\Delta x$
a	fraction of the step size in the x-direction
b	= 1 - a
Δc_r	characteristic length
h	radial velocity in the computational domain = w / λ
k	swirl velocity in the computational domain = $\lambda\xi v$
m	axial station number
n	radial station number
p	pressure
R	= b/a
R_e	Reynold's number
r^e	stretched radial coordinate = $\tilde{r}R_e^{\frac{1}{2}}$
$\tilde{r}$	radial coordinate
$r_o(x)$	stretched outer core radius at any axial station
$r_o(x_1)$	stretched outer core radius at the initial axial station
$\tilde{U}_\infty$	freestream velocity
u	axial velocity
v	swirl velocity
w	stretched radial velocity = $\tilde{w}R_e^{\frac{1}{2}}$
$\tilde{w}$	radial velocity
x	axial coordinate
Δx	axial step size
λ	shape factor = $r_o(x)/r_o(x_1)$
ξ	radial coordinate in the computational domain
ξ_o	outer radius in the computational domain
$\Delta\xi$	radial step size

III.2. Formulation of the Problem

Starting with the nondimensional Navier-Stokes equations for incompressible axisymmetric steady flow, using a boundary-layer-like stretching transformation and performing an order of magnitude analysis, one obtains the nondimensional equations for quasi-cylindrical vortex flows[48].

$$\frac{\partial w}{\partial r} + \frac{w}{r} + \frac{\partial u}{\partial x} = 0 \tag{1}$$

$$\frac{v^2}{r} = \frac{\partial p}{\partial r} \tag{2}$$

$$w\frac{\partial u}{\partial r} + u\frac{\partial u}{\partial x} = -\frac{\partial p}{\partial x} + \frac{\partial^2 u}{\partial r^2} + \frac{1}{r}\frac{\partial u}{\partial r} \tag{3}$$

$$w\frac{\partial v}{\partial r} + \frac{wv}{r} + u\frac{\partial v}{\partial x} = \frac{\partial^2 v}{\partial r^2} + \frac{1}{r}\frac{\partial v}{\partial r} - \frac{v}{r^2} \tag{4}$$

This is a parabolic set of equations and hence a finite difference marching technique proceeding in the axial direction is applicable to this set. A basic difference between these equations and the first order boundary-layer equations is the pressure term. In the boundary-layer equations, the pressure across the boundary-layer thickness is constant while in the present equations the pressure is varying in the radial direction as given by equation (2).

The viscous region diverges in the downstream direction due to the swirl induced adverse pressure gradient. If the finite-difference grid is constructed in this physical domain, one needs to increase the number of grid points in the radial direction as one proceeds downstream. For computational efficiency and convenience of applying the finite-difference marching technique, it is desirable to transform the physical diverging domain into a rectangular computation domain. In this way, equal number of grid points can be used in the radial direction at each station of the axial direction (see figure 16). This is easily achieved by adopting the transformation used by Hall[48].

$$\xi = r(x)/\lambda(x) \tag{5}$$

$$\lambda(x) = r_o(x)/r_o(x_1) \tag{6}$$

Thus, the outer boundary ξ_o at any axial station becomes a constant

$$\xi_o = r_o(x)/\lambda(x) = r_o(x_1) = \text{constant} \tag{7}$$

Moreover, the swirl velocity v is transformed into a variable proportional to the circulation k, while the radial velocity is scaled by the shape factor

$$k(x,\zeta) = rv(x,r) = \lambda\zeta v \tag{8}$$

$$h(x,\zeta) = w(x,r)/\lambda \tag{9}$$

Using the transformation equations of equations (5), (6), (8) and (9) into equations (1) - (4), we get

$$\frac{\partial(\zeta h)}{\partial\zeta} = -\zeta\frac{\partial u}{\partial x} + \zeta^2\frac{\lambda'}{\lambda}\frac{\partial u}{\partial\zeta} \tag{10}$$

$$\frac{\partial p}{\partial\zeta} = \frac{k^2}{\lambda^2\zeta^3} \tag{11}$$

$$u\frac{\partial u}{\partial x} - \frac{1}{\lambda^2}\frac{\partial^2 u}{\partial\zeta^2} + \left(h - \frac{\lambda'}{\lambda}\zeta u - \frac{1}{\lambda^2\zeta}\right)\frac{\partial u}{\partial\zeta} = \frac{\lambda'}{\lambda^3}\frac{k^2}{\zeta^2} - \frac{\partial p}{\partial x} \tag{12}$$

$$u\frac{\partial k}{\partial x} - \frac{1}{\lambda^2}\frac{\partial^2 k}{\partial\zeta^2} + \left(h - \frac{\lambda'}{\lambda}\zeta u + \frac{1}{\lambda^2\zeta}\right)\frac{\partial k}{\partial\zeta} = 0 \tag{13}$$

Equations (10) - (13) are the governing equations in the computational domain. Equations (10) - (11) are first order equations in h and p; respectively, while equations (12) and (13) are parabolic equations in u and k; respectively. Therefore, the boundary conditions on h and p must be specified on only one boundary; either on the axis or on the boundary ζ_o = const, while the boundary conditions on u and k must be specified on the axis and the outer boundary.

Along the core axis, $\zeta = 0$, the following boundary conditions are imposed:

$$\frac{\partial u(x,0)}{\partial\zeta} = k(x,0) = h(x,0) = 0 \tag{14}$$

The first condition expresses the fact that the axial velocity is symmetrical about the axis. The second condition requires the circulation to vanish on the axis; i.e., a rigid body motion exists in the limit as the axis is approached. The third condition requires the radial velocity to vanish in the absence of sources or sinks on the axis. On the outer surface, the following boundary conditions must be specified:

$$u(x,\zeta_o) = u_o(x),\ k(x,\zeta_o) = k_o(x),\ p(x,\zeta_o) = p_o(x) \tag{15}$$

The functions $u_o(x)$, $k_o(x)$, and $p_o(x)$ are provided by the inviscid solution of the outer flow obtained in Section II.4.

The initial conditions at the initial station x_1 are given by

$$u(x_1,\zeta) = u_1(\zeta),\ k(x_1,\zeta) = k_1(\zeta) \tag{16}$$

These profiles are obtained from experimental data or from previous approximate solutions. Alternatively, they may be obtained from the three dimensional viscous flow solution on the wing surface.

III.3. The Finite Difference Technique and Quasilinearization

In this section, we develop the basic difference equations required to determine a function or its derivatives along the axial and radial directions with second-order accuracy. Next, we develop a "quasilinearization technique" to linearize the nonlinear terms in the equations.

Figure 17 shows a rectangular computational domain covered by a grid system consisting of constant x and ζ lines. Subscript m refers to the point number in the x direction while subscript n refers to the point number in the ζ direction. The developed equations are evaluated at the x_c location which is defined as follows:

$$x_c = x_m + a\,.\,\Delta x = x_m + a(x_{m+1} - x_m) \tag{17}$$

where $a + b = 1$

Expanding the functions $G_{m,n}$ and $G_{m+1,n}$ about point (c,n), adding and neglecting terms of $O(\Delta x)^2$ or higher, we get

$$G_{c,n} = bG_{m,n} + aG_{m+1,n} + O(\Delta x)^2 \tag{18}$$

Subtracting the two expansions $G_{m,n}$ and $G_{m+1,n}$, we get

$$\frac{\partial G_{c,n}}{\partial x} = \frac{G_{m+1,N} - G_{m,n}}{\Delta x} - \frac{\Delta x}{2}(b-a)\frac{\partial^2 G_{c,n}}{\partial x^2} + O(\Delta x)^3$$

By letting $b-a=O(\Delta x)$, the second term on the right becomes of $O(\Delta x)^2$ and the equation can be truncated there and we get

$$\frac{\partial G_{c,n}}{\partial x} = \frac{G_{m+1,n} - G_{m,n}}{\Delta x} + O(\Delta x)^2 \qquad (19)$$

Expanding $G_{c,n+1}$ and $G_{c,n-1}$ about point (c,n), subtracting and adding the equations, we obtain the following equations; respectively

$$\frac{\partial G_{c,n}}{\partial \zeta} = \frac{G_{c,n+1} - G_{c,n-1}}{2\Delta\zeta} + O(\Delta\zeta)^2 \qquad (20)$$

$$\frac{\partial^2 G_{c,n}}{\partial \zeta^2} = \frac{G_{c,n+1} - 2G_{c,n} + G_{c,n-1}}{(\Delta\zeta)^2} + O(\Delta\zeta)^2 \qquad (21)$$

Substituting eq. (18) into eqs. (20) and (21), we get

$$\frac{\partial G_{c,n}}{\partial \zeta} = \frac{a(G_{m+1,n+1} - G_{m+1,n-1}) + b(G_{m,n+1} - G_{m,n-1})}{2\Delta\zeta} + O(\Delta\zeta)^2 \qquad (22)$$

$$\frac{\partial^2 G_{c,n}}{\partial \zeta^2} = \frac{a(G_{m+1,n+1} - 2G_{m+1,n} + G_{m+1,n-1})}{(\Delta\zeta)^2} + \frac{b(G_{m,n+1} - 2G_{m,n} + G_{m,n-1})}{(\Delta\zeta)^2} + O(\Delta\zeta)^2 \qquad (23)$$

Next, we consider the "Quasilinearization Technique." Equations (10) - (12) include nonlinear terms, e.g.; $u\frac{\partial u}{\partial x}$, $v\frac{\partial u}{\partial \zeta}$, . . . etc. which produce nonlinear algebraic terms in the finite difference form. Since the solution of nonlinear equations is time consuming, one needs to linearize these terms. For this purpose, we consider Taylor's expansions of two functions $G_{m+1,n}$ and $H_{m+1,n}$ about $G_{m,n}$ and $H_{m,n}$; respectively, and form the linearized expression of a typical nonlinear term $G_{m+1,n}\,H_{m+1,n}$

$$G_{m+1,n}\,H_{m+1,n} = G_{m+1,n}\,H_{m,n} + G_{m,n}\,H_{m+1,n} - G_{m,n}\,H_{m,n} + O(\Delta x)^2 \qquad (24)$$

Since the governing equations are evaluated at point (c,n), a typical nonlinear term at this point is linearized as follows

$$G_{c,n}\,H_{c,n} = a[G_{m+1,n}\,H_{m,n} + G_{m,n}\,H_{m+1,n} + (R-1)\,G_{m,n}\,H_{m,n}] + O(\Delta x)^2 \qquad (25)$$

where $R=b/a$ (26)

It should be noted that eqs. (18) and (24) are used to derive eq. (25).

III.4. Difference Equations of the Governing Equations

Continuity Equation

Equation (10) is evaluated at point $(c,n-\frac{1}{2})$. Using the difference expressions developed in the preceding section, one obtains the following equation:

$$h_{m+1,n} = \left(\frac{n-\frac{1}{2}}{n-1}\right) h_{m+1,n-1} + R\left[\left(\frac{n-\frac{1}{2}}{n-1}\right) h_{m,n-1} - h_{m,n}\right] + \frac{\Delta r}{4a}\left(\frac{2n-3}{n-1}\right)\left([Rv_m\,(2n-3) + 1]\,u_{m,n} - [Rv_m\,(2n-3) - 1]\,u_{m,n-1} + [v_m\,(2n-3) - 1]\,u_{m+1,n} - [v_m\,(2n-3) + 1]\,u_{m+1,n-1}\right) \qquad (27)$$

where

$$v_m = \frac{\lambda_{m+1} - \lambda_m}{\lambda_{m+1} + R\lambda_m}, \quad A_r = \frac{\Delta\zeta}{\Delta x} \qquad (28)$$

ζ-Momentum Equation

Equation (11) is evaluated at point $(c,n-\frac{1}{2})$. Using the difference expressions developed in the preceding section, one obtains the following equation:

$$p_{m+1,n-1} = p_{m+1,n} + R(p_{m,n} - p_{m,n-1}) + \frac{2a\,\beta_n}{(2n-3)^3}\left[R(k_{m,n} + k_{m,n-1}) + (k_{m+1,n} + k_{m+1,n-1})\right]^2 \qquad (29)$$

where

$$\beta_n = -1/[a^2\,\Delta\zeta^2(\lambda_{m+1} + R\lambda_m)^2] \qquad (30)$$

φ-Momentum Equation

Equation (12) is evaluated at point (c,n). Using the difference expressions developed in the preceding section, one obtains the following equation:

$$A_n\,k_{m+1,n-1} + B_n\,k_{m+1,n} + C_n\,k_{m+1,n-1} = D_n \qquad (31)$$

where

$$A_n = a(\beta_n + \gamma_n) \qquad (32)$$

$$B_n = \alpha_n - 2a\,\beta_n \qquad (33)$$

$$C_n = a(\beta_n - \gamma_n) \qquad (34)$$

$$D_n = aR(\beta_n + \gamma_n)\,k_{m,n+1} + (\alpha_n + 2b\,\beta_n)k_{m,n} - aR(\beta_n - \gamma_n)k_{m,n-1} \qquad (35)$$

$$\alpha_n = U_{m,n}/\Delta x \qquad (36)$$

$$\gamma_n = \tfrac{1}{2}\left[\frac{a}{\Delta\zeta}\,(Rh_{m,n} + h_{m+1,n})\right.$$

$$\left. - \frac{A_R}{\Delta\zeta}\,(n-1)\,\nu_m(Ru_{m,n} + u_{m+1,n}) - \beta_n/(n-1)\right] \qquad (37)$$

x-Momentum Equation

Equation (13) is evaluated at point (c,n). Using the difference expressions developed in the preceding section, one obtains the following equation:

$$\hat{A}_n\, u_{m+1,n+1} + \hat{B}_n\, u_{m+1,n} + \hat{C}_n\, u_{m+1,n-1} = \hat{D}_n \qquad (38)$$

where

$$\hat{A}_n = a(\beta_n + \psi_n) + \theta_n\, u_{m,n} \qquad (39)$$

$$\hat{B}_n = \alpha_n - 2a\beta_n + \theta_n(u_{m,n+1} - u_{m,n-1}) \qquad (40)$$

$$\hat{C}_n = a\beta_n - a\psi_n - \theta_n\, u_{m,n} \qquad (41)$$

$$\hat{D}_n = \frac{-\nu_m \beta_n}{(n-1)^2\Delta x}\,[2k_{m+1,n}\,k_{m,n} + (R-1)\,k_{m,n}^2]$$

$$- (p_{m+1,n} - p_{m,n})/\Delta x$$

$$+ [\alpha_n + 2b\beta_n - (R-1)(u_{m,n+1} - u_{m,n-1})\theta_n]\, u_{m,n}$$

$$- b(\beta_n + \psi_n)\, u_{m,n+1} - b(\beta_n - \psi_n)\, u_{m,n-1} \qquad (42)$$

$$\psi_n = \tfrac{1}{2}\left[\frac{a}{\Delta\zeta}\,(Rh_{m,n} + h_{m+1,n}) + \beta_n/(n-1)\right] \qquad (43)$$

$$\theta_n = -\frac{(n-1)}{2\Delta x}\,\nu_m \qquad (44)$$

III.5. Method of Solution, Implementation, and Computer Program

III.5.1. Initial Axial Station

Once the axial- and swirl-velocity profiles are specified, equation (16), the initial pressure and initial radial-velocity profiles are calculated from equations (10)-(13). For the initial pressure, equation (11) is evaluated at point $(1,n-\frac{1}{2})$ and we obtain

$$p_{1,n-1} = p_{1,n} - \frac{(k_{1,n} + k_{1,n-1})^2}{4\Delta\zeta^2\,(n-3/2)^3} \qquad (45)$$

This equation is used to calculate the initial pressure.

For the initial radial velocity, we eliminate the axial derivatives in equations (10)-(13) and obtain the following equation

$$\frac{u}{\zeta}\frac{\partial H}{\partial\zeta} + \frac{\partial^2 u}{\partial\zeta^2} - \frac{1}{\zeta}(H-1)\frac{\partial u}{\partial\zeta} = \int_0^{\zeta} I\, d\zeta \qquad (46)$$

where

$$H = \zeta h \text{ and } I = \frac{2k}{u\zeta^3}\left[\frac{\partial^2 k}{\partial\zeta^2} - \frac{1}{\zeta}\,(H+1)\,\frac{\partial k}{\partial\zeta}\right] \qquad (47)$$

To obtain the difference equation of eq. (46), we evaluate the equation at point $(1,n-\frac{1}{2})$. The integral on the right-hand side is evaluated by using the trapezoidal rule. The resulting equation is

$$H_{1,n} = \frac{1}{u_{1,n-1}}\left[H_{1,n-1}\,u_{1,n} - u_{1,n} + u_{1,n-1}\right.$$

$$\left. - 4(n-3/2)(u_{1,n-2} - u_{1,n-\frac{1}{2}} + u_{1,n-1})\right]$$

$$+ \frac{\Delta\zeta^2(n-3/2)}{u_{1,n-1}}\left[\frac{\Delta\zeta}{4}\,(I_{1,n-1} + I_{1,n-\frac{1}{2}})_{n\geq 2}\right.$$

$$\left. + \frac{\Delta\zeta}{2}\,(I_{1,1} + I_{1,n-1})_{n\geq 3} + \Delta\zeta\Big(\sum_{2}^{n-2} I_{1,i}\Big)_{n\geq 4}\right] \qquad (48)$$

III.5.2. Subsequent Stations

Here, iteration must be used to obtain the solutions for λ_{m+1}, $h_{m+1,n}$, $p_{m+1,n}$, $k_{m+1,n}$ and $u_{m+1,n}$. The shape factor λ_{m+1} which signifies the expansion of the viscous core in the downstream direction can be determined by iteration or by assuming that the outer boundary is a stream surface. If the shape of the outer boundary is prescribed, then λ_{m+1} is already known. Next, we describe the steps used to proceed in the downstream direction using equations (27), (29), (31) and (39).

i. Equation (27) is used to calculate $h_{m+1,n}$. Starting at $n = 2$, we march toward $n = N + 1$. On the right hand side $h_{m+1,n-1}$, $h_{m,n-1}$, $h_{m,n}$, $u_{m,n}$ $u_{m,n-1}$ and ν_m are known while $u_{m+1,n}$ and $u_{m+1,n-1}$ are unknown. The latter values are initially extrapolated from the preceding station values $u_{m,n}$ and $u_{m,n-1}$. (During the iteration cycles, they are assumed equal to the recently calculated values of the preceding iteration.)

ii. Equation (31) is used next to calculate $k_{m+1,n}$. Following the Tridiagonal Algorithm, we obtain the following recurrence equations.

$$I_n = \frac{D_n - C_n\,I_{n-1}}{B_n + C_n\,J_{n-1}}\,,\quad J_n = \frac{-A_n}{B_n + C_n\,J_{n-1}} \qquad (49)$$

$$I_1 = J_1 = 0 \qquad (50)$$

$$k_{m+1,n} = I_n + J_n\,k_{m+1,n+1} \qquad (51)$$

Starting at $n = 2$, we march toward $n = N$ to calculate I_n and J_n using eqs. (49) and (50). Since the value of $k_{m+1,N+1}$ is known from the boundary conditions, we march backward from $n = N$ to $n = 2$ to calculate $k_{m+1,n}$ using eq. (51). The unknown value of $u_{m+1,n}$, eq. (37), is initially extrapolated

from the preceding station value $u_{m,n}$. (During the iteration process, they are assumed equal to the recently calculated values of the preceding iteration.)

iii. Equation (29) is used next to calculate $P_{m+1,n-1}$ starting from n = N + 1 and marching toward n = 2.

iv. Equation (38) is used next to calculate $u_{m+1,n}$. The following recurrence equations are used:

$$L_n = \frac{\hat{D}_n - \hat{C}_n L_{n-1}}{\hat{B}_n + \hat{C}_n M_{n-1}}, \quad M_n = \frac{-\hat{A}_n}{\hat{B}_n + \hat{C}_n M_{n-1}} \tag{52}$$

$$L_1 = 0, \; M_1 = 1 \tag{53}$$

$$u_{m+1,n} = L_n + M_n u_{m+1,n+1} \tag{54}$$

Here, we march upward and backward in the same way as step iii using equations (52) - (54).

v. Steps i-iv are repeated until the calculated values converge.

vi. Next, we march to the next axial station. It should be noted that if convergence failed at any or took large number of iteration cycles, this indicates that the breakdown point may be reached. The boundary-layer-like equations are not valid in this region and one has to resort to the Navier-Stokes equations.

III.5.3. Computer Program

A computer program is written to implement the developed method of solution. The Main Program reads the boundary conditions and initial conditions either in the form of discrete values or in the form of analytic expressions. It also reads the step size $\Delta\zeta$, aspect ratio of the grid A_r, number of steps N in the ζ direction, the parameter a, and the ratio R. The main program interacts with several subroutines.

Two subroutines are devoted to the initial conditions; the first calculates the initial pressure profile $P_{1,n-1}$ while the second calculates the profile of initial radial velocity $h_{1,n}$.

Another five subroutines are used to calculate λ_{m+1}, $h_{m+1,n}$, $k_{m+1,n}$, $P_{m+1,n-1}$ and $u_{m+1,n}$. These subroutines are successively called in the main program within a continuous iterative loop until the values of h, k, p and u converge at two successive cycles of iteration. If convergence is not reached at any downstream station after a prescribed number of iterations, the program stops. This is an indication that this station is closely upstream of the breakdown station. If the program converges at all stations, it is stopped after a prescribed distance in the axial direction. In the case of the leading-edge vortex core, the program stops after a distance equals to one and one-half the wing root chord.

A Plotting Subroutine is also included to plot the profiles h, k, p and u at any desired station.

Figure 18 shows a flow chart of the main features of the computer program.

III.6. Numerical Examples

Preliminary numerical examples have been considered to check the developed computer program. In this paper, the results for a trailing-edge vortex core calculations are presented. Typical velocity profiles for the initial viscous-core flow are used. This example was considered earlier by Hall[48]. The application to a leading-edge vortex core, with boundary conditions obtained from the inviscid model, is currently considered. The DEC-10 Computer of the Old Dominion University Computer Center is used to carry out the calculations.

For the trailing-edge vortex core, the following initial conditions are used:

At $x_1 = 0.25$, we have

$$u(x_1,\zeta) = 1 - 0.25 \exp(-\zeta^2),$$

$$k(x_1,\zeta) = 0.5[1-\exp(-\zeta^2)]$$

For the boundary conditions, the following conditions are used:

At $\zeta_0 = 6.0$ and for $0.25 \le x \le 1.0$, we have

$u(\zeta_0,x) = 1.0$, $k(\zeta_0,x) = .5$, $p(\zeta_0,x) = 1.0$

The shape factor of the outer boundary is considered constant; $\lambda(x) = 1.0$. In the axial direction, 15 stations are taken ($\Delta x = 0.05$), while in the radial direction, 80 stations are taken ($\Delta\zeta = 0.075$). The factor R is taken to be 1.0. Figure 19 shows the axial- and swirl-velocity profiles at x = 0.25, 0.5, 0.75 and 1.0. One can see the strong interaction between the axial and swirl velocities. As the swirl velocity decreases in the downstream direction, the axial-velocity deficit 1-u decreases too. These results agree exactly with those of reference 48. The results of the linear theories[52,53] are also included in the figure. The computational time for this case took 4.0 seconds of CPU time.

IV. Concluding Remarks

Integrated numerical methods are developed for the inviscid and viscous solutions of highly swept-back wings at large angles of attack. The results of the MNDV-method are remarkably successful in predicting Hummel's experimental data. The developed viscous program, based on the first order boundary-layer-like equations, successfully reproduces Hall's numerical results. Currently, accurate near-field calculations of the inviscid model are developed to provide the boundary conditions needed for the viscous solutions of the leading- and trailing-edge cores.

Acknowledgement

The viscous part of this research work is supported under Contract No. N62269-80-C-0704 from the Naval Air Development Center, Warminster, PA. The inviscid part is supported under Grant No. NSG 1560 from NASA Langley Research Center, VA.

References

1. Peckham, D. H., "Low-Speed Wind-Tunnel Tests on a Series of Uncambered Slender Pointed Wings with Sharp Edges," British ARC R & M No. 3186, December 1958.

2. Kummel, D., "Study of Flow Around Sharp-Edged Slender Delta Wings with Large Angles of Attack," NASA TT F-15, 107, September 1973.

3. Wentz, W. H., "Effects of Leading-Edge Camber on Low-Speed Characteristics of Slender Delta Wings," NASA CR-2002, 1972.

4. Bergeson, A. H. and Porter, J. D., "An Investigation of the Flow Around Slender Delta Wings with Leading-Edge Separation," Princeton University, Department of Aeronautical Engineering, Report No. 510, May 1960.

5. Hummel, D., "On Vortex Formation Over a Slender Wing at Large Angles of Incidence," AGARD CP-247, January 1979.

6. Smith, J. H. B., "Improved Calculations of Leading-Edge Separation from Slender Delta Wings," Proc. Roy. Soc. Land. A 306, 1968.

7. Private discussions with Prof. Dietrich Hummel during the 11th Congress of ICAS, Lisbon, Portugal, September 10-16, 1978 and during the AGARD Symposium on High Angle of Attack Aerodynamics, Sandefjored, Norway, October 4-6, 1978.

8. Elle, B. J. and Jones, J. P., "A Note on the Vorticity Distribution on the Surface of Slender Delta Wings with Leading-Edge Separation," J. Roy. Aero-Soc., 65, 1961, pp. 195-198.

9. Hummel, D., and Redeker, G., "Experimentelle Bestimmung der gebunden Wirbellinien sowie des Stromungsverlaufs in der Umgebung der Hinter-Kante eines Schlanken Delta Flugels, Abhandlg. d. Braunschw. Wiss. Ges, 22, 1972, pp. 273-290.

10. Johnson, F. T., Tinoco, E. N., Lu, P. and Epton, M. A., "Recent Advances in the Solution of Three-Dimensional Flows Over Wings with Leading Edge Vortex Separation," AIAA paper No. 79-0282, January 1979.

11. Campbell, J. F., "Vortex Flow Aerodynamics-An Emerging Design Capability," Astronautics & Aeronautics, Volume 19, No. 5, May 1981, pp. 54, 56, 58.

12. Hall, M. G., "Vortex Breakdown," Annual Review of Fluid Mechanics, Vol. 4, Annual Reviews Inc., Palo Alto, Calif., 1972.

13. Bossel, H. H., "Vortex Equations: Singularities, Numerical Solution, and Axisymmetric Breakdown," NASA CR-2090, July 1972.

14. Smith, J. H. B., "A Review of Separation in Steady, Three-Dimensional Flow," AGARD Conference Proceedings No. 168 on Flow Separation, AGARD-CP-168, November 1975.

15. Kandil, O. A., Chu, L. and Yates, Jr., E.C., "Hybrid Vortex-Method for Lifting Surfaces with Free Vortex Flow," AIAA paper No. 80-0070, AIAA 18th Aerospace Sciences Meeting, January 1980.

16. Legendre, R., "E'coulement du Vaisinage de la Pointe Avante d'une dile a Forte Flache dux Incidences Moyenes, "La Recherche Aeronautique No. 31, 1953.

17. Brown, C. E. and Michael, W. H., "Effect of Leading Edge Separation on the Lift of a Delta Wing," Journal of Aeronautical Sciences," Vol. 31, Oct. 1954, pp. 690-694.

18. Mangler, K. W. and Smith, J. H. B., "Calculation of the Flow Past Slender Delta Wings with Leading Separation," RAE Rept. 2593, May 1957, Royal Aircraft Establishment, Farnsborough, England.

19. Gersten, K., "Calculation of Nonlinear Aerodynamic Stability Derivatives of Aeroplanes," AGARD Rep. 342, April 1961.

20. Garner, H. C. and Lehrian, "Nonlinear Theory of Steady Forces on Wings with Leading-Edge Flow Separation," R & M 3375, Feb. 1963, Aeronautical Research Council, London.

21. Pullin, D. K., "Calculations of the Steady Conical Flow Past a Yawed Slender Delta Wing with Leading Edge Separation," Imperial College of Science and Technology, Lond., I. C. Aero Report 72-17, July 1972.

22. Jones, I. P., "Flow Separations from Yawed Delta Wings," Computers and Fluids, Vol. 3, 1975, pp. 155-177.

23. Cohen, M. J. and Nimri, D., "Aerodynamics of Slender Rolling Wings at Incidence in Separated Flow," AIAA Journal, Vol. 14, No. 7, July 1976, pp. 886-893.

24. Belotserkovskii, S. M., "Calculation of the Flow Around Wings of Arbitrary Planforms Over a Wide Range of Angles of Attack," NASA TT F-12, 391, 1969.

25. Rehbach, C., "Calculation of Flow Around Zero-Thickness Wings with Evolute Vortex Sheets," NASA TT F-15, 183, 1973.

26. Kandil, O. A., "Prediction of the Steady Aerodynamic Loads on Lifting Surfaces Having Sharp-Edge Separation," Ph.D. Dissertation, Dept. of Engr. Sci. and Mechanics, Virginia Polytechnic Institute and State University, December 1974.

27. Rehbach, C., "Numerical Investigation of Vortex Sheets Issuing from Separation Line Near the Leading Edge," NASA TT F-15, 530, 1974.

28. Kandil, O. A., Mook, D. T., and Nayfeh, A. H., "Nonlinear Prediction of the Aerodynamic Loads on Lifting Surfaces," Journal of Aircraft, Vol. 13, No. 1, January 1976, pp. 27-28.

29. Kandil, O. A., Mook, D. T., and Nayfeh, A. H., "A Numerical Technique for Computing Subsonic Flow Past Three Dimensional Canard-Wing Configurations with Edge Separation," AIAA paper No. 77-1, January 1977.

30. Kandil, O. A., Atta, E. H., and Nayfeh, A. H., "Three Dimensional Steady and Unsteady Asymmetric Flow Past Wings of Arbitrary Planforms," AGARD CP-227, February 1978. Also NASA CR 145 235, September 1977.

31. Kandil, O. A., "Asymmetric Flow Past Wings at Large Incidence with Small Amplitude Oscillations," AIAA paper No. 78-1336, August 1978.

32. Kandil, O. A. and Page, M., "A Nonlinear Discrete-Vortex-Perturbation Method for the Unsteady Lifting-Surface Problems with Edge Separations," 11th Congress of ICAS, Lisbon, Portugal, September 1978.

33. Kandil, O. A., "State of the Art of Nonlinear Discrete-Vortex Methods for Steady and Unsteady High Angle of Attack Aerodynamics," AGARD CP-247, January 1979.

34. Belotserkovskii, S. M. and Nisht, M. I., "Non Stationary Nonlinear Theory of a Thin Wing of Arbitrary Planform," Mekhanika Zhidkosti Gasa, No. 4, 1974, pp. 100-108.

35. Rom, J., Almosnino, D. and Zorea, C., "Calculation of the Nonlinear Aerodynamic Coefficients of Wings of Various Shapes and their Wakes Including Canard Configurations," 11th Congress of ICAS, Lisbon, Portugal, September 1978.

36. Kandil, O. A., Mook, D. T., and Nayfeh, A. H., "New Convergence Criteria for the Vortex Lattice Models of the Leading-Edge Separation," NASA SP-405, No. 16, May 1976, pp. 285-300.

37. Johnson, F. T. and Rubbert, P. E., "Advanced Panel-Type Influence Coefficient Methods Applied to Subsonic Flows," AIAA paper No. 75-50, January 1975.

38. Weber, J. A., Brune, G. W., Johnson, F. T., Lu, P. and Rubbert, P. E., "Three Dimensional Solution of Flows Over Wings with Leading Edge Vortex Separation," AIAA Journal, Vol. 14, 1976, pp. 519-525.

39. Johnson, F. T., Lu, P., Brune, G. W., Weber, J. A. and Rubbert, P. E., "An Improved Method for the Prediction of Completely Three-Dimensional Aerodynamic Load Distributions on Configurations with Leading-Edge Separation," AIAA paper 76-417, 1976.

40. Kuhlman, J. M., "Analytical Studies of Separated Vortex Flow on Highly Swept Wings," NASA CR 3022, Nov. 1978.

41. Reddy, C. S., "Theoretical Study of Aerodynamic Characteristics of Wings Having Vortex Flow," NASA CR 159184, Nov. 1979.

42. Hoeijmakers, H. W. M., and Bennekers, B., "A Computational Method for the Calculation of the Flow about Wings with Leading-Edge Vortices," AGARD CP-247, January 1979.

43. Smith, J. H. B., "Inviscid Fluid Models, Based on Rolled-up Vortex Sheets, for Three-Dimensional Separation at High Reynolds Number," RAE Technical Memorandum AERO 1738, November 1977.

44. Polhamus, E. C., "Technical Evaluation Report on the FDPS on High Angle of Attack Aerodynamics," AGARD AR-145, August 1979.

45. Chu, L., "Nonlinear Hybrid-Vortex Method for Wings Having Side-Edge Separations," M. S. thesis, Old Dominion University, Norfolk, VA, December 1980.

46. Kandil, O. A., "Numerical Prediction of Vortex Cores from the Leading and Trailing Edges of Delta Wings," ICAS paper No. 14.2, The 12th Congress of the International Council of the Aeronautical Sciences, Munich, Germany, October 1980.

47. Gratshore, I. S., "Some Numerical Solutions for the Viscous Core of an Irrotational Vortex," Aero-Rept. LR-378, National Research Council, Canada 1963.

48. Hall, M. G., "A Numerical Method for Solving the Equations for a Vortex Core," British ARC R&M No. 3467, May 1965.

49. Hall, M. G., "The Structure of Concentrated Vortex Cores," Progress in Aeronautical Sciences, Vol. 7, Pergamon Press, Oxford, 1966, pp. 53-110.

50. Raat, J., "Vortex Development and Breakdown," AFFDL-TR-75-69, May 1975.

51. Wilson, J. D., "Calculation of Vortex Breakdown Locations for Flow over Delta Wings," Journal of Aircraft, Vol. 14, No. 10, October 1977, pp. 1020-1022.

52. Newman, B. G., "Flow in a Viscous Trailing Vortex," Aero. Quart., Vol. X, 1959, pp. 149-162.

53. Batchelor, G. K., "Axial Flow in Trailing Line Vortices," Journal of Fluid Mechanics, Vol. 20, 1964, pp. 645-658.

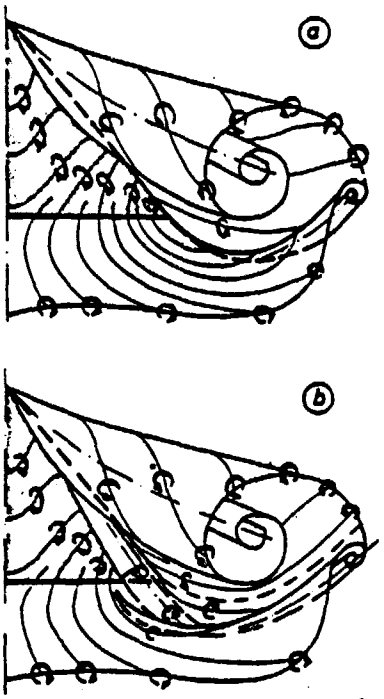

Figure 1. Vortex formation behind a slender delta wing (schematic) a) Elle and Jones (Ref. 8). Hummel and Redeker (Ref. 9) b) Hummel (Ref. 5).

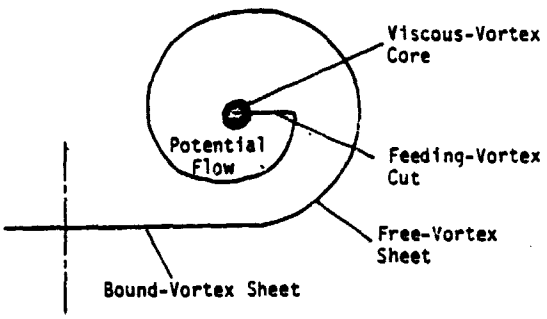

a. MODEL NO. 1

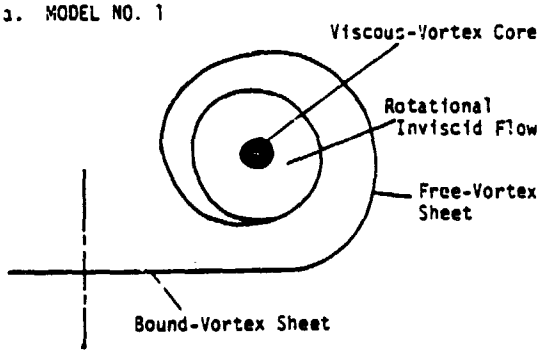

b. MODEL NO. 2

Figure 2. Models of Viscous-Vortex Cores

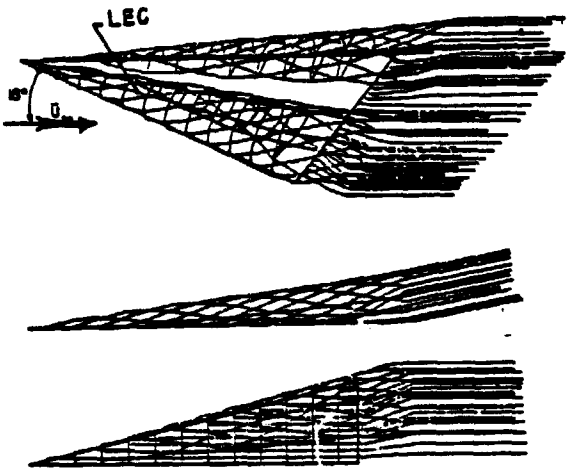

Figure 3. Typical solution of the leading-edge vortex sheet, AR = 1, 12 x 12 lattice; Kandil, et.al. (Ref. 36).

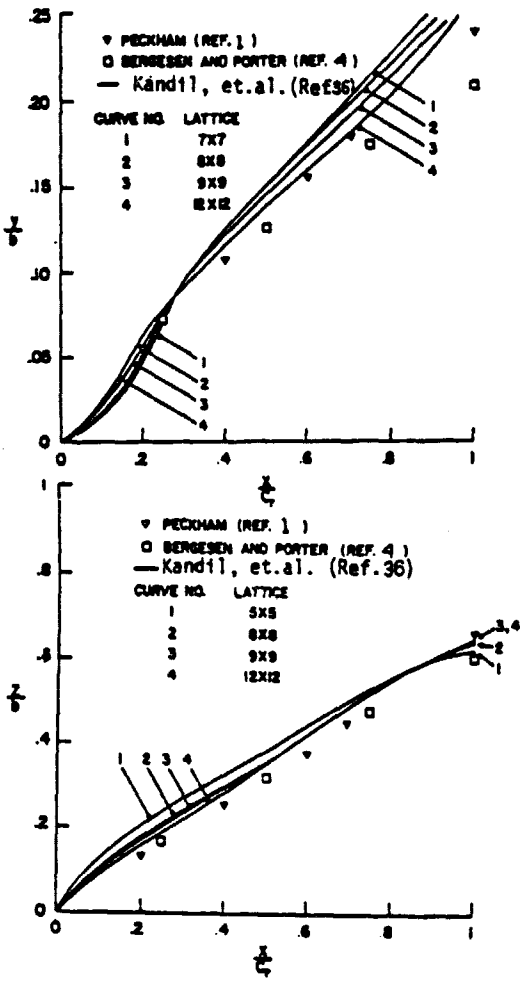

Figure 4. Height and spanwise position of the leading-edge core, AR = 1, $\alpha = 15^{0}$; Kandil, et.al. (Ref. 36).

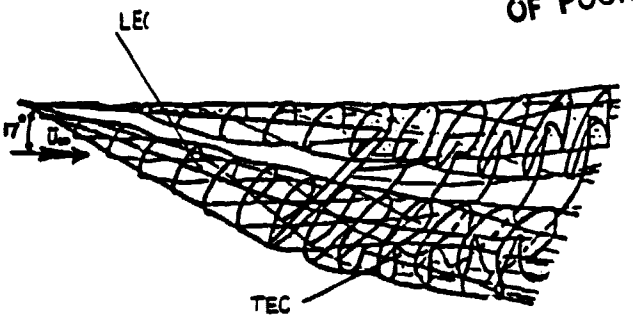

Figure 5. Typical solution of the leading- and trailing-edge vortex sheets, AR = 1, 7 x 7 lattice, NDV-Method.

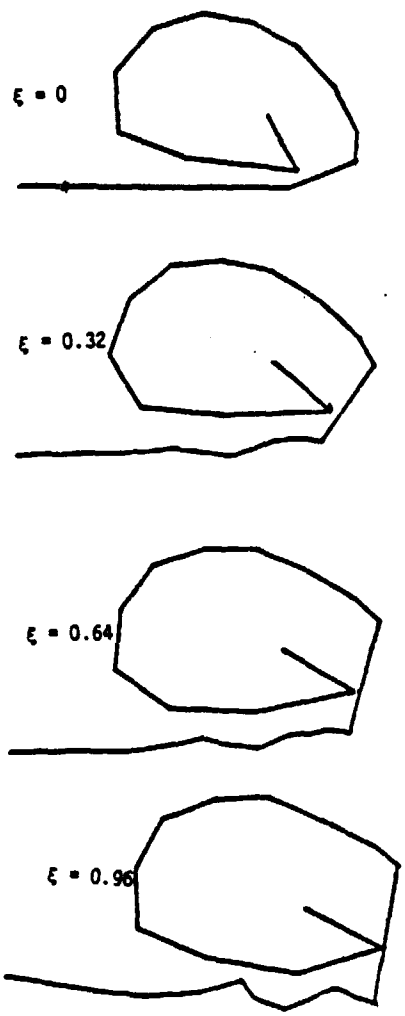

Figure 6. Leading- and trailing-edge sheets behind a delta wing in planes perpendicular to the wind direction, AR = 1, $\alpha = 17^0$, 7 x 7 lattice, NDV-Method.

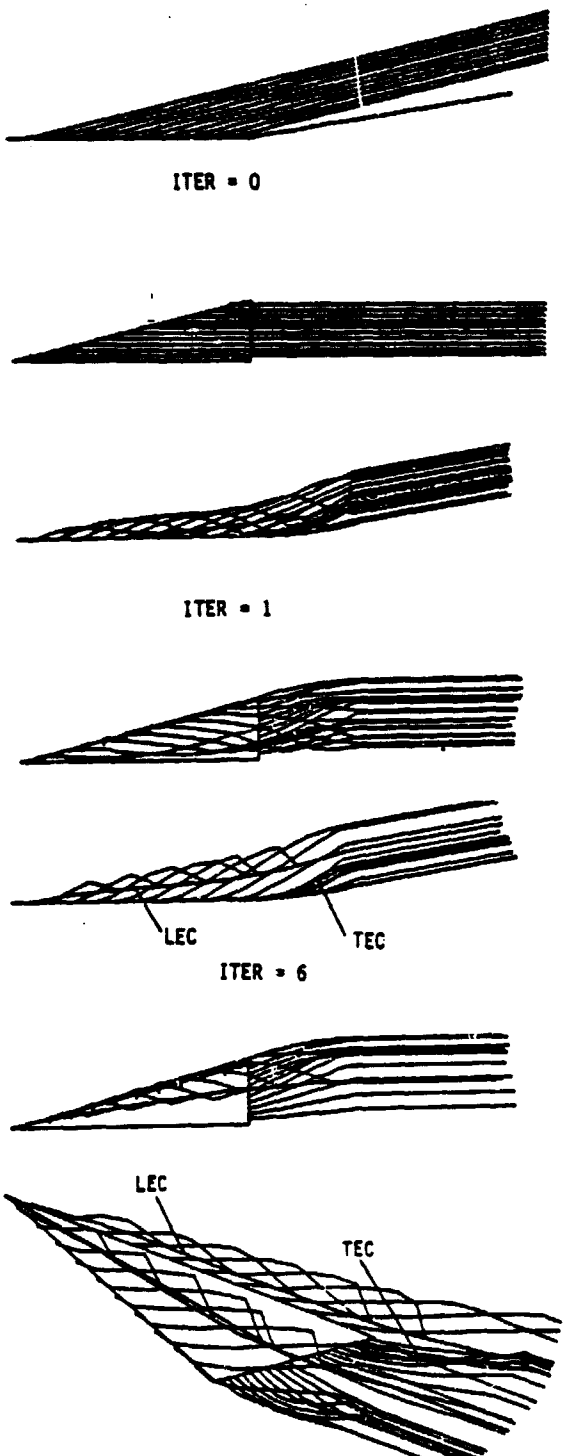

Figure 7. Typical solutions at different iteration steps; ITER = 6 is the converged solution showing the leading- and trailing-edge cores in two- and three-dimensional views; AR = 1, $\alpha = 20.5^0$, 10 x 10 lattice, 1/4 turn, MRDV-Method.

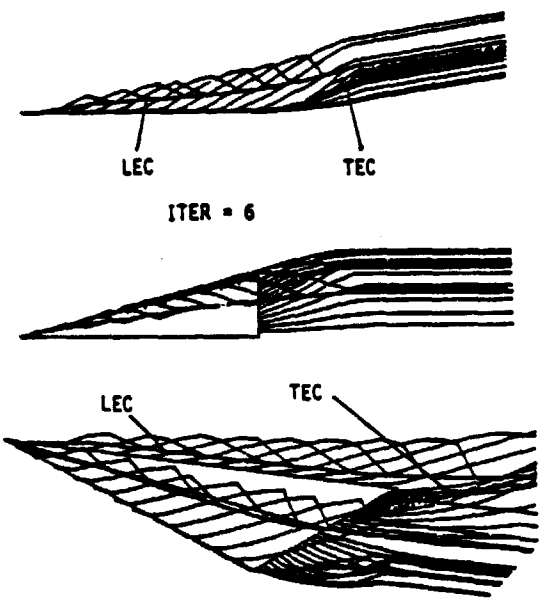

Figure 8. Converged solution showing the leading- and trailing-edge cores in two- and three-dimensional views; AR = 1, $\alpha = 20.5^{0}$, 12 x 12 lattice, 1/4 turn, MNDV-Method.

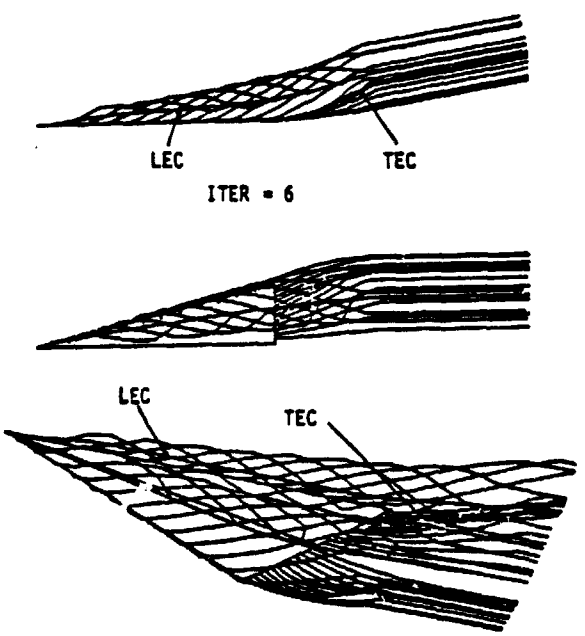

Figure 9. Converged solution showing the leading- and trailing-edge cores in two- and three-dimensional views; AR = 1, $\alpha = \alpha = 20.5^{0}$, 12 x 12 lattice, 1/2 turn, MNDV-Method.

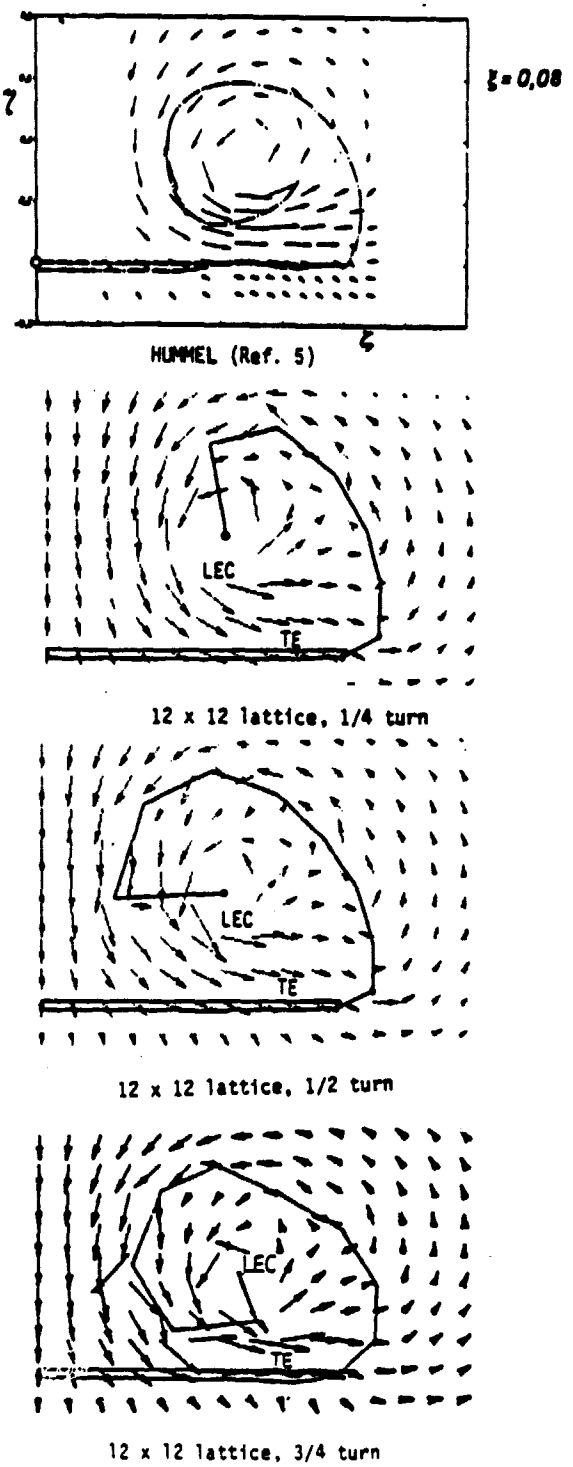

Figure 10. Leading- and trailing-edge sheets and flow direction in a plane perpendicular to the wind direction with different turns, AR = 1, $\alpha = 20.5^{0}$, $\zeta = 0.08$, $|\overline{V_{yz}}/U_{\infty}| = 1$.

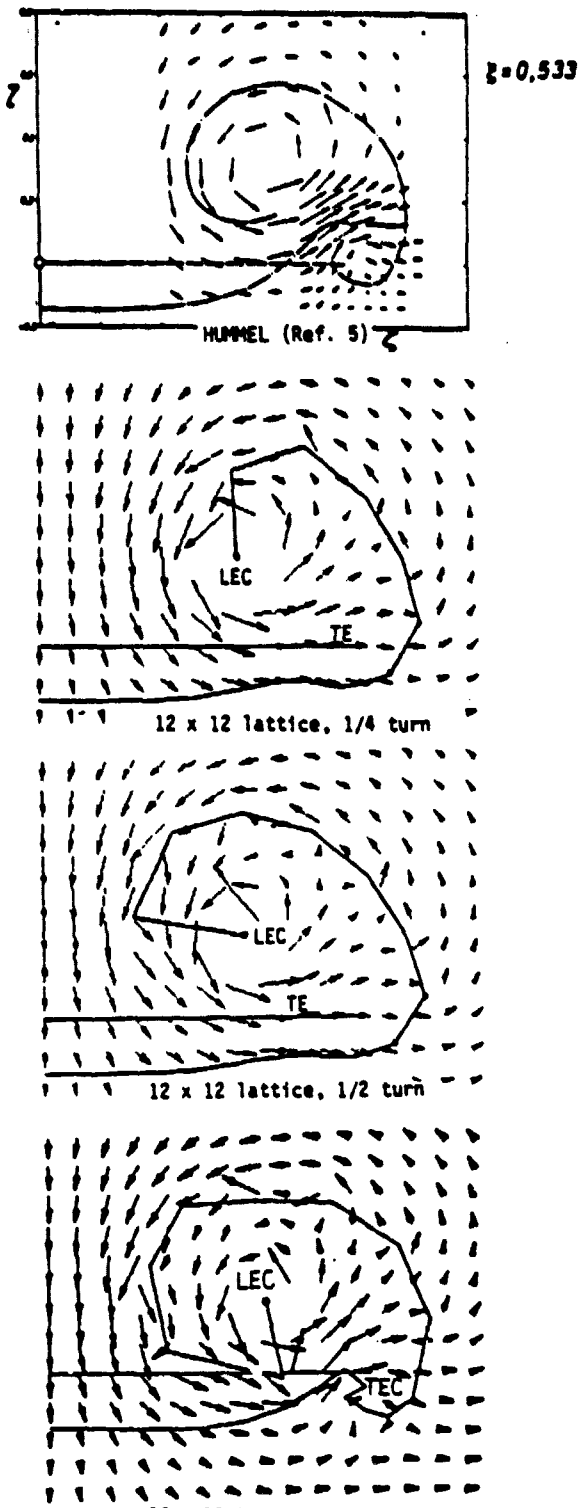

Figure 11. Leading- and trailing-edge sheets and flow direction in a plane perpendicular to the wind direction with different turns, AR = 1, $\alpha = 20.5^0$, $\varepsilon = 0.5333$.

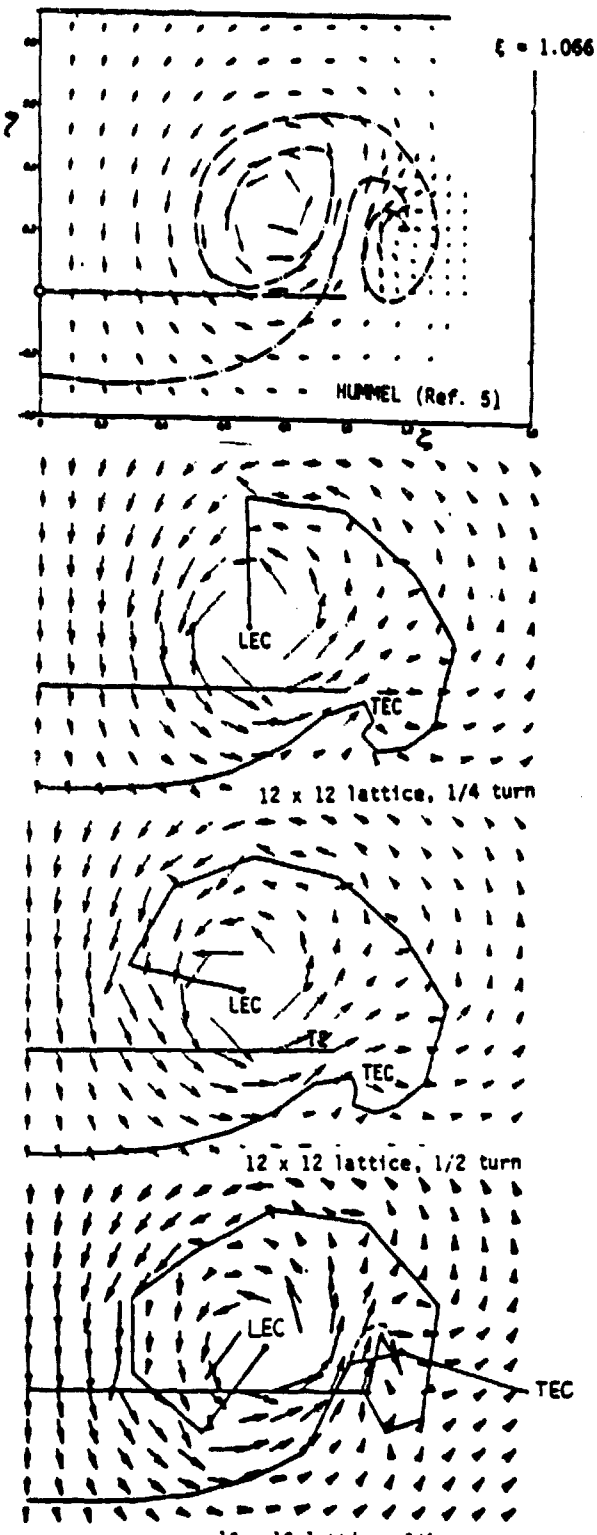

Figure 12. Leading- and trailing-edge sheets and flow direction in a plane perpendicular to the wind direction with different turns AR = 1, $\alpha = 20.5^0$, $\varepsilon = 1.066$.

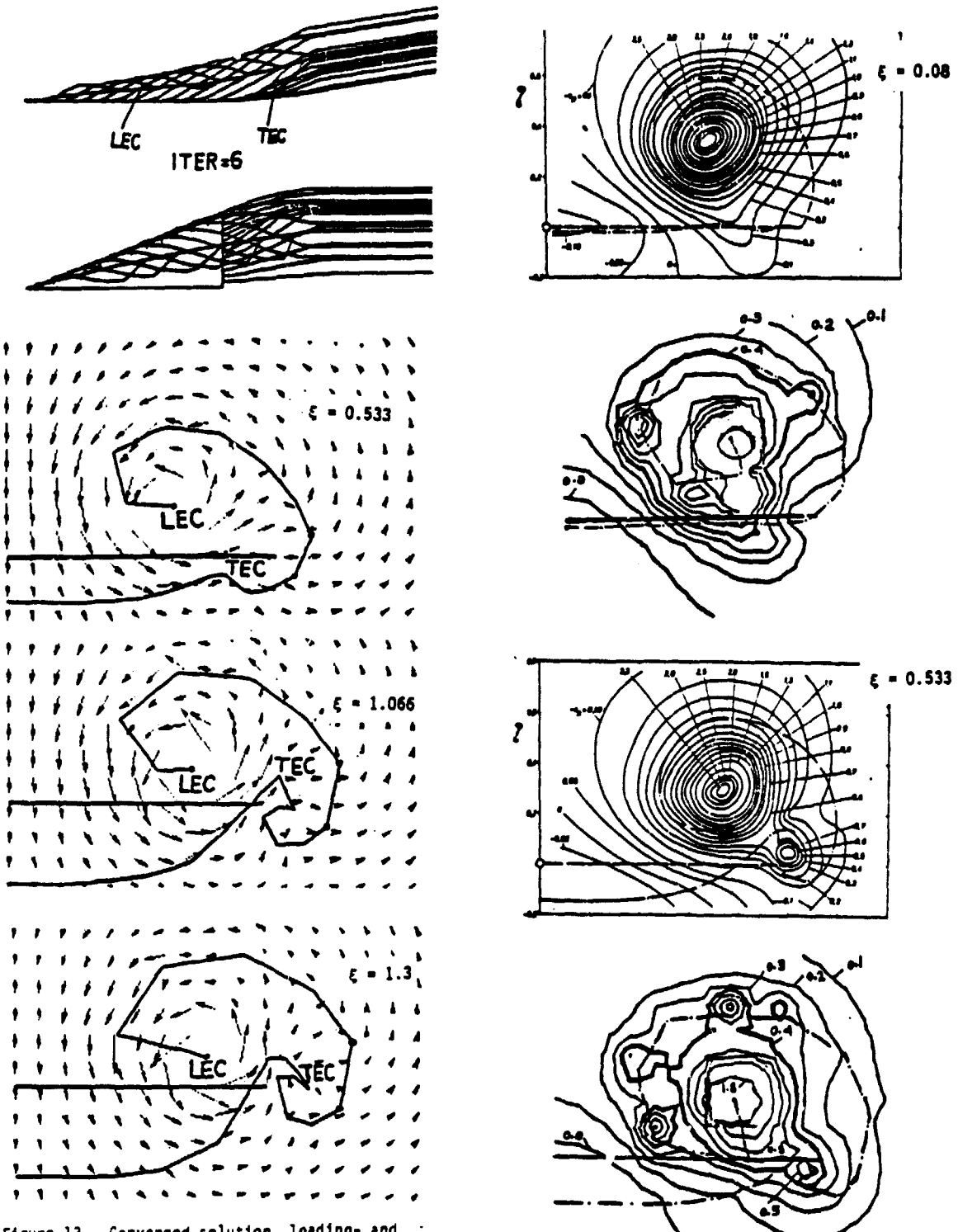

Figure 13. Converged solution, leading- and trailing-edge sheets, and flow direction in different planes perpendicular to the wind direction, AR = 1.45, $\alpha = 20.5^{\circ}$, 12 x 12 lattice, 1/2 turn.

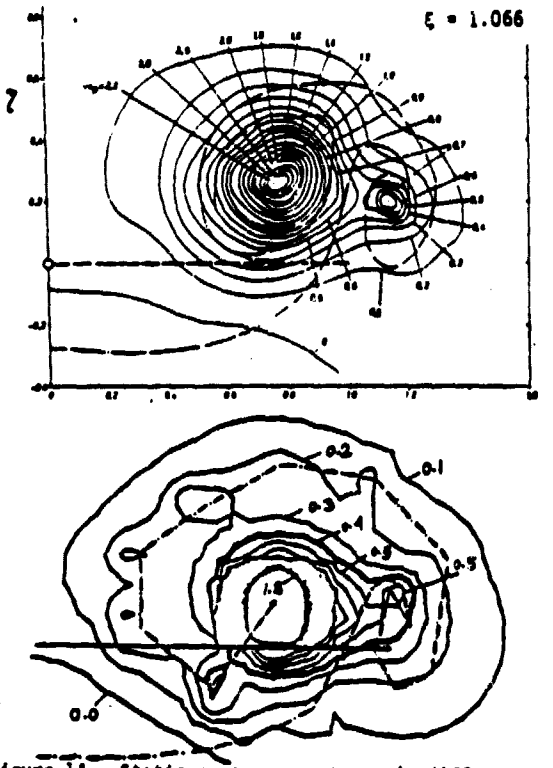

Figure 14. Static pressure contours in different planes perpendicular to the wind direction, AR = 1, $\alpha = 20.5^0$, 12 x 12 lattice, 3/4 turn.

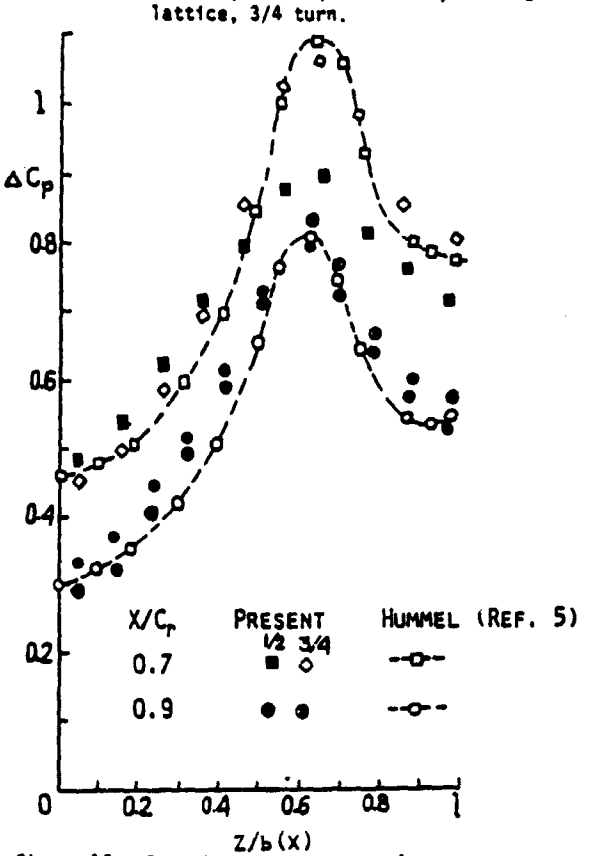

Figure 15. Spanwise net surface pressure variation, $\alpha = 20.5^0$, 12 x 12 lattice.

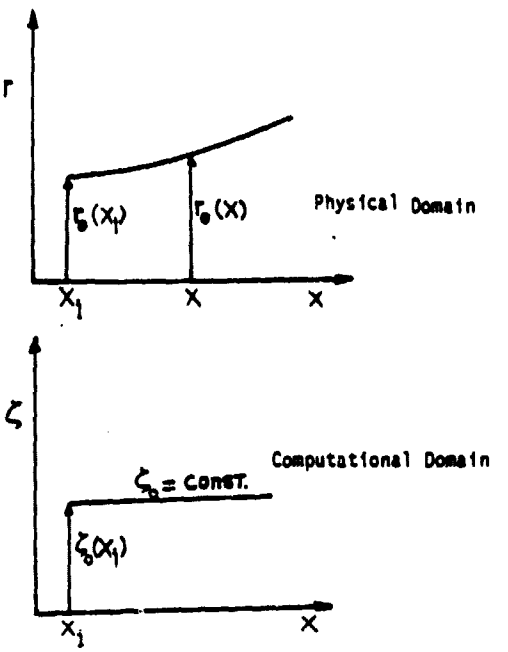

Figure 16. Transformation of Physical Domain.

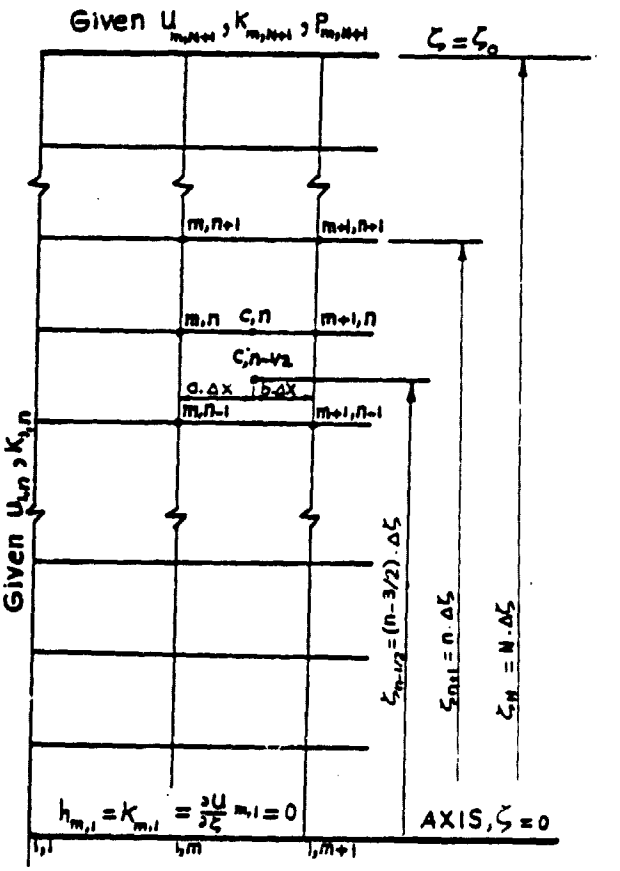

Figure 17. Finite-Difference grid system.

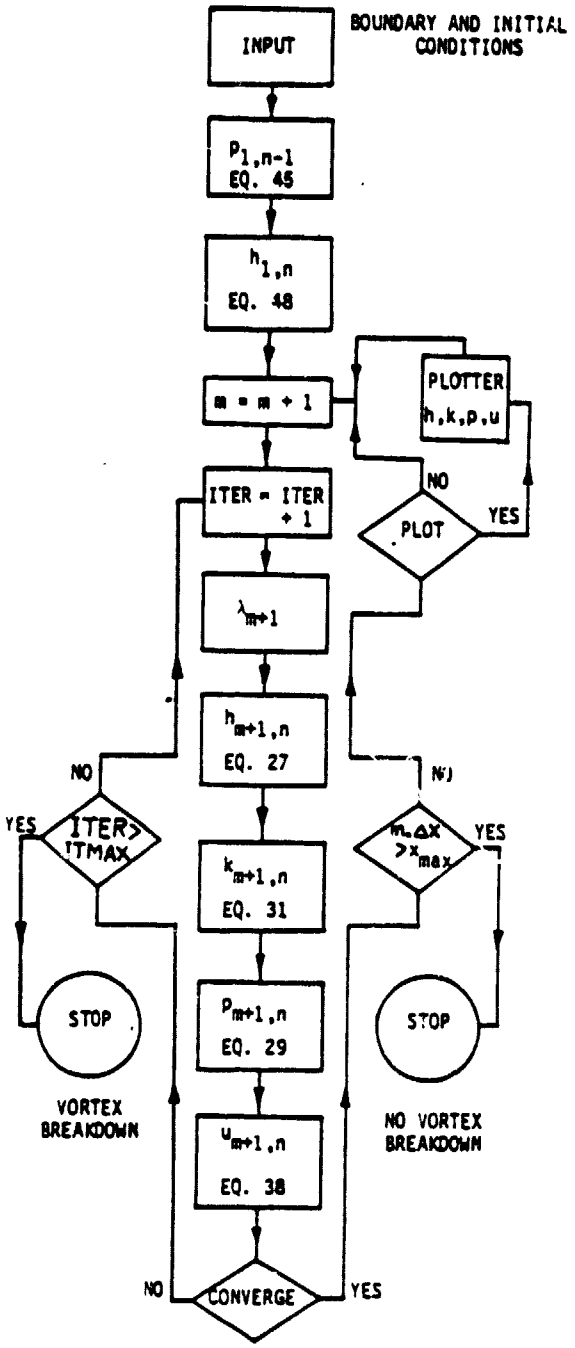

Figure 18. Flow Chart of the Computer Program.

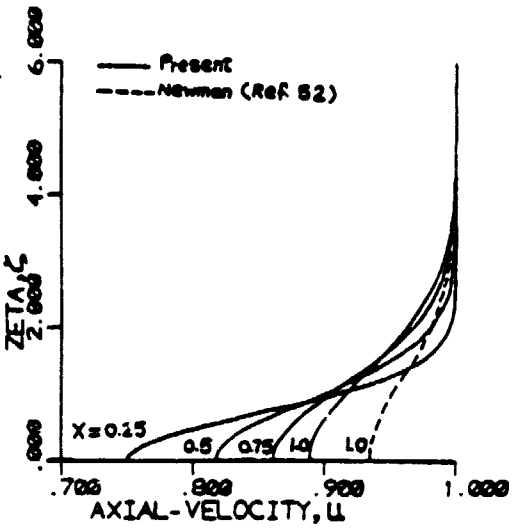

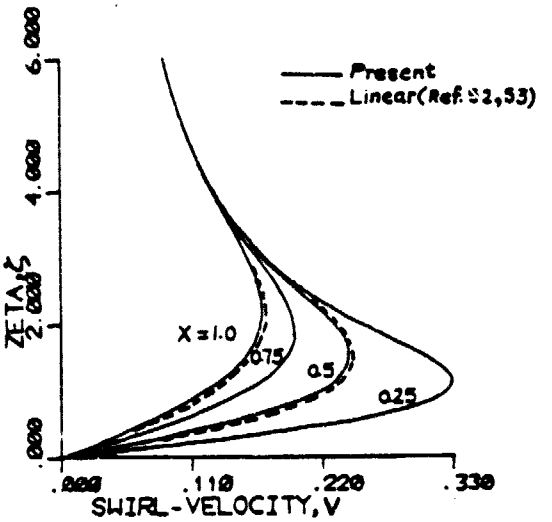

Figure 19. Present solutions for the axial- and swirl-velocity profiles for the trailing-edge vortex core considered in reference 48.

- INTERNATIONAL CENTER FOR TRANSPORTATION STUDIES

INTERNATIONAL SCHOOL OF APPLIED AERODYNAMICS

STEADY AND UNSTEADY INCOMPRESSIBLE FREE-WAKE ANALYSIS

OSAMA A. KANDIL

ASSOCIATE PROFESSOR-DEPT. OF MECHANICAL ENGINEERING AND MECHANICS

OLD DOMINION UNIVERSITY, NORFOLK, VIRGINIA - USA

1st Course on Computational Methods in Potential Aerodynamics

Amalfi - ITALY, May 29/ June 5, 1982

STEADY AND UNSTEADY INCOMPRESSIBLE FREE-WAKE ANALYSIS

Dr. Osama A. Kandil, Associate Professor
Department of Mechanical Engineering and Mechanics
Old Dominion University, Norfolk, Va. 23508, USA
Tel. 804-440-3720

ABSTRACT

The first part of this lecture covers detailed descriptions of the flows around highly sweptback wings and bodies of revolution at high angle of attack. Next, inviscid model approximations and mathematical formulation of the problem are given for steady and unsteady incompressible flows. A general presentation of the methods of solution is given with emphasis on the modern computational techniques. Detailed descriptions of the nonlinear vortex-lattice and vortex-panel techniques are presented to show how the boundary conditions are enforced using iteration.

Typical numerical results are compared with the available experimental data. The lecture ends with concluding remarks regarding the existing computational techniques and the outstanding problems in this area.

IN RECENT YEARS, accurate analysis and reliable prediction of vortex flows have become extremely important to aerodynamicists dealing with modern designs of fighter aircrafts,[1] missiles[2] and helicopters.[3] Modern fighter aircrafts fly at high angles of attack during take-off, offensive and defensive maneuvering, approach and landing. In this range of angle of attack, vortex flows develop around the aircraft with dominant effects on its aerodynamic characteristics and controllability. Modern designs of missiles require high launch angles of attack and high maneuverability within which a very complex vortex flow develops. For helicopters, the interaction of a blade with the vortex wake of another blade affects its operating performance, vibration and noise characteristics. In forward speeds, blade slap, a predominant source of external noise, occurs due to the rapid time rates of change of the blade pressure developing from its passage through a tip vortex of a preceding blade. Examples of these vortex flows are given in Figure 1.

For all these applications, one has to deal with strong nonlinear aerodynamics. Compressibility and separation of the flow are the main sources of the strong nonlinear effects. As the flow Mach number changes from low subsonic to transonic and supersonic, the flow undergoes several qualitative changes and shock waves (detached or attached)[6,7] appear in the flow. As the angle of attack increases from low to moderate and high values, the lift- and pitching-moment coefficients become nonlinear functions of the angle of attack. This nonlinear behavior of the total loads is attributed to flow separations, from the wing edges (side and leading edge) and the body leeward side, in the form of vortex sheets that roll up into strong vortex cores.

Prediction of the coupled effects of nonlinearities; compressible and separated flow nonlinearities, is currently receiving considerable efforts from researchers working in the computational fluid dynamics area, but it is far from being complete. In the supersonic flow regime, a few successful attempts based on the finite difference solution of Euler's equations exists.[8,9] In the transonic flow regime, nothing is available yet and several efforts have just started.

In the present lecture, I am going to discuss the nonlinearity due to flow separation only. Compressibility effects will be presented using the Prandtl-Glauert transformation. The full nonlinear compressibility effects will be presented in the next lecture using the integral equation formulation (Green's function solutions). In this regard, the lecturer has presented[10] a steady nonlinear vortex lattice technique which accounts for the full nonlinear compressibility terms in the nonlinear potential equation. Flow compressibility in this technique is modeled by volume-source distribution within a finite volume around the body. The technique has not been numerically tested yet but work is underway using a similar technique which includes shock capturing using the artificial compressibility method of reference 11.

The first part of this lecture covers a description of the flow based on the available experimental measurements. This is followed by the inviscid model approximations and the mathematical formulation of the steady and unsteady problems. A general presentation of the methods of solutions is given with emphasis on the modern computational techniques. Detailed descriptions of the nonlinear vortex-lattice and vortex-panel techniques are presented to show how the boundary conditions are enforced using iteration. Typical numerical results are compared with

the available experimental data. The lecture ends with concluding remarks regarding the existing computational techniques and the outstanding problems in this area.

Major portions of this lecture are based on earlier published papers, reports and theses[10,12-22] by the lecturer, his collaborators and his students.

DESCRIPTION OF THE FLOW FIELD

In the low-subsonic to transonic speed range, numerous experimental data are available for vortex flows about highly swept back wings[23-38] and bodies of revolution[39-51] at an angle of attack.

HIGHLY SWEPT BACK WINGS-The fluid flow past such wings is characterized by flow separations from side and leading edges due to strong cross flows. The flows from the pressure and suction sides of the wing leave at the side and leading edges to form free-shear layers. The separated free-shear layers roll up spirally and form two vortex cores which are continuously fed by vorticity shed from the attached boundary layers on the wing surfaces through the free-shear layers. This type of flow separation is known as the "primary separation." It has a dominant effect on the aerodynamic characteristics due to the large strength of its vortex core and its prximity to the upper surface of the wing. It generates a large suction pressure peak on the upper surface under the primary vortex core.

The primary separation lines of wings with sharp leading and side edges are fixed along these edges and hence they are known a priori. In the case of rounded edges, the separation lines are inboard of the edges and are not known a priori. Hence a viscous model or perhaps an empirical formula is needed to locate these lines.

The adverse pressure gradient outboard of the suction peaks affects the boundary layer flow on the upper surface and "secondary separation" from the wing surface occurs. The secondary separated flow forms either an additional free shear layer or a bubble depending on the angle of attack. In the range of moderate to large angles of attack, the secondary free-shear layer rolls up spirally in an opposite sense to that of the primary shear layer and forms a secondary vortex core with a strength much smaller than that of the primary core and of opposite sense. The effect of secondary separation depends on the type of boundary-layer flow on the upper surface. For a laminar boundary layer, the secondary core produces another lower pressure peak between the secondary and primary lines of separation. For a turbulent boundary layer, such a pressure peak is hardly noticed, and the primary pressure peak is slightly higher than that of the laminar boundary-layer flow.[4]

A third type of flow involving a "tertiary" separation may occur between the lines of secondary and primary separation due to the adverse pressure gradient created by the secondary vortex core. Figure 2 gives a schematic of these flow separations.

The free-shear layer emanating from the trailing edge is of opposite strength to that of the primary free-shear layer. Within a short distance behind the trailing edge (a distance of a 1/4 root-chord length for a delta wing of aspect ratio of one at 20.5° angle of attack), the trailing free-shear layer rolls up spirally in an opposite sense to that of the primary free-shear layer and forms two counter rotating

vortex cores. The trailing-edge vortex core has the same sense of rotation and almost the same spanwise location as those of the secondary vortex core, although each originates from a different phenomenon. The former is due to an edge separation while the latter is due to a surface separation. Hummel[4] concluded from his latest experimental measurements for turbulent boundary layers at the trailing edge that the secondary-vortex core decays rapidly behind the trailing edge and its remains roll up into the trailing vortex.

Predicting the correct formation of the trailing-edge vortex core is essential for predicting the correct aerodynamic loads near the wing trailing edge due to its proximity to this dege. Moreover, a correct prediction is of paramount importance to problems involving high-angle-of-attack aerodynamics for the canard-wing configurations.

The size of the primary-vortex core and viscosity of the flow within a narrow region around the core centerline play important roles in the aerodynamic characteristics of low-aspect ratio wings at large angles of attack. For these types of wings, it is well known that the lift coefficient increases nonlinearly with the increase in the angle of attack. This is attributed to the increase of the strength of the primary vortex core. However, the increase in the lift coefficient is limited by the occurrence of vortex-core breakdown over the wing and hence there exists a maximum angle of attack corresponding to the maximum lift, Figure 3.

The phenomenon of vortex-core breakdown is defined as an abrupt increase in the core diameter. It occurs due to the adverse swirl-induced pressure gradients along the core axis. Using the radial component of the momentum equation of the boundary-layer like equations (for quasi-cylinderical vortex cores), one can show that an increase in the swirl velocity of the flow, due to an increase in the core strength, increases the axial pressure gradient along the core axis. Therefore, the flow near the core axis loses its axial momentum and swelling of the vortex core develops.

For moderate angles of attack, vortex-core breakdown develops far downstream from the wing trailing edge. As the angle of attack increases, vortex-core strength increases and the breakdown point travels upstream toward the trailing edge. As the breakdown point approaches the trailing edge, the slope of the lift versus angle of attack curve decreases until the maximum lift is reached. Thereafter, the lift coefficient drops sharply, the breakdown point crosses the trailing edge and the wing stalls.

SLENDER BODIES-Three distinct patterns of flow separation develop on the leeward side of a slender body as it is pitched through three ranges of angles of attack.

At low to moderate angles of attack (6°-25°), two symmetric vortices appear on the leeward side which consist of two counter rotating vortex cores with increasing strength and size in the downstream direction. Vorticity from the boundary-layer flow on the body surface is shed from the separation lines and feeds the vortex cores through roll-up free-shear layers. This type of flow separation is also known as the primary separation. The separated flow has a dominant effect on the pressure distribution on the leeward side. Similar to the flow around delta wings, secondary-flow separation develops also inboard of the primary separation line.

Above the 25° angle of attack, the two continuous feeding free-shear layers break-up asymmetrically at points along the two separation lines and multiple pairs of asymmetric vortex cores form over the leeward side of the body. Each vortex core originates from a separate point on the separation line. Ericsson and Reding[52] conclude that both the "vortex crowding" near the body nose and the degree of freedom of the separation point may contribute to the formation of asymmetric vortices. The resulting asymmetric pattern of vortex cores produces large side forces which can be larger than the normal force.

At very large angles of attack, above 60° angle of attack, the crossflow becomes dominant and unsteady vortex shedding starts. The separated free-shear layers are shed in the form of a Karman vortex street.

APPROXIMATIONS FOR INVISCID ANALYSIS

The experimental results given above show that we are dealing with highly complex flow fields. For highly swept back wings, four different vortex cores (primary, secondary, tertiary, and trailing-edge) have been found and apparently their origins are well understood. For bodies of revolutions, two different vortex cores (primary and secondary) have been found and three different modes of flow separation (steady symmetric, steady asymmetric and unsteady asymmetric) have been identified. For inviscid analysis, certain approximations are adopted so that the resulting potential flow model represents the main features of the real flow to a good degree of accuracy.

For wings, the effect of the tertiary vortex core is very small and can be neglected. The effect of the secondary vortex core is small in symmetric flows particulary when the boundary layer on the suction side is turbulent. Hence, its effect on surface pressures and integrated forces can be neglected without appreciable error under the conditions stated. Thus, we are left with the primary flow separation and the trailing-edge flow separation. For an isolated wing, the effect of deformation of the primary and trailing-edge vortex cores and their feeding free-shear layers is neglected after a distance of about 1/2 to 1 root chord since it is a far field effect. For canard-wing, wing-tail and strake-wing configurations, this effect must be taken into account.

In most inviscid analyses, the attached boundary layers are replaced with bound-vortex sheets while the free-shear layers are replaced with free-vortex sheets. Accordingly, the inviscid region representing the vortex core should be represented by a conical sprial vortex sheet which ends with a concentrated vortex line along the core centerline. Although this theoretical representation of the vortex-core is ideal for the inviscid model, the usage of many turns within the core region creates numerical problems in a three-dimensional model which does not assume slender-body approximations. The numerical problems arise due to the proximity of the vortex layers of the spiral and due to the large number of small-size panels needed to accurately model the turns. However, it was found, according to the numerical results and their excellent comparison with the experimental data, that only one turn of the spiral need to be accurately modeled while the remaining turns of the spiral are replaced by a cut ending with a concentrated vortex line along its edge (Figure 4.)

Since one does not know a priori where the trailing-edge vortex core originates, one has to obtain it as a part of the solution. This has been successfully accomplished, for the first time, by the lecturer[13,15].

In all inviscid wing models, the wing edges are assumed to be sharp so that the separation lines are known a priori and hence viscous modeling is not needed to determine the lines of separations. However, for wings with round edges, viscous modeling is needed to determine these lines. Moreover, vortex-breakdown points are assumed to be far downstream so that the variations in the size of the primary-vortex core can be neglected. In fact, this assumption limits the large angles of attack at which inviscid modeling is applicable. With the vorticity confined to the inner boundary of the flow region (bound- and free-vortex sheets), the resulting model is a potential-flow model governed by Laplace's equation (in incompressible flows) and certain boundary conditions.

For bodies, the effect of secondary separation is also small and can be neglected. Unlike the primary separation of wings, the primary separation lines are not known a priori and hence viscous solutions are needed to locate these lines and determine the strength of shed vorticity (this is a separation from a smooth surface and hence Kutta condition is not applicable). In this regard, the reader is referred to the work of Mendenhall, Spangler and Perkins.[53] Since we are dealing with inviscid analyses only, this problem will not be discussed anymore in the present lecture. The rest of the lecture addresses the steady and unsteady problems of wings with vortex flows.

MATHEMATICAL FORMULATION OF THE GENERAL PROBLEM

The problem is formulated relative to a wing-fixed frame of reference xyz. The x-axis is the wing centerline and the xy-plane is the wing plane of symmetry. The wing is rotating at the angular velocity $\bar{\Omega}$ and the freestream velocity is $\bar{U}_\infty$. The general orientation of the wing is described using the Eulerian angles α, β, and γ, Figure 5, which refer to the angles of attack, yaw and roll; respectively. In terms of these angles and their time rate of change, the dimensionless freestream velocity and the angular velocity are expressed by

$$\bar{e}_\infty = \cos\alpha\cos\beta\,\bar{i} + (-\sin\alpha\cos\gamma + \cos\alpha\sin\beta\sin\gamma)\bar{j} + (\sin\alpha\sin\gamma + \cos\alpha\sin\beta\cos\gamma)\bar{k} \tag{1}$$

$$\bar{\Omega} = (-\dot{\alpha}\sin\beta + \dot{\gamma})\bar{i} + (\dot{\alpha}\cos\beta\sin\gamma + \dot{\beta}\cos\gamma)\bar{j} + (\dot{\alpha}\cos\beta\cos\gamma - \dot{\beta}\sin\gamma)\bar{k} = \Omega_x\bar{i} + \Omega_y\bar{j} + \Omega_z\bar{k} \tag{2}$$

where $\bar{i}$, $\bar{j}$ and $\bar{k}$ are the base unit vectors of the xyz-frame of reference.

The unsteady irrotational ideal flow in the region outside of the wing and its separated vortex sheets is governed by the Laplace's equation

$$\nabla^2\phi = 0 \tag{3}$$

where $\phi(\bar{r},t)$ is the perturbation velocity potential. The no-penetration condition on the wing $s(\bar{r},t)$, relative to the wing fixed frame of reference, is given by

$$\frac{\partial s}{\partial t} + (\bar{e}_\infty + \nabla\phi - \bar{\Omega}x\bar{r})\cdot\nabla s = 0 \quad \text{on } s(\bar{r},t) = 0 \tag{4-a}$$

For a rigid wing, $\frac{\partial s}{\partial t} = 0$ and equation (4-a) reduces to

$$(\bar{e}_\infty + \nabla\phi - \bar{\Omega}x\bar{r})\cdot\bar{n}_s = 0 \qquad \text{on } s(\bar{r}) = 0 \tag{4-b}$$

On the separated free-vortex sheet $w(\bar{r},t)$, the no-penetration condition is given by

$$\frac{\partial w}{\partial t} + (\bar{e}_\infty + \nabla\phi - \bar{\Omega}x\bar{r})\cdot\nabla w = 0 \quad \text{on } w(\bar{r},t) = 0 \tag{5}$$

The no-pressure jump condition on $w(\bar{r},t)$ is obtained from the unsteady Bernoulli's equation

$$C_p(\bar{r},t) = -\nabla\phi\cdot[\nabla\phi + 2(\bar{e}_\infty - \bar{\Omega}x\bar{r})] - 2\frac{\partial\phi}{\partial t} \tag{a}$$

where $C_p(\bar{r},t)$ is the pressure coefficient at any point $\bar{r}$ and at any time t. Forming the pressure jump from equation (a) and equating the result to zero, we obtain

$$\Delta C_p = C_{p1} - C_{p2} = -(\nabla\phi_1 - \nabla\phi_2)\cdot[\nabla\phi_1 + \nabla\phi_2 + 2(\bar{e}_\infty - \bar{\Omega}x\bar{r})]$$

$$- 2\frac{\partial(\phi_1 - \phi_2)}{\partial t} = 0 \tag{b}$$

where the subscripts 1 and 2 refer to the upper and lower surface of the wing; respectively. Rearranging equation (b) and setting

$$\phi_1 - \phi_2 = \Delta\phi \tag{c}$$

one obtains

$$\Delta C_p = -2(\frac{\partial}{\partial t} + \bar{v}_w \cdot \nabla)(\Delta\phi) = -2\frac{D(\Delta\phi)}{Dt} = 0 \tag{d}$$

where $\bar{v}_w$ = velocity of a wake element relative to the xyz-frame of reference

$$= \frac{1}{2}(\nabla\phi_1 + \nabla\phi_2) + \bar{e}_\infty - \bar{\Omega}x\bar{r}$$

Equation (d) represents the theorems of Klelvin and Helmhotlz

$$\frac{D\Gamma}{Dt} = \frac{D}{Dt} \iint \bar{\omega} \cdot \bar{n}_A \, dA = 0 \qquad \text{on } w(\bar{r},t) = 0 \tag{6}$$

of conservation of the circulation and the outflow of vorticity; respectively. In equation (6), $\bar{n}_A$ is a unit normal to the surface A bounded by a closed curve around which the circulation Γ is calculated. Equation (6) simply states that the rate of change of circulation around a closed curve or the rate of change of outflow of vorticity through the surface bounded by this closed curve is zero (following the same fluid particles.)

For uniqueness of the solution, one has to impose the Kutta condition along the edges of separation. Here, Kutta condition is represented by

$$\Delta C_p \Big|_{TE,LE,SE} = 0 \tag{7}$$

Finally, the infinity condition requires that

$$\nabla\phi \to 0 \text{ away from s and w} \tag{8}$$

Equations(1) - (8) are the required equations for the general unsteady flow problem.

For steady and unsteady symmetric flows, equations (1)-(8) are simplified as follows:

STEADY-SYMMETRIC FLOW-For this problem, we set $\bar{\Omega}=0$, $\beta=\gamma=0$ and drop the time dependent terms. The resulting equations are

$$\bar{e}_\infty = \cos\alpha\,\bar{i} - \sin\alpha\,\bar{j} \tag{9}$$

$$\nabla^2\phi = 0 \tag{10}$$

$$(\bar{e}_\infty + \nabla\phi) \cdot \bar{n}_s = 0 \qquad \text{on } s(\bar{r}) = 0 \tag{11}$$

$$(\bar{e}_\infty + \nabla\phi) \cdot \bar{n}_w = 0 \qquad \text{on } w(\bar{r}) = 0 \tag{12}$$

$$\Delta C_p = -2(\bar{n}_w \times \bar{\omega}) \cdot (\bar{e}_\infty + \nabla\phi) = 0 \qquad \text{on } w(\bar{r}) = 0 \tag{13}$$

$$\Delta C_p \Big|_{TE,LE,SE} = 0 \tag{14}$$

$$\nabla\phi \to 0 \text{ away from s and w} \tag{15}$$

UNSTEADY-SYMMETRIC FLOW-For this problem, we set $\beta=\gamma=\dot{\beta}=\dot{\gamma}=0$ and the resulting equations are

$$\bar{e}_\infty = \cos\alpha\,\bar{i} - \sin\alpha\,\bar{j} \tag{16}$$

$$\bar{\Omega} = \Omega_z\,\bar{k} = \dot{\alpha}\,\bar{k} \tag{17}$$

$$\nabla^2\phi = 0 \tag{18}$$

$$(\bar{e}_\infty + \nabla\phi - \bar{\Omega}_z x\bar{r}) \cdot \bar{n}_s = 0 \qquad \text{on } s(\bar{r}) = 0 \tag{19}$$

$$\frac{\partial w}{\partial t} + (\bar{e}_\infty + \nabla\phi - \bar{\Omega}_z x\bar{r}) \cdot \nabla w = 0 \qquad \text{on } w(\bar{r},t) = 0 \tag{20}$$

$$\frac{Dr}{Dt} = 0 \qquad \text{on } w(\bar{r},t) = 0 \tag{21}$$

$$\Delta C_p \Big|_{TE,LE,SE} = 0 \tag{22}$$

$$\nabla\phi \to 0 \qquad \text{away from s and w} \tag{23}$$

EXISTING METHODS OF SOLUTION

Before the Nonlinear Vortex-Lattice [Nonlinear Discrete-Vortex (NDV)] and Nonlinear Vortex-Panel [Nonlinear Hybrid-Vortex (NHV)] methods are discussed in detail, a brief discussion of the existing mathematical models is presented. The literature contains several steady and unsteady inviscid-flow models with various degrees of limitations and drawbacks. These models can be divided into four main groups. Each group is presented and evaluated in the next subsections.

SLENDER-BODY MODELS-This group of models uses slender body and conical flow assumptions.[54-61] Modeling of the primary-vortex core and its feeding sheet was first introduced by Brown and Michael.[55] However, the feeding sheet in their model was taken as a planar surface and hence it did not represent the real rolled-up vortex sheet. Mangler and Smith[56] introduced the first realistic model of the primary-vortex core and its feeding sheet. However, this model does not account for the feeding-sheet deformation in the chordwise direction due to the slender-body assumption. These models satisfactorily predict the pressure distribution on the front portion of the wing surface. In the rear portion, the models fail to predict satisfactory pressure distributions because Kutta condition cannot be satisfied at the trailing edge. Such models were limited to slender delta planforms.

OLD NDV-MODELS-In these models,[10,17-22,62-66] the bound-vortex sheet and the free-vortex sheets are approximated by a set of concentrated vortex lines. The bound-vortex sheet is replaced by a bound-vortex lattice, while the free-vortex sheet is replaced by segmented free-vortex lines (in the case of steady flow) or by a growing free-vortex lattice (in the case of unsteady flow). The boundary conditions are satisfied at certain control points on the bound- and free-vortex system using an iterative technique. Excellent agreement was found[10,22] between calculated and experimental total aerodynamic characteristics, and the agreement between calculated and experimental total aerodynamic characteristics was satisfactory for wings with only side-edge separation. For wings with leading-edge separation, however, the agreement was less than satisfactory for some cases. Although the discrete-vortex model has for many years worked very well for attached-flow problems,[67] when vortex-type separation from leading edges and/or tips

occurs, the free-vortex system lies close to the lifting-surface and the results are found to be sensitive to the model of the primary separated flow. The most obvious drawback of the old model is the lack of a realistic model of the primary vortex core and its feeding vortex sheet.

Although the old NDV-method was almost abandoned in predicting the flow details and the distributed aerodynamic characteristics, the modified NDV-method[13,15] pinpointed and cured most of the problems encountered with the old method. It enjoyed a remarkable success in predicting, for the first time, the latest experimental results of Hummel[4].

DOUBLET-PANEL MODELS-This group of models employs doublet-panels[68-75]. In this method, the wing and its free-vortex sheets are divided into networks of quadrilateral panels. Each panel of the networks representing the wing has a biquadratic local doublet distributions and a bilinear local source distribution. The panels of networks representing the free-vortex sheets have biquadratic local doublet distributions. Source and doublet splines are used to express the distributions of singularities on the networks in terms of discrete values of singularity strength at certain standard points on each network. The boundary conditions and continuity of singularity strengths across abutting networks are enforced at certain standard points on network. The results of this method[73,74] are generally good when the solution converges. Apparently, the difficulty in obtaining convergence is due to the failure in satisfying the continuity of the derivatives of the doublet strength across abutting networks. This is equivalent to the existence of concentrated vortex lines between abutting networks.

The doublet panel method was extended[75] to include the effect of entrainment of the primary vortex cores through an empirical approach. The results indicated that the entrainment increased the normal-force coefficient substantially over the experimental values.

This group of models do not account for the chordwise deformation of the primary-vortex sheet. Consequently, the primary vortex sheet cannot be fed three-dimensionally with the shed vorticity. Moreover, the trailing-edge free-vortex sheet was represented by a "fixed design wake."

NHV-MODELS-This group of models employs a nonlinear hybrid vortex method[12,14,16]. In this method, continuous-vorticity and vortex-line representations of the wing and its separated free-shear layers are used. Continuous vorticity is used in the near-field calculations while discrete vortex-lines are used in the far-field calculations.

The wing and its free-shear layers are divided into planar quadrilateral panels having first-order vorticity distribution. The aerodynamic boundary conditions and continuity of the vorticity distributions are imposed at certain nodal points on the panels. To satisfy these conditions, an iterative technique is followed which alternatively yields the local vorticity distribution on the bound-vortex panels and the shape of the free-vortex panels. This method has been used to calculate the steady distributed and total loads on planar-low-aspect-raio rectangular wings. The results have shown that the spanwise variations of the load coefficients are in good agreement with the experimental data. Comparisons of the results with those of the NDV-method have shown that the hybrid method requires less number of vortex panels for the same accuracy.

NONLINEAR DISCRETE-VORTEX (NDV) METHOD

In this method the basic unknowns are the circulation distribution and the shape of the free-vortex sheets. The following sub-sections give the details of the method.

CONSTRUCTION OF THE DISCRETE-VORTEX METHOD-Figure 6 shows how the discrete vortex model is constructed for a delta wing. Although the example discussed here is for a thin, flat, delta wing, the method is general and is not restricted by the geometrical parameters of the wing; e.g. camber, aspect or thickness ratios or wing planform.

The first step is to divide the wing into rectangular and cropped-delta winglets as shown by the dashed lines in Figure 6.a. A rectangular winglet is aerodynamically represented by a spanwise bound-vortex segment of constant circulation Γ_j. This segment is placed at the quarter-chord length of the winglet (the chord length of the rectangular winglet is the characteristic length of the problem). In addition a control point is placed at the three quarter-chord length. The choice of these positions is suggested by thin airfoil theory. It can be shown that the bound-vortex sheet representing the two-dimensional flow around a flat plate at an angle of attack can be replaced by a point vortex of the same strength as that of the continuous vortex sheet under the following conditions: a) the point vortex is placed at the quarter-chord length and b) the flow tangency condition is enforced at only one point at the three-quarter-chord length.

On the other hand, a cropped-delta winglet is aerodynamically represented by a bound-vortex segment of constant circulation. This vortex segment is directed along the perpendicular from the midpoint of the winglet root chord to its leading edge. With this choice it can be seen that the vorticity of this vortex segment does not have a component along the leading edge and hence the Kutta condition is approximately satisfied along this edge.

Chordwise bound-vortex segments arise due to the differences in the strengths of the neighboring spanwise, bound-vortex segments. In this way, a bound-vortex lattice which replaces the continuous, bound-vortex sheet is constructed. The model is completed by adding free-vortex lines, representing the continuous free-vortex sheets at the ends of the bound-vortex lattice along the edges of separation ; the leading and trailing edges. Each line is divided into a series of small, straight segments (near-wake region) and one semi-infinite vortex line (far-wake region). The upstream end of each segment represents a control point of the wake surface where the kinematic and dynamic boundary conditions are satisfied. The initial positions and shapes of these lines are prescribed. The resulting model is shown in Figure 6b. This model has an unknown circulation distribution and a wake that can be deformed to satisfy the boundary conditions.

The model described above is used to solve the steady-flow problem by satisfying the corresponding boundary conditions. On the other hand, if the problem under consideration is for an unsteady flow which starts from a steady flow situation, then the solution of the steady-flow problem serves as an initial condition to the unsteady problem. Furthermore, if the problem under consideration is for an unsteady flow which arises from an impulsive motion of the wing, then the initial condition corresponds also to the solution of the model given above, but with the wakes removed from the model.

CALCULATION OF THE VELOCITY FIELD-To satisfy the boundary conditions on the wing and its wake and to calculate the surface pressure distribution, one needs an accurate method to calculate the velocity at any field point $\bar{r}_j$ at any time step t_k. If the field point is off the wing and its wake, then the velocity is given by

$$\bar{V}(\bar{r}_j,t_k) = \nabla\phi(\bar{r}_j,t_k) + \bar{e}_\infty - \bar{\Omega}(t_k) \times \bar{r}_j \tag{24}$$

where

$$\nabla\phi(\bar{r}_j,t_k) = \sum_{i}^{n(t_k)} [\Gamma_i(t_k)/4\pi h_i(\bar{r}_j,t_k)][\cos\theta_{1i}(\bar{r}_j,t_k) - \cos\theta_{2i}(\bar{r}_j,t_k)]\bar{e}_i(\bar{r}_j,t_k) \tag{25}$$

is the induced velocity from all the vortex segments of the model. The parameters on the right-hand side of equation (25) are those of Biot-Savart's law[76]. The number of vortex segments $n(t_k)$ is a function of the time step t_k due to the growing vortex lattice in the wake in the unsteady-flow problem. To account for the near-vortex velocity, equation (25) is modified by an artificial viscosity which is obtained from reference 77.

When the field point is on the wing surface or on the wake surface, one has to account for the self-induced tangential velocity due to the local strength of the vortex sheet. Figure 7 shows the parameters involved in calculating the components of the induced tangential velocity in the x and z direction at a point p for a rectangular vortex element in the xz-plane. With linear interpolation, it is easy to show that these components are given by

$$\bar{v}_{tx}(y = 0^{\pm}) = \pm (1/2\ \ell_1^2)[\Gamma_1(x + \ell_1 - x_1) + \Gamma_3(x_1 - x)]\bar{e}_1 \tag{26.a}$$

$$\bar{v}_{tz}(y = 0^{\pm}) = \mp (1/2\ \ell_2^2)[\Gamma_4(z + \ell_2 - z_1) + \Gamma_2(z_1 - z)]\bar{e}_2 \tag{26.b}$$

where the arguments $y = 0^+$ and $y = 0^-$ correspond to the upper surface and the lower surface of the wing, respectively. Equations (26) must be added to equation (24) if one is to calculate the pressure distribution on the upper and lower surfaces by using Bernoulli's equation. Extension of equations (26) to a general, quadrilateral vortex element is straightforward.

BOUNDARY CONDITIONS FOR THE STEADY PROBLEM-The boundary conditions on the wing surface $s(\bar{r})$ and the wake surface $w(\bar{r})$ are satisfied by an iterative process. To initiate the iterative process, one needs to prescribe an initial geometry of the wake surface. It has been found from several numerical tests that the number of iterative cycles required to achieve the solution can be reduced by an appropriate choice of the initial geometry. This initial geometry depends on the problem under consideration and thus it varies from one problem to the other.

For instance, the number of iterative cycles for the steady, symmetric-flow problem is reduced by about 20% when the free-vortex lines emanating from the leading edge are prescribed to be straight lines pitched at one half the wing angle of attack. In addition, those lines emanating from the trailing edge are assumed straight lines pitched at one third the wing angle of attack. Here, the comparison is

made with respect to the number of iterative cycles required for the same problem when all the free-vortex lines are prescribed to be straight lines pitched at an angle equal to the wing angle of attack.

In the case of a steadily, rolling wing at zero angle of attack, an appropriate initial guess is found to be related to an angle $\theta(\bar{r}) = \pm 1/2 \tan^{-1}|\bar{\Omega}x\bar{r}|/U_\infty$. Here, we specify the free-vortex lines emanating from the edges of the advancing and receding sides to be straight lines pitched at the angles $+\theta$ and $-\theta$; respectively.

Next, the flow-tangency condition and the spatial conservation of circulation are satisfied at the control points and node points, respectively, of the bound-vortex lattice. Thus, we obtain a set of linear algebric equations which yeilds the circulation distribution Γ_j.

With the circulation distribution fixed, the kinematic and dynamic boundary conditions at the control points of the free-vortex lines are satisfied. For steady flows, these two conditions are combined into a simple condition in which we require that each vortex segment in the wake be aligned with the local velocity at its upstream end (a control point on the wake surface). This means that each vortex segment is a segment of a streamline (kinematic condition). Moreover, it means that the force on each vortex segment is zero according to Kutta-Jawkowski theorem in the small (dynamic condition). This process is carried out by calculating the downstream end of each vortex segment according to

$$\bar{r}_{j+1} = \bar{r}_j + \bar{V}_j \ell_j / |\bar{V}_j| \qquad (27)$$

where $\bar{r}_j$ and $\bar{r}_{j+1}$ are the position vectors of the upstream and downstream ends, respectively, ℓ_j is the segment length and $\bar{V}_j$ is the velocity at its point [equation (24) for steady flows].

The iteration scheme moves back and forth from the control points of the bound-vortex lattice to the control points of the free-vortex lines until convergence is achieved. We consider the iteration scheme converged when the variation in the circulation distribution or the displacement of the downstream ends of the free-vortex segment between two seccessive iteration cycles does not exceed a certain prescribed tolerance. Once convergence is achieved, we calculate the pressure distribution and the total load coefficients.

BOUNDARY CONDITIONS FOR THE UNSTEADY PROBLEM-Here, we consider the problem of unsteady flow which starts from a steady flow situation. The continuous motion of the wing is discretized into a series of impulsive changes occuring at discrete time steps. At each time step t_k, a set of starting vortices develops along the edges of separation and are shed with the local velocities to restore the smoothness of flow at the edges (Kutta condition). In the same time, the starting vortices shed in the wake at earlier time steps are convected downstream with the local velocities without changing their strengths. This process satisfies the kinematic condition on the wake (a wake element moves along the direction of the local velocity) and it also satisfies the dynamic condition on the wake (a wake element satisfies Kelvin-Helmholtz theorem).

The position of any shed vortex $\bar{r}_j$ at any time step t_k is determined by

$$\bar{r}_j(t_k) = \bar{r}_j(t_{k-1}) + (t_k - t_{k-1})\bar{V}_j(\bar{r}_j, t_{k-1}) \tag{28}$$

where t_{k-1} is the preceding time step and $\bar{V}_j$ is given by equation (24). The strength of any newly shed vortex is related to the change in the bound circulation. Hence, with the positions of the shed vortices known from equation (28) and with the strength of the newly shed vortices given in terms of the change of the bound circulation, the flow tangency condition at the control points of the wing yields the unknown circulation distribution. To account for the error in equation (28) (because of using the velocity $V_j(\bar{r}_j,t_{k-1})$ at the preceding time step t_{k-1} rather than the current time step t_k), an iteration procedure similar to that of the steady-flow problem is performed.

In both the steady and unsteady flows, the only difference between the symmetric and asymmetric problems is the longer computational time required for the latter problem as compared to that of the former problem. In the former problem, we need only to use half the wing to obtain the solution because of the flow symmetry. In the latter problem, the whole wing must be used to obtain the solution.

CALCULATION OF THE PRESSURE COEFFICIENT-The distribution of the pressure coefficient on the upper and lower surfaces of the wing is calculated by using Bernoulli's equation in terms of a wing-fixed frame of reference.

$$C_p(\bar{r}_j^{\pm},t_k) = -[\bar{V}(\bar{r}_j^{\pm},t_k)]^2 + 2\bar{V}(\bar{r}_j^{\pm},t_k)\cdot[\bar{\Omega}(t_k)\times\bar{r}_j - \bar{e}_\infty] - 2\frac{\partial\phi(\bar{r}_j,t_k)}{\partial t} \tag{29}$$

where

$$\bar{V}(\bar{r}_j^{\pm},t_k) = \nabla\phi(\bar{r}_j,t_k) + \bar{v}_{tx}(\bar{r}_j^{\pm},t_k) + \bar{v}_{tz}(\bar{r}_j^{\pm},t_k) \tag{30}$$

$\bar{r}_j^{\pm}$ is the position vector of the control point, the positive and negative superscripts refer to the upper surface and lower surface of the wing, respectively, and $\nabla\phi$, $\bar{v}_{tx}$ and $\bar{v}_{tz}$ are given by equations (25), (26.a) and (26.b), respectively. The pressure is calculated at the control points of the bound-vortex lattice because these are the points where the flow tangency condition is enforced.

In the steady-flow problem, the last term of the right-hand side of equation (29) is zero and all the other terms are time independent.

The net pressure coefficient is given by

$$\Delta C_p(\bar{r}_j,t_k) = 4[\bar{v}_{tx}(\bar{r}_j^{+},t_k) + \bar{v}_{tz}(\bar{r}_j^{+},t_k)]\cdot[\bar{\Omega}(t_k)\times\bar{r}_j - \bar{e}_\infty - \nabla\phi(\bar{r}_j,t_k)] - 2[\Gamma(\bar{r}_j,t_k) - \Gamma(\bar{r}_j,t_{k-1})/(t_k - t_{k-1})] \tag{31}$$

The total-load coefficients are obtained by integrating the net pressure coefficient on the wing.

NUMERICAL EXAMPLES; NDV-METHOD-Figures 8-15 show typical solutions of free-vortex sheets emanating from side, leading and trailing edges of isolated wings, a canard-wing configuration and a wing-body combination for steady symmetric and asymmetric flows and for unsteady symmetric flows.

In figure 8, the arrangement of the bound-vortex lattice used for rectangular wings is also shown. It is noticed that the tip vortex covers about 13% of the wing semi-span and hence its effect on the spanwise pressure distribution is confined in this region.

In figure 9, Rehbach's solution[64] for a delta wing of aspect ratio of 1 is shown. Starting with the solution of a rectangular wing, he progressively deform the wing leading edge to obtain the solution of the delta wing; a time consuming process. The present NDV-method solves the problem directly without going through this deformation process. Although the arrangement of the bound-vortex lattice of the present method differs from Rebach's (compare Figure 6.b and 9.4), the final shapes of the leading-edge vortex lines are the same.

Figure 10 shows the solution for a delta wing of aspect ratio of 0.7. Figure 11 shows the solution for the same wing which is now steadily rolled at zero angle of attack. Notice the antisymmetric roll up of the leading-edge vortex lines.

Figure 12 shows the solution for a yawed delta wing and the relative sizes of the leading-edge vortex sheets emanating from the windward and leeward sides.

In Figure 13, it is seen that the vortex trail of the canard is deflected inboard of the main wing toward its plane of symmetry. It also moves downwards toward the surface of the main wing. This produces a downwash on the central part of the main wing and an upwash on its tip region.

In Figure 14, the solution of the leading-edge vortex for a wing-body combination without leeward-side separation from the body is given.

Figure 15 shows the development of the leading- and trailing-edge vortex system for a delta wing undergoing a sinusoidal pitching motion.

Figures 16-21 show samples of the computed total and distributed loads for the cases considered above.

It is seen from figure 16 that the section-lift peak near the wing tip moves inboards as the angle of attack increases. In the linear case, indicated by the dotted lines, the tip vortex is not taken into account and one can see the substantial effect when the tip vortex is included (indicated by the solid lines).

Figures 17 and 18 show the spanwise variation of the pressure coefficient. The suction peak of the pressure coefficient exists almost at the same spanwise location of the center of the leading edge vortex.

Figure 19 shows the pitching-moment coefficient versus the lift coefficient and the lift coefficient versus the angle of attack for a wing-body combination. Although the leeward-side separation from the body is not taken into account, the computed results are in good agreement with the experimental data.

Figure 20 shows the well-known hysteritic behavior encountered in unsteady flows as the angle of attack increases to a maximum, then decreases to its initial value.

Figure 21 shows the variation of the normal-force and pitching-moment coefficients with time for the delta wing considered in Figure 15. Notice the phase lag between the loads and the wing motion.

THE MODIFIED NONLINEAR-DISCRETE VORTEX (MNDV)-METHOD;LEADING- AND TRAILING-EDGE VORTEX CORES (LEC & TEC)

Figure 22 shows a recent converged solution of the system of free-vortex lines with a long deformed wake. It can be seen that the trace of the trailing-edge vortex system in cross planes indicates that the sheet tends to deform upwards showing a tendency to form a trailing-edge vortex core. However, the cross-flow planes taken further downstream show that the free-vortex lines leapfrog. This does not represent the real flow. Figure 23 shows four of these cross-flow planes taken perpendicular to the wind direction.

It is cleary seen from the example given above, that the existing model of the NDV-method does not realistically model the leading- and trailing-edge vortex cores. Therefore, the model and the numerical technique must be modified in order to obtain realistic vortex-core modeling.

In the MNDV-method a realistic modeling of the primary-vortex core region is introduced. The old NDV-method is only used in the first iterative cycle to initiate the roll-up process and to calculate the centroid of the leading-edge vortex system. Next, the leading- and trailing-edge vortex segments are replaced by smaller segments. Then, the iterative cycles proceed.

In a typical iterative cycle, each free-vortex line of the leading-edge vortex system is allowed, three-dimensionally, to rotate around the most recently calculated centroid a prescribed portion of a turn (1/4, 1/2, 3/4, or 1 turn). This is done by continuously checking the coordinates of the free-vortex segments (as they are adjusted) with the location of the calculated centroid. Once this is achieved, the remaining free-vortex segments of each line are dumped into the calculated centroidal line of the vortex system. The iterative technique is followed until the circulation distribution converges.

Figure 24 shows typical solutions at different iterative cycles. It can be seen , after one iterative cycle, that the system of free-vortex lines shows good roll-up. The converged solution, indicated by ITER=6, shows the leading-edge core and its feeding free-vortex lines. It can also be seen that the free-vortex lines continue to feed the LEC beyond the trailing edge. The trailing-edge core is also indicated on the figure. This will be clearly seen in the cross-flow planes discussed in the next sub-section.

NUMERICAL EXAMPLES-Figures 25-27 show comparisons between the experimental and numerical results for leading- and trailing-edge vortex sheets and flow direction in cross-flow planes perpendicular to the wind direction. The numerical results are drawn at the same scale as that of the experimental results. The predicted sizes and locations of the leading- and trailing-edge vortex sheets are in excellent agreement with the measured ones. The results of the 3/4 turn show the correct roll-up of the trailing-edge vortex sheet and the correct locations of the LEC and TEC. This is exactly what we expected when we increased the roll-up from 1/2 to 3/4 turn. With the 3/4 turn of the leading-edge vortex system, the roll-up tightens and larger velocities are induced at the trailing-edge vortex sheet which cause it to deform upwards and leftwards.

Figure 28 shows comparisons between the predicted and measured static-pressure contours at $\xi = 1.066$. The predicted sizes, locations, and levels of the pressure contours are in good agreement with those of the measured data.

Figure 29 shows comparisons of the predicted and measured spanwise net surface-pressure variation at difference chordwise stations. It is seen that the results of the 3/4 turn are more accurate than that of the 1/2 turn. With 3/4 turn, the roll-up of the leadingedge vortex system tightens and produces better predicted distribution than that of the 1/2 turn.

The developed computer program of the MNDV-method is computationally efficient. On a CYBER-175 machine, a typical solution using a 12x12 lattice and including the cross-flow planes calculation takes 10 minutes of CPU time.

THE NONLINEAR HYBRID-VORTEX (NHV-METHOD)

In this method, vortex panels with first-order vorticity distribution is used in the near-field calculations. In the far field calculations, the distributed vorticity over each far-field panel is lumped into equivalent concentrated vortex lines. In this way, accuracy is satisfied in the near field while computational efficiency is maintained in the far field. The coupling of a continuous vortex-sheet representation and a concentrated vortex-line representation for solving the nonlinear lifting-surface problem is called the "Nonlinear Hybrid-Vortex (NHV)" method.

STEADY-FLOW PROBLEM-Equation (12) requires the flow to be tangent to w while equation (13) requires this tangential flow to be parallel to the vorticity direction. Therefore, if the flow direction is forced to be parallel to the vorticity direction on the surface w, the boundary conditions of equations (12) and (13) are automatically satisfied. Next, we outline the method of solution.

Once the wing and its free-shear layers are represented by vortex sheets, equations (10) and (15) are automatically satisfied. The basic unknowns in the present problem are the vorticity distribution $\bar{\omega}$ and the free-vortex sheet w. They are determined by satisfying the remaining boundary conditions, equations (11)-(14), through a finite-element type approach.

In this approach, the bound-vortex sheet (representing the wing) is divided into quadrilateral bound-vortex panels while the free-vortex sheets (representing the free-shear layers) are divided into triangular free-vortex panels, see Figure 30. On each vortex panel (bound or free), a local vorticity distribution with undetermined coefficients is defined in a local-coordinate system (Figures 31, 32). The local distribution is selected such that the solenoidal property of vorticity is satisfied. The continuity of vorticity (a compatibility condition) is enforced at certain nodes on the interelement boundaries of adjacent panels.

The remaining boundary conditions, equations (11)-(14), are enforced at certain nodes of the vortex panels to obtain the undetermined coefficients of the local vorticity distribution and the shape of the free-vortex panels. Kutta condition, equation (14), is enforced at the nodes of the bound-vortex panels along the edges of separation. The no-penetration condition, equation (11), is enforced at the average points

of the bound-vortex panels. The no-penetration and no-pressure-jump conditions, equations (12) and (13), are simultaneously satisfied at the nodes of the free-vortex panels, Figure 33.

To satisfy these conditions, an iterative technique is followed which alternatively yields the local vorticity distribution on the bound-vortex panels and the shape of the free-vortex panels, Figure 34. During a typical iterative cycle, an overdetermined set of algebraic equations are solved for the undetermined coefficients of the local vorticity distributions. This is followed by adjusting the surface w such that $\bar{\omega}$ and $(\bar{e}_\infty - \nabla\phi)$ at the nodes of the free-vortex panels become parallel. The overdetermined set of equations consists of the equations obtained from the continuity of vorticity condition, Kutta condition, the no-penetration condition on the wing, and a symmetry condition applied at the nodes along the line of symmetry. This set is solved by a least-square technique.

Once the iterative technique converges, the pressure distribution is calculated and this is followed by calculating the total aerodynamic characteristics. Convergence of the technique is expedited by using an initial guess for w provided by NDV-method. More details of the method are given in reference 12.

UNSTEADY-FLOW PROBLEM-The source of flow undsteadiness can be a time dependent angle of attack or a time-dependent freestream speed. In this time-domain approach the function of angle of attack is divided into discrete changes in the angle of attack corresponding to discrete changes in time; i.e., at $t=t_0$, $\alpha=\alpha_0$ and at $t=to + \Delta t$, $\alpha_0+\Delta\alpha$ etc. The problem is then solved at each time step where the solution of each step serves as the initial condition for the next discrete time step. The case of an impulsively started wing from rest is considered for the purpose of explaining the details of the technique. In this case, we set $\alpha=0$ and replace $\bar{e}_\infty$ by $-\bar{e}_\infty$ in equations (16), (17) and (19)-(22). The following steps explain the procedure to enforce the boundary conditions of equations (19)-(22) to obtain $\bar{\omega}(\bar{r},t)$ and $w(\bar{r},t)$:

a. The initial condition, at $t=t_0$, is considered to be a wing without a wake surface having a velocity of $-\bar{e}_\infty$. At this instant, we assume that not enough time has passed for the vorticity to be convected from the separation edges. The initial vorticity distribution on the wing $\bar{\omega}(\bar{r},t)$ is obtained from the least-square solution of an over-determined set of linear algebraic equations in the unknown coefficients describing the vorticity distribution. The set of equations consists of the no-penetration conditions, the continuity of vorticity conditions, the Kutta conditions, and the symmetry conditions.

It should be noted that the initial vorticity distribution on the wing is such that the circulation around any closed curve embracing a wing section or equivalently the outflow of vorticity from a surface enclosed by this curve is zero. Consequently, a starting vortex of opposite strength to that of the vorticity on the wing develops at the edges of separation. Next, the starting vortex is convected downstream with the local particle velocity, the flow existing at the preceding instant is disturbed, and the vorticity distribution on the wing changes creating a new starting vortex to be shed downstream.

This process continues and by the end of the first time-step, at $t=t_0+\Delta t$, a free-vortex strip, consisting of triangular free-vortex panels attached to the separation edges, is created. The free-vortex strip obeys the conditions given by equations (20) and (21) and its upstream edge satisfies Kutta condition at the separation edges, equation (22).

b. At $t=t_0+\Delta t$, one needs $\bar{v}(\bar{r},t_0+\Delta t)$ to determine the width of the vortex strip. Since this velocity is unknown so far, a good estimate is taken as the velocity at the preceding time step $\bar{v}(\bar{r},t_0)$, which is completely known from the solution corresponding to the initial condition. Within the time step Δt, the displacement $\Delta\bar{r}$ of any panel node is found from

$$\Delta\bar{r} = \bar{r}(t_0 + \Delta t) - \bar{r}(t_0) = \Delta t \cdot \bar{V}(\bar{r},t_0) \qquad (32)$$

Equation (22) is the same as equation (28) of the NDV-method.

At $t=t_0+\Delta t$, one also needs the vorticity of the triangular vortex panels forming the free-vortex strip, $\bar{\omega}_w(\bar{r},t_0+\Delta t)$. For each triangular panel, we express its five unknown coefficients, describing its linear vorticity distribution, in terms of the five unknown coefficients of the adjacent bound-vortex panel, at the separation edges, at $t=t_0$ (the coefficients of the bound panel are already known) and at $t=t_0+\Delta t$ (the coefficients of the bound panel are still unknown). This is achieved by satisfying the following conditions. At $t=t_0+\Delta t$ the vorticity is continuous at the global nodes (on the separation edge) between the bound- and free-vortex panels. Also, at $t=t_0+\Delta t$, the fluid particles along the downstream edges of the triangular panels are the same particles which existed at the edge of separation at $t=t_0$. According to Helmholtz theorem $[D\bar{\omega}/Dt = (\bar{\omega}\cdot\nabla)\bar{v}]$, the vorticity of these particles changes as they are convected downstream. But according to Kelvin theorem $(D\Gamma/Dt = 0)$, the circulation around these particles remains constant and hence additional equations are written to satisfy Kelvin theorem between $t=t_0$ and $t=t_0+\Delta t$.

Next, the vorticity distribution on the wing $\bar{\omega}(\bar{r},t_0+\Delta t)$ is obtained from the overdetermined set of algebraic equations.

c. At $t=t_0+2\Delta t$, a new free-vortex strip is created along the separation edges, the first shed free-vortex strip is convected downstream under the condition $D\Gamma/Dt = 0$, and step (b) is repeated to find locations of the free-panels nodes and $\bar{\omega}(\bar{r},t_0+2\Delta t)$.

d. The steady state is reached once the change in the vorticity distribution is less than a prescribed error.

To calculate the net pressure coefficient at any point on the wing surface $\bar{r}$ at any time $t_k = t_0 + t_k \cdot \Delta t$, we apply the unsteady Bernoulli's equation

$$\Delta C_p(\bar{r},t_k) = -2\bar{V}_j(\bar{r},t_k) \cdot [\nabla\phi(\bar{r},t_k) + (\bar{e}_\infty + \dot{\alpha}\bar{k}x\bar{r})] - 2\frac{\partial\Delta\phi(\bar{r},t_k)}{\partial t} \qquad (33)$$

where $\bar{V}_j(\bar{r},t_k)$ is the jump in the tangential velocity across the wing, which is completely known from the vorticity vector at this location, $\bar{\omega}(\bar{r},t_k)$.

NUMERICAL EXAMPLE FOR A STEADY-FLOW-The developed computer program of Figure 34 is used to solve for the steady flow past a rectangular wing having side-edge separation. The wing is of aspect ratio of one at 9.7° angle of attack. The wing is divided into 6x6 quadrilateral bound-vortex panels, the trailing edge free-vortex sheet is divided into 6x6 quadrilateral free-vortex panels, and the side edge free-vortex sheet is divided into a 6 vortex strips and each is divided into a different number of quadrilateral free-vortex panels such that the last panel in each strip occupy the same chordwise station as that of the last panel

of the trailing-edge free-vortex panel.

Figure 35 shows a typical converged solution of the spanwise and chordwise components of vorticity at the local nodes of the quadrilateral vortex panels. At any node, the upper number is the spanwise component ω_ζ and the lower number is the chordwise component ω_ξ. It is seen that the continuity of vorticity condition, Kutta condition and the symmetry condition are satisfied at the common nodes, at the nodes of the trailing and side edges, and at the notes of the line of symmetry; respectively.

Figure 36 shows the spanwise variation of the section normal-force coefficient at three iteration steps. The solution converges in the third iteration step and is in good agreement with the experimental data of Scholtz[24]. The figure also shows the solution of the same case obtained by the NDV-method with 6x6 bound-vortex lines. One can conclude that the NDV-method underestimates the normal-force coefficient near the wing tip. If the number of bound-vortex lines of the NDV-method is increased to 9x7 (Figure 16), the solution agrees with that obtained by the NHV-method with 6x6 bound-vortex panels. This clearly shows that a less number of vortex panels gives the same accuracy as that obtained by a large number of bound-vortex lines.

Figure 37 shows the converged solution of the spanwise variation of the section pitching-moment coefficient for the wing. The results of the NDV-method with 6x6 and 9x7 bound-vortex lines are also included in the figure.

Figure 38 shows the spanwise variation of the net-pressure coefficient at different chord stations with different number of panels for a rectangular wing at 15° angle of attack. The corresponding results of the NDV-method are also shown in the figure.

The present computer program is computationally efficient when it is compared with other existing codes which use high-order doublet distribution. The CPU time on the CYBER 175 for this case is about 200 seconds.

NUMERICAL EXAMPLE FOR AN UNSTEADY FLOW-The same computer program is also used to solve for the unsteady flow past impulsively strated wings from rest without side edge separation. In the two examples, the wing is divided into 5x5 quadrilateral bound-vortex panels with a sine distribution in the chordwise direction and a cosine distribution in the spanwise direction. In the present cases, the dimensionless time step is equivalent to 0.48 while the root-chord length is 5 units.

Figure 39 shows the distribution of the lift coefficient for a rectangular wing of aspect ratio of three at 5° angle of attack for t=2 and t=22. The present results are compared with the steady numerical data of reference (83) where 196 panels of constant potential function are used. It is also compared with the experimental data of Reference (82). Although we used 25 panels in the present case, the results compares well with the given data.

Figure 40 compares the growth of indicial lift for the same wing considered above with the numerical data of reference (84) where 100 panels of constant doublets are used.

Figure 41 shows the distribution of net pressure coefficient for a rectangular wing of aspect ratio of two at 20.5° angle of attack for t=2, 10, 21 and 22.

On the CYBER 175 computer, the CPU time for each case with 5x5

bound panels and 22 time steps is about 10 minutes.

Currently, work is underway to increase the number of panels, use the efficient far field calculations, and calculate cases with side- and leading-edge separations.

CONCLUDING REMARKS

Steady and unsteady, incompressible free-wake analysis has been presented in detail. In the first part of the lecture, the motive behind the problem is established. Some of the existing experimental measurements and data are discussed and the approximations for the mathematical model are deduced. Using the model, the general formulation of the problem and special steady and unsteady cases are developed. The existing methods of solution are divided into four main groups; slender-body methods, nonlinear vortex lattice methods, doublet-panel methods, and nonlinear vortex-panel methods.

Two specific methods (one from the second group; the NDV-method and the other from the fourth group; the NHV-method) are presented in detail with numerical examples showing their capabilities and success. I would like to emphasize that the nonlinear discrete-vortex method should not be abandoned in view of the success of the MNDV-method. It is simple, accurate, and efficient. For more accuracy, all we need is to replace the near-field calculations by continuous vortex panels instead of the vortex lines.

The solution of the free-wake problem is far from being complete. The problem of compressibility effects in high subsonic and transonic flow needs considerable efforts in the future. In the transonic regime, the problems of shock capturing and shock-free wake interaction will require careful analysis and bigger computing machines. Currently, several researchers are approaching the present problem using the finite difference method. It remains to be seen how successful this approach is.

ACKNOWLEDGEMENT

The research work, reported in this lecture, to develop the Nonlinear Discrete- and Hybrid-Vortex Methods has been supported for several years, under different grants from NASA-Langley Research Center at Hampton, Virginia (Dr. E. Carson Yates, Jr. - technical montior), the Army Research Office at Research Triangle, North Carolina (Dr. Robert Singleton - technical monitor) and the Naval Air-Development Center at Warminster, Pennsylvania (Mr. Marvin Walters - technical monitor).

REFERENCES

1. A. M. Skow and G. E. Erickson, "Modern Fighter Aircraft Design for High-Angle-cf-Attack Aerodynamics." AGARD Lecture Series No. 121 High-Angle-of-Attack Aerodynamics, NASA Langley Research Center, Hampton, Va., March 1982.

2. J. N. Nielson, "Nonlinearities in Missile Aerodynamics." AIAA Paper No. 78-20, January 1978.

3. N. A. Chigier and V. R. Corsiglia, "Tip Vortices-Velocity Distributions." Preprint No. 522, Presented at the 27th Annual National V/STOL Forum of the American Helicopter Society, Washington, D.C., May 1971.

4. D. Hummel, "On Vortex Formation Over Slender Wings at Large Angles of Incidence." AGARD CP-247, January 1979, pp. 15.1-15.17.

5. R. B. Gray, "An Aerodynamic Analysis of a Single-Bladed Rotor in Hovering and Low Speed Forward Flight as Determined from Smoke Studies of the Vorticity Distribution in the Wake." Princeton University Aeronautical Engineering Report No. 356, Princeton, New Jersey, September 1956.

6. W. L. Oberkamf and T. J. Bartel, "Supersonic Flow Measurements in the Body Vortex Wake of an Ogive Nose Cylinder." AIAA Paper No. 78-787, April 1978.

7. L. C. Squire, "Flow Regimes Over Delta Wings at Supersonic and Hypersonic Speeds." Aeronautical Quarterly, Vol. XXVII, Part 1, February 1976, pp. 1-14.

8. A. N. Minailos, "Calculation of Supersonic Flow Past Wings with Consideration of Tangential Discontinuites Shed from the Edges within the Scope of a Model Using a System of Euler Equations." Fluid Dynamics, Vol. 13, No. 1, January-February, 1978.

9. G. H. Klopfer and J. N. Nielsen, "Euler Solutions for Wing and Wing-Body Combinations at Supersonic Speeds with Leading-Edge Separation." AIAA Paper No. 80-0126, January 1980.

10. O. A. Kandil, "Prediction of Steady Aerodynamic Loads on Lifting Surfaces Having Sharp-Edge Separation." Ph.D. Dissertation, Virginia Polytechnic Institute and State University, Blacksburg, Va., December 1974, pp. 57-64.

11. M. Hafex, J. South and E. Murman, "Artificial Compressibility Method for Numerical Solutions of Transonic Full Potential Equation." AIAA Journal, Vol. 17, No. 8, August 1979, pp. 838-844.

12. O. A. Kandil, L-C. Chu, T. Tureaud, "Steady and Unsteady Nonlinear Hybrid Vortex Method for Lifting Surfaces at Large Angles of Attack." AIAA Paper No. 82-351, January 1982.

13. O. A. Kandil and L. Balakrishnan, "Recent Improvements in the Prediction of the Leading- and Trailing-Edge Vortex Cores of Delta Wings." AIAA Paper No. 81-1263, June 1981.

14. L. Chu, "Nonlinear Hybrid-Vortex Method for Wings Having Side-Edge Separations." M.S. thesis, Old Dominion University, Norfolk, Va., December 1980.

15. O. A. Kandil, "Numerical Prediction of Vortex Cores from the Leading and Trailing Edges of Delta Wings." ICAS Paper No. 14.2, the 12th Congress of the International Council of Aeronautical Sciences, Munich, West Germany, October 12-17, 1980.

16. O. A. Kandil, L-C. Chu and E. C. Yates, Jr., "A Hybrid Vortex Method for Lifting Surfaces with Free-Vortex Flows." AIAA Paper No. 80-70, January 1980.

17. E. H. Atta, "Unsteady Aerodynamics of Wings and Wing-Body Configurations at High Angles of Attack." Ph.D. Dissertation, Virginia Polytechnic Institute and State University, Blacksburg, Va., May 1978.

18. O. A. Kandil, E. H. Atta and A. H. Nayfeh, "Three-Dimensional Steady and Unsteady Asymmetric Flow Past Wings of Arbitrary Planforms," AGARD CP-227, Unsteady Aerodynamics, 1978, pp. 2.1-2.19.

19. E. H. Atta, O. A. Kandil, D. T. Mook and A. H. Nayfeh, "Nonlinear, Unsteady Aerodynamic Loads on Rectangular and Delta Wings." AIAA Paper No. 77-157, January 1977.

20. O. A. Kandil, D. T. Mook and A. H. Nayfeh, "A Numerical Technique for Computing Subsonic Flow Past Three-Dimensional Canard-Wing Configuration with Edge Separation." AIAA Paper No. 77-1, January 1977.

21. O. A. Kandil, D. T. Mook and A. H. Nayfeh, "Subsonic Loads on Wings Having Sharp Leading-Edges and Tips." Journal of Aircraft, Vol. 13, No. 1, January 1976, pp. 62-63.

22. O. A. Kandil, D. T. Mook and A. H. Nayfeh, "Nonlinear Prediction of Aerodynamic Loads on Lifting Surfaces." Journal of Aircraft, Vol. 13, No. 1, January 1976, pp. 22-28.

23. H. Winter, "Flow Phenomena on Plates and Airfoils of Short Span." NACA Report 798, 1936.

24. V. N. Scholz, "Kraft and Drickverteilungsmessungen an Tragflachen Kleiner Streckung." Forscharb. Ing. Wes., 16, 1949, pp. 85-92.

25. H. A. Wilson, Jr. and J. C. Lovell, "Full Scale Investigation of the Maximum Lift and Flow Characteristics of an Airplane having Approximately Triangular Planform." NACA RM No. LGK 20, 1947.

26. G. E. Bartlett and R. J. Vidal, "Experimental Investigation of Influence of Edge Shape on the Aerodynamic Characteristics of Low-Aspect-Ratio Wings at Low Speeds." Journal of Aeronautical Sciences, Vol. 22, No. 8, August 1955, pp. 517-533.

27. D. J. Marsdon, R. W. Simpson and B. E. Rainbird, "An Investigation into the Flow Over Delta Wings at Low Speeds with Leading Edge Separation." The College of Aeronautics, Cranfield, Report No. 114, February 1958.

28. D. H. Peckham, "Low-Speed Wing-Tunnel Tests on a Series of Uncambered Slender Pointed Wings with Sharp Edges." RAE Report No. AERO 2613, ARC R and M 3186, December 1958.

29. N. C. Lambourne, and D. W. Bryer, "Some Measurements in the Vortex Flow Generated by a Sharp Leading Edge Having 65° Sweep." ARC 21, 073, July 1959.

30. A. J. Bergesen and J. D. Porter, "An Investigation of the Flow Around Slender Delta Wings with Leading-Edge Separation." Princeton University, Department of Aeronautical Engineering, RPT. No. 510, May 1960.

31. P. B. Earnshaw, "An Experimental Investigation of the Structure of a Leading-Edge Vortex." RAE Technical Note No. Aero. 2740, R and M. No. 3281, March 1961.

32. W. H. Wentz, "Effects of Leading-Edge Camber on Low-Speed Characteristics of Slender Delta Wings." NASA CR-2002, 1972.

33. D. Hummel, "Study of Flow Around Sharp-Edged Slender Delta Wings with Large Angles of Attack." NASA TT F-15, 107, September 1973.

34. D. Hummel and G. Redker, "Experimentelle Bestimmung der Gebuden Wirbellinien Sowie des Stromungsverlaufs in der Umgebung der Hinter-Kante eines Schlanken Delta Flugels." Abhandlg. d. Braunschw. Wiss. Ges, 22, 1972, pp. 273-290.

35. N. C. Lambourne and D. W. Bryer, "The Bursting of Leading Edge Vortices; Some Observations and Discussion of the Phenomenon." ARC, R & M 3282, 1962.

36. M. V. Lowson, "Some Experiments with Vortex Breakdown." Journal of the Royal Aeronautical Society, Vol. 68, 1964, pp. 343-346.

37. D. H. Peckham and S. A. Atkinson, "Preliminary Results of Low Speed Wind Tunnel Tests on a Gothic Wing of Aspect Ratio 1." ARC, CP 508, 1957.

38. D. Hummel and P. S. Srinivasan, "Vortex Breakdown Effects on the Low-Speed Aerodynamic Characteristics of Slender Delta Wings in Symmetrical Flow." Journal of the Royal Aeronautical Society, Vol. 71, April 1967, pp. 319-322.

39. H. J. Allen and E. W. Perkins, "A Study of Effects of Viscosity on Flow over Slender Inclined Bodies of Revolution." NACA Report 1048, 1951.

40. R. L. Maltby and D. H. Peckham, "Low Speed Flow Studies of the Vortex Patterns above Inclined Slender Bodies Using a New Smoke Technique." RAE TN 2482, Nov. 1956, ARC Great Britain.

41. W. J. Rainbird, R. S. Crabbe and L. S. Jurewicz, "A Water Tunnel Investigation of the Flow Separation About Circular Cones at Incidence." Aero Report LR-385, Sept. 1963, National Research Council of Canada, Ottawa, Canada.

42. E. G. Friberg, "Measurement of Vortex Separation: Part II-Three-Dimensional Circular and Elliptic Bodies." TR 115, Aug. 1965. MIT Aerophysics Lab., Cambridge, Mass.

43. W. J. Rainbird, R. S. Crabbe, D. J. Peake and R. R. Heyer, "Some Examples of Separation in Three-Dimensional Flows." Canadian Aeronautics and Space Journal, Vol. 12, No. 10, Dec. 1966, pp. 402-423.

44. L. H. Schindel and T. E. Chamberlain, "Vortex Separation on Slender Bodies of Elliptic Cross Section." TR 138, Aug. 1967, MIT Aerophysics Lab., Cambridge, Mass.

45. G. S. Pick, "Investigation of Side Forces on Ogive-Cylinder Bodies at High Angles of Attack in the M=0.5 to 1.1 Range." AIAA Paper No. 71-570, June 1971.

46. K. D. Thomson and D. F. Morrison, "The Spacing, Position and Strength of Vortices in the Wake of Slender Cylindrical Bodies at Large Incidence." Journal of Fluid Mechanics, Vol. 50, part 4, 1971, pp. 751-783.

47. F. D. Deffenbaugh and W. G. Loerner, "Asymmetric Wake Development and Associated Side Force on Missiles at High Angles of Attack." AIAA Paper No. 76-364, July 1974.

48. J. E. Fidler, R. G. Schwind and J. N. Nielsen, "An Investigation on Slender-Body Wake Vortices." NEAR TR 108, April 1976.

49. W. J. Yanta and A. B. Wardlaw, "Laser Doppler Velocimeter Measurements of Leeward Flow Fields on Slender Bodies at Large Angles of Attack." AIAA Paper 77-660, June 1977.

50. B. L. Hunt and P. C. Dexter, "Pressures on a Slender Body at High Angles of Attack in a Very Low Turbulence Level Airstream." AGARD-CP-247, January 1979.

51. E. R. Keener and G. T. Chapman, "Similarity in Vortex Asymmetrics Over Slender Bodies and Wings." AIAA Journal, Vol. 15, No. 9, September 1977, pp. 1370-1372.

52. L. E. Ericsson and J. P. Reding, "Vortex-Induced Asymmetric Loads in 2-D and 3-D Flows." AIAA Paper No. 80-0181, January 1980.

53. M. R. Mendenhall, S. B. Spangler and S. C. Perkins, Jr., "Vortex Shedding from Circular and Non-Circular Bodies at High Angles of Attack." AIAA Paper No. 79-26, January 1979.

54. R. Legendre, "E'coulement du Vaisinage de la Pointe Avante d'une dile a Forte Flache dux Incidences Moyenes." La Recherche Aeronautique No. 31, 1953.

55. C. E. Brown and W. H. Michael, "Effect of Leading Edge Separation on the Lift of a Delta Wing." Journal of Aeronautical Sciences, Vol. 31, Oct. 1954, pp. 690-694.

56. K. W. Mangler and J. H. B. Smith, "Calculation of the Flow Past Slender Delta Wings with Leading Separation." RAE Report 2593, May 1957, Royal Aircraft Establishment, Farnsborough, England.

57. K. Gersten, "Calculation of Nonlinear Aerodynamic Stability Derivatives of Aeroplanes." AGARD Report 342, April 1961.

58. H. C. Garner and Lehrian, "Nonlinear Theory of Steady Forces on Wings with Leading-Edge Flow Separation." R & M 3375, Feb. 1963, Aeronautical Research Council, London.

59. D. K. Pullin, "Calculations of the Steady Conical Flow Past a Yawed Slender Delta Wing with Leading Edge Separation." Imperial College of Science and Technology, Lond., I. C. Aero Report 72-17, July 1972.

60. I. P. Jones, "Flow Separations from Yawed Delta Wings." Computers and Fluids, Vol. 3, 1975, pp. 155-177.

61. M. J. Cohen and D. Nimri, "Aerodynamics of Slender Rollings Wings at Incidence in Separated Flow." AIAA Journal, Vol. 14, No. 7, July 1976, pp. 886-893.

62. S. M. Belotserkovskii, "Calculation of the Flow Around Wings of Arbitrary Planfors Over a Wide Range of Angles of Attack." NASA TT F-12, 391, 1969.

63. C. Rehbach, "Calculation of Flow Around Zero-Thickness Wings with Evolute Vortex Sheets." NASA TT F-15, 183, 1973.

64. C. Rehbach, "Numerical Investigation of Vortex Sheets Issuing from Separation Line Near the Leading Edge." NASA TT F-15, 530, 1974.

65. S. M. Belotserkovskii and M. I. Nisht, "Non Stationary Nonlinear Theory of a Thin Wing of Arbitrary Planform." Mekhanika Zhidkosti Gasa, No. 4, 1974, pp. 100-108.

66. J. Rom, D. Almosnino and C. Zorea, "Calculation of the Nonlinear Aerodynamic Coefficients of Wings of Various Shapes and Their Wakes Including Canard Configurations." 11th Congress of ICAS, Lisbon, Portugal, September 1978.

67. S. G. Hedman, "Vortex-Lattice Method for Calculation of Quasi Steady State Loadings on Thin Elastic Wings." The Royal Aeronautical Institute of Sweden, Report 105, Stockholm, 1966.

68. F. T. Johnson, E. N. Tinoco, P. Lu and M. A. Epton, "Recent Advances in the Solution of Three-Dimensional Flows Over Wings with Leading Edge Vortex Separation." AIAA Paper No. 79-0282, January 1979.

69. J. F. Campbell, "Vortex Flow Aerodynamics-An Emerging Design Capability." Astronautics & Aeronautics, Volume 19, No. 5, May 1981, pp. 54, 54, 58.

70. F. T. Johnson and P. E. Rubbert, "Advanced Panel-Type Influence Coefficient Methods Applied to Subsonic Flows." AIAA Paper No. 75-50, January 1975.

71. J. A. Weber, G. W. Brune, F. T. Johnson, P. Lu and P. E. Rubbert, "Three Dimensional Solution of Flows Over Wings with Leading Edge Vortex Separation." AIAA Journal, Vol. 14, 1976, pp. 519-525.

72. F. T. Johnson, P. Lu, G. W. Brune, J. A. Weber and P. E. Rubbert, "An Improved Method for the Prediction of Completely Three-Dimensional Aerodynamic Load Distributions on Configurations with Leading-Edge Separation." AIAA Paper 76-417, 1976.

73. J. M. Kuhlman, "Analytical Studies of Separated Vortex Flow on Highly Swept Wings." NASA CR 3022, Nov. 1978.

74. C. S. Reddy, "Theoretical Study of Aerodynamic Characteristics of Wings Having Vortex Flow." NASA CR 159184, Nov. 1979.

75. H. W. M. Hoeijmakers and B. Bennekers, "A Computational Method for the Calculation of the Flow about Wings with Leading-Edge Vortices." AGARD CP-247, January 1979.

76. K. Karamcheti, "Principles of Ideal-Fluid Aerodynamics." John Wiley and Sons, Inc., N.Y., 1966.

77. P. M. Yager, C. H. Holland and T. Strand, "Modified Weissinger Lifting Surface Method for Calculating Aerodynamic Parameters of Arbitrary Wing-Canard Configurations." Air Vehicle Corporation, La Jolla, California, Rept. 354, August 1974.

78. J. K. Harvey, "Some Measurements on a Yawed Slender Delta Wing with Leading Edge Separation." British ARC Report 20451, 1958.

79. J. K. Karvey, "A Study of the Flow Field Associated with Steadily-Rolling Slender Delta Wing." Journal of the Royal Aeronautical Society, Vol. 68, Feb. 1964, pp. 106-110.

80. M. Hanin and D. Lischne, "Flow About Rolling Slender Wing with Leading Edge Separation." Israel Journal of Technology, Vol. 11, No. 13, 1973, pp. 131-136.

81. C. F. Hall, "Lift, Drag and Pitching Moment of Low-Aspect-Ratio Wings at Subsonic and Supersonic Speeds." NASA RM A53A30.

82. H. C. Lessing, J. C. Troutman and G. P. Menees, "Experimental Determination of the Pressure Distribution on a Rectangular Wing Oscillating in the First Bending Mode for Mach numbers from 0.24 to 1.30." NASA TN D-344, 1960.

83. L. Morino and K. Tseng, "Time-Domain Green's Function Method for Three-Dimensional Nonlinear Subsonic Flows." AIAA Paper No. 78-1204, 1978.

84. J. M. Summa, "A Numerical Method for the Exact Calculation of Airloads Associated with Impulsively Started Wings." AIAA Paper 77-002, 1977.

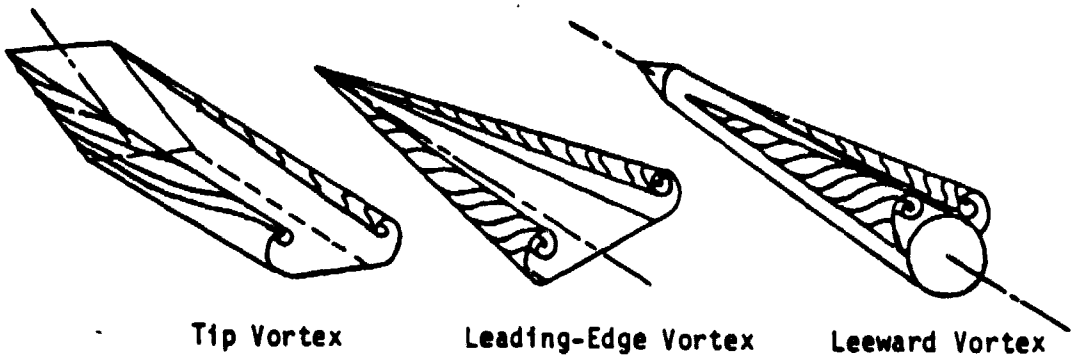

Tip Vortex Leading-Edge Vortex Leeward Vortex

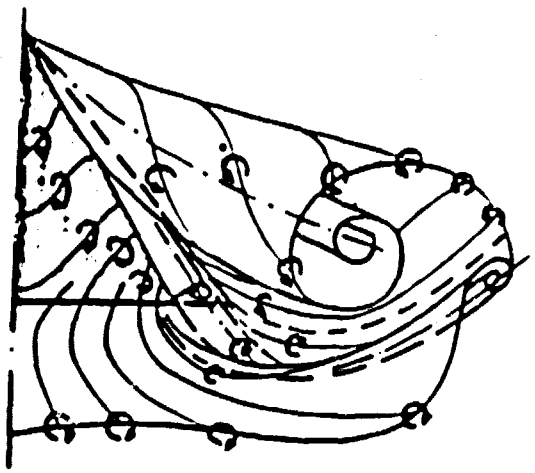

Leading- and Trailing-Edge Vortex Interaction (Reference 4)

a. Vortex Flows of Isolated Wings and Bodies

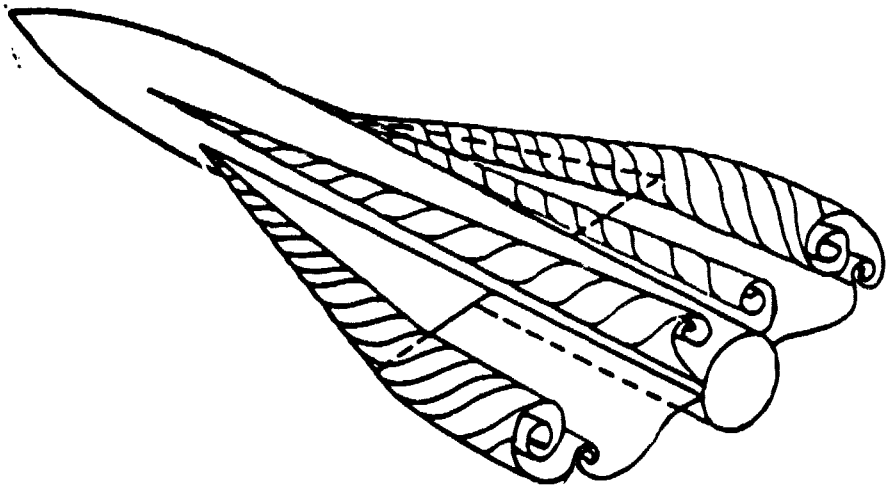

b. Symmetric Vortex Flow of a Wing-Body Configuration

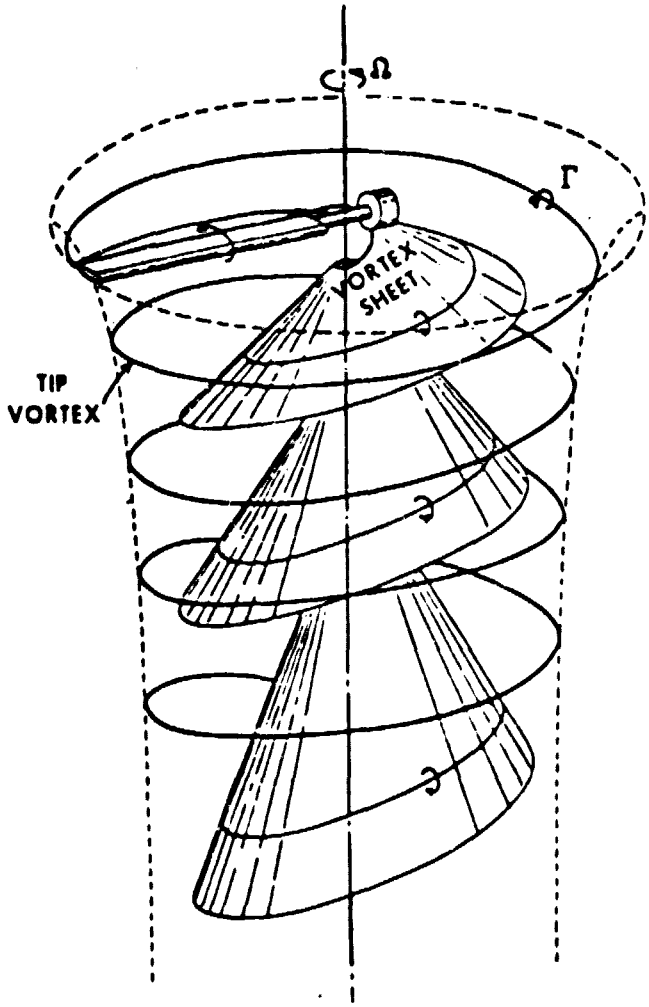

c. Vortex Flow of a Hovering Rotor (Reference 5)

Figure 1. Examples of Vortex Flows

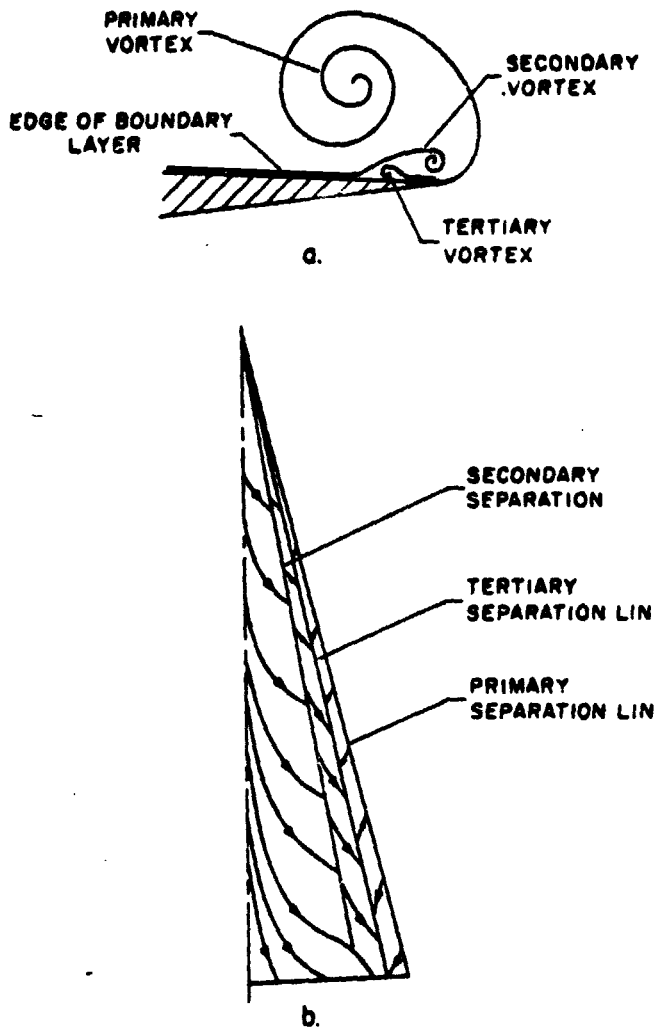

a. Section normal to the leading edge
b. Separation lines

Figure 2. Types of separation near the leading edge of highly swept back wings.

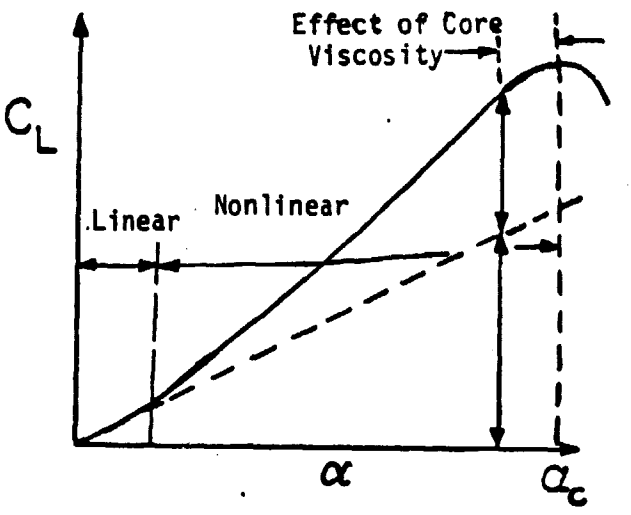

Figure 3. Lift Coefficient VZ angle of attack for highly swept back wings.

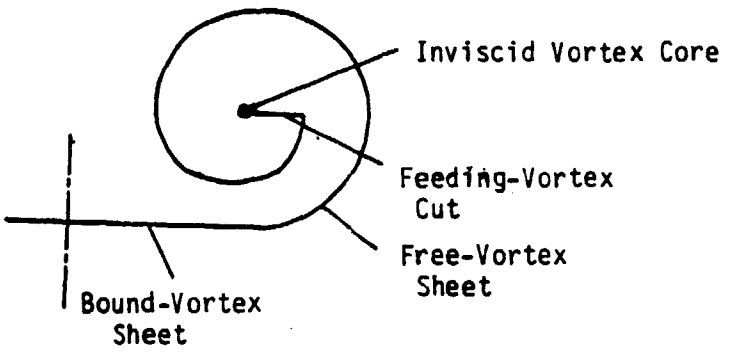

Figure 4. Inviscid model of primary separation

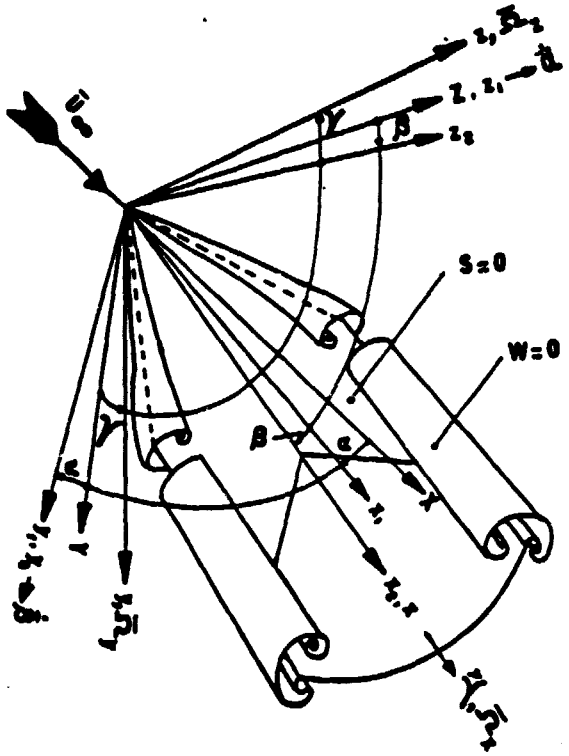

Figure 5. Space-Fixed Coordinates XYZ, Wing-Fixed Coordinates xyz, and Eulerian's Angles α, β, γ.

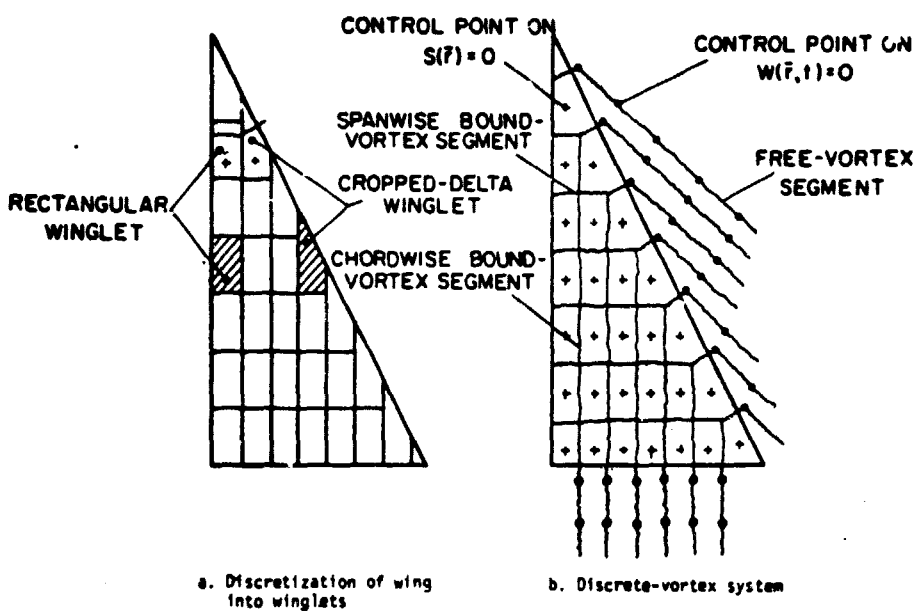

Figure 6. Construction of the discrete-vortex system in the NDV-method.

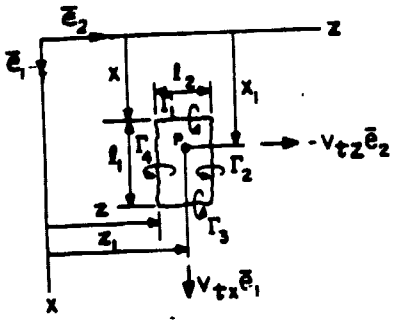

Figure 7. Self-induced tangential velocity in the NDV-method.

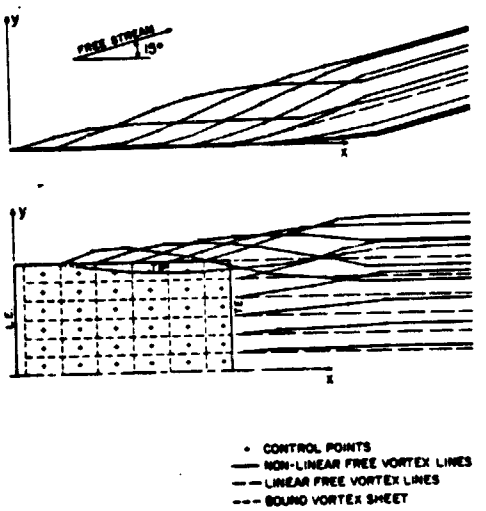

Figure 8. Typical solution of the side-edge vortex sheet, steady flow, AR=1, α=15°, 6x6 lattice, NDV-method.

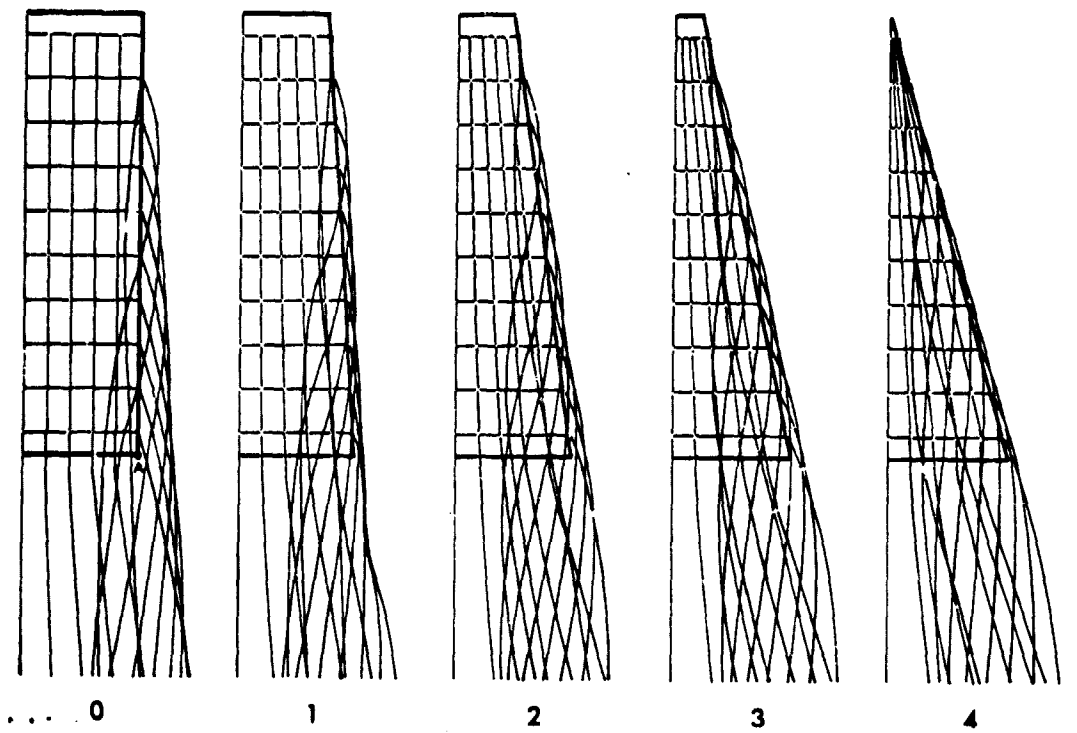

Figure 9. Rehbach's[64] progressive deformation of rectangular wing.

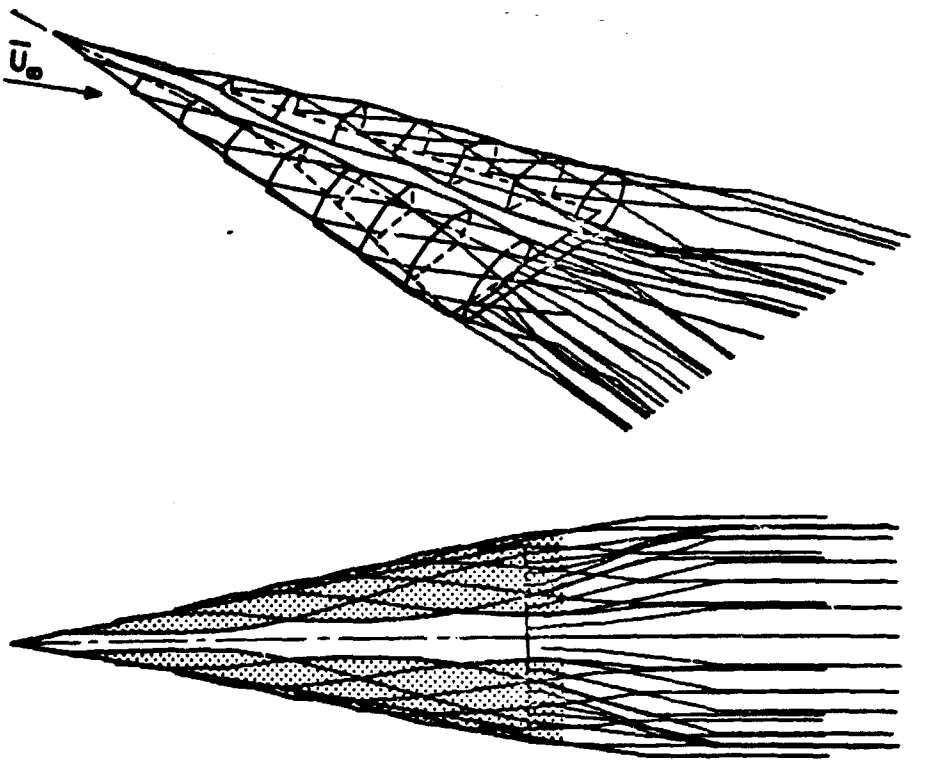

Figure 10. Typical solution of the leading-edge vortex sheet, steady flow, AR=0.7, α=15°, 8x8 lattice, NDV-method.

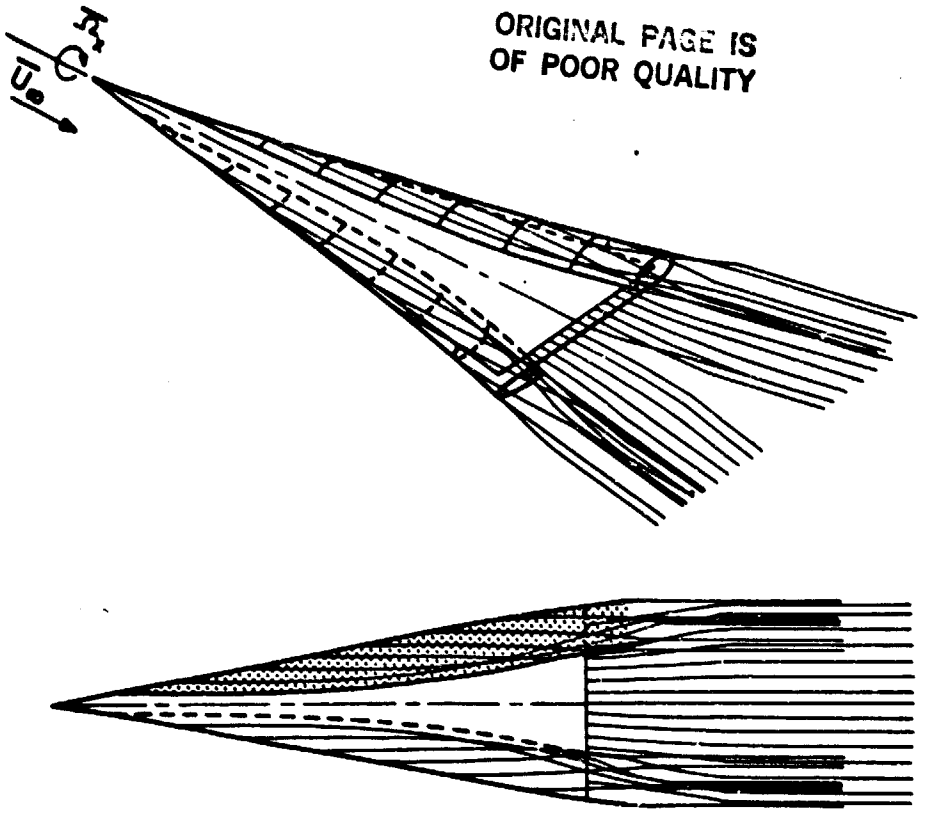

Figure 11. Typical solution of the leading-edge vortex sheet, steady rolling motion, AR=0.7, α=0°, Ω_x=-0.2, 8x8 lattice, NDV-method.

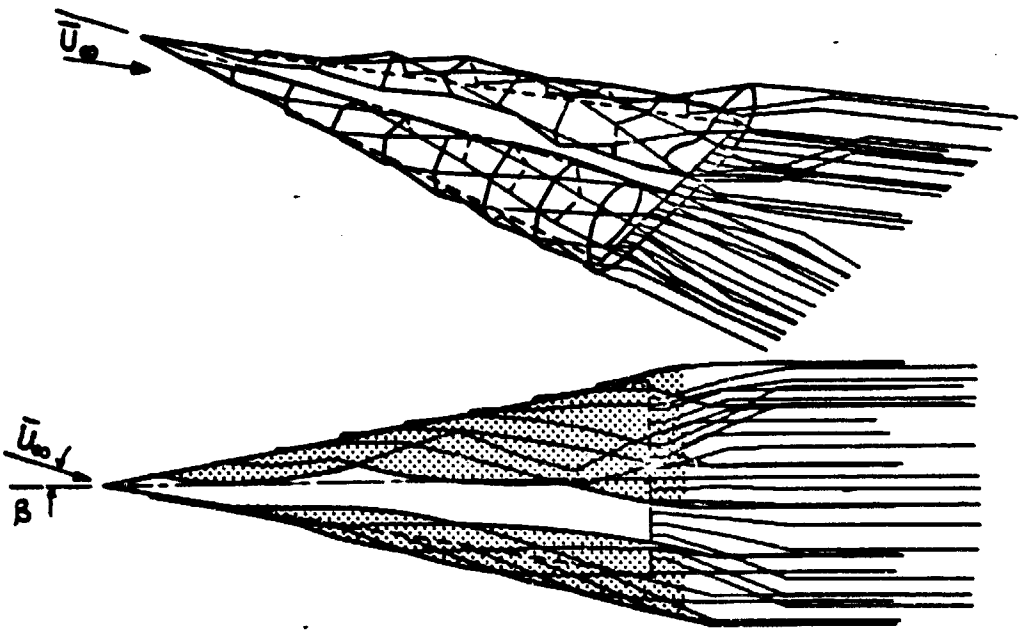

Figure 12. Typical solution of the leading-edge vortex sheet, Yawed wing, AR=0.7, α=15°, β=10°, 8x8 lattice, NDV-method.

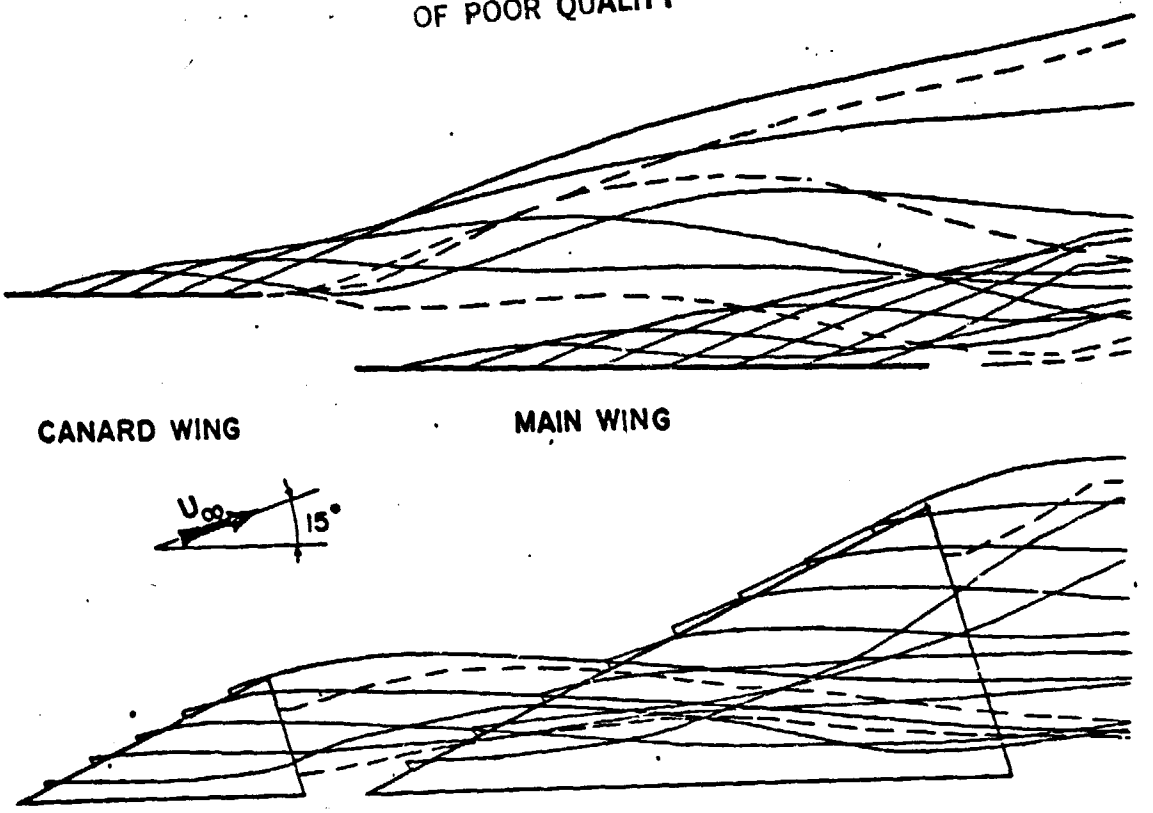

Figure 13. Typical solution of the free-vortex sheets for a canard-wing configuration, steady flow, AR=1.66, α=15°, 5x5 and 8x8 lattices for the canard and main wing; respectively, NDV-method.

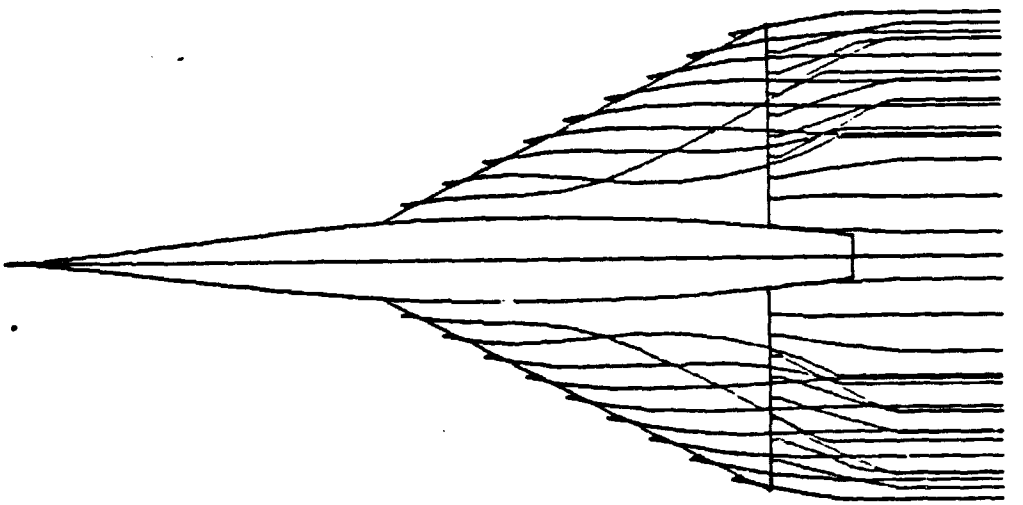

Figure 14. Typical solution of the leading-edge vortex sheet for a wing-body combination (no leeward separation), AR=2, f=9.86, α=12.15°, 9x9 lattice for wing, 25x16 lattice for the body.

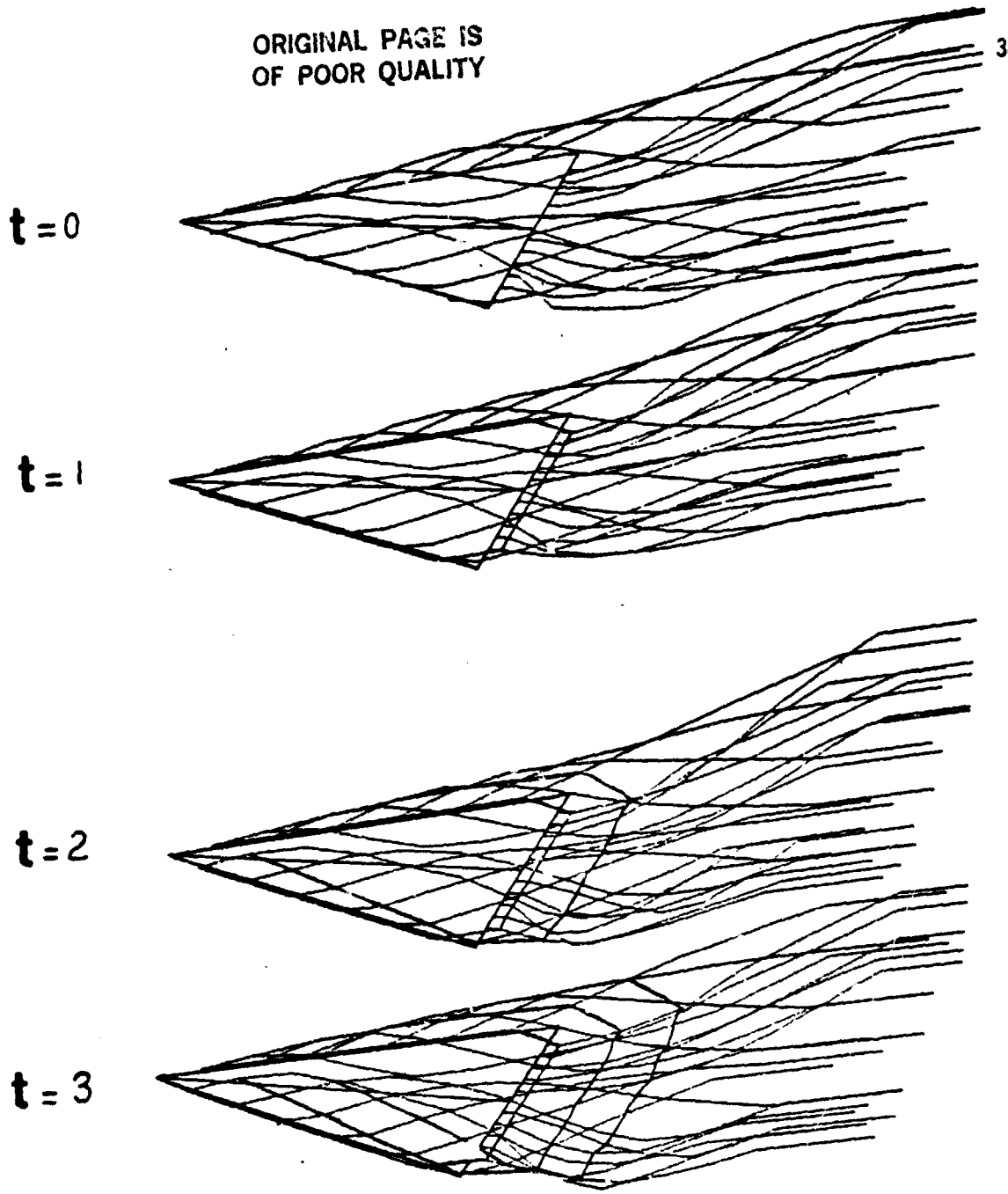

Figure 15. Typical solution of the unsteady wake for a delta wing, AR=1, $\alpha=15°+4 \sin \frac{\pi}{6} t$, 6x6 lattice, NDV-method.

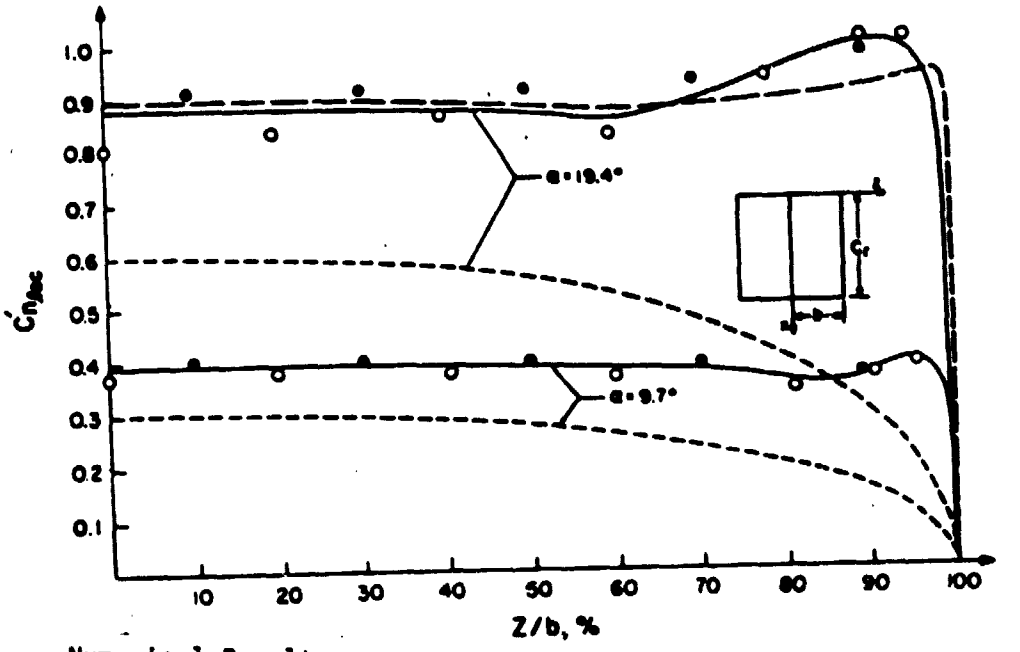

Numerical Results

—— — Gersten[57]
● Rehbach[63]

----- Linear
——— Nonlinear } NDV-Method (9 x 7 lattice)

Experimental Results

o Scholz[24]

Figure 16. Spanwise variation of section normal-force coefficient, AR=1.

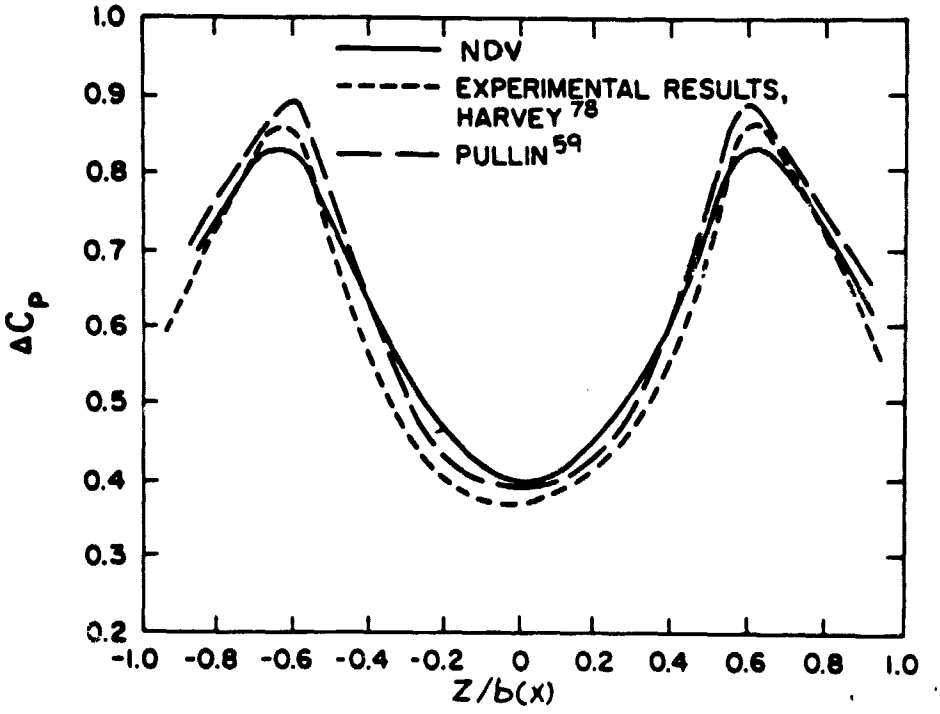

Figure 17. Net spanwise pressure distribution on a delta wing, AR=0.7, α=15°, 8x8 lattice, x/c_r=0.395.

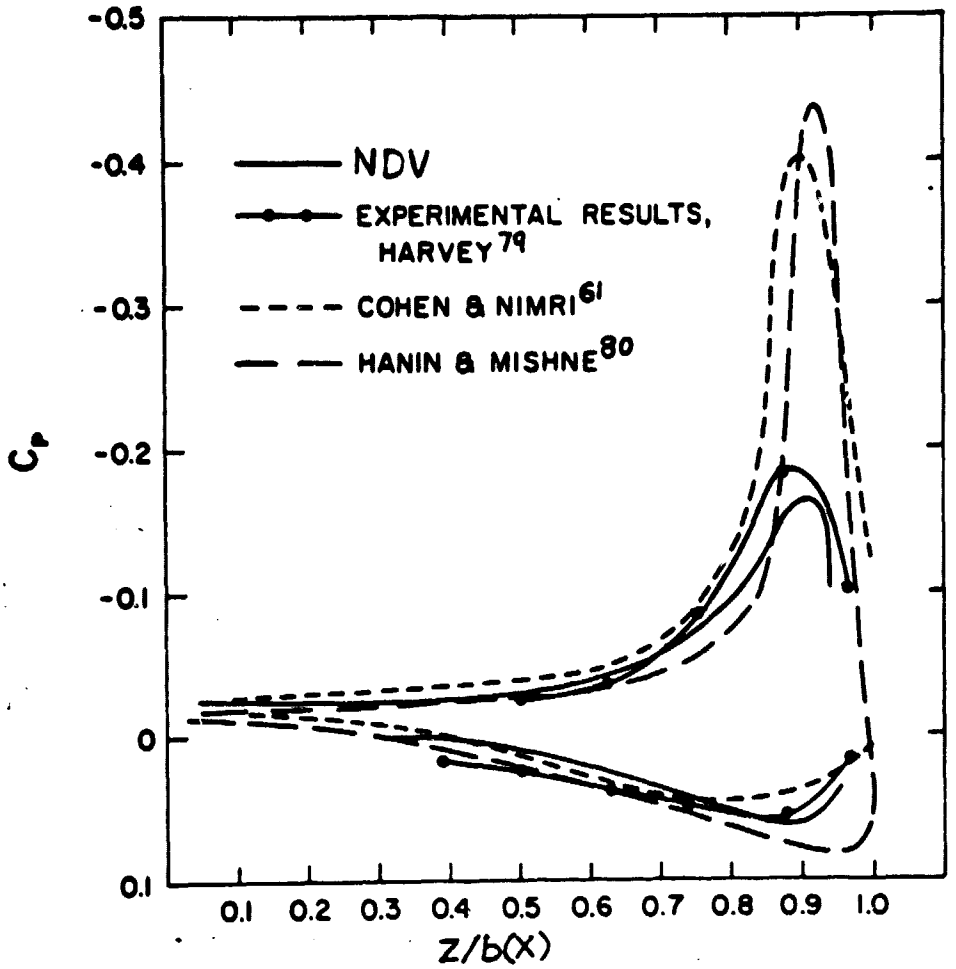

Figure 18. Upper and lower, spanwise pressure variation on a steadily rolling delta wing, AR=0.7, α=0°, Ω_x=-0.2, 8x8 lattice, x/c_r=0.778.

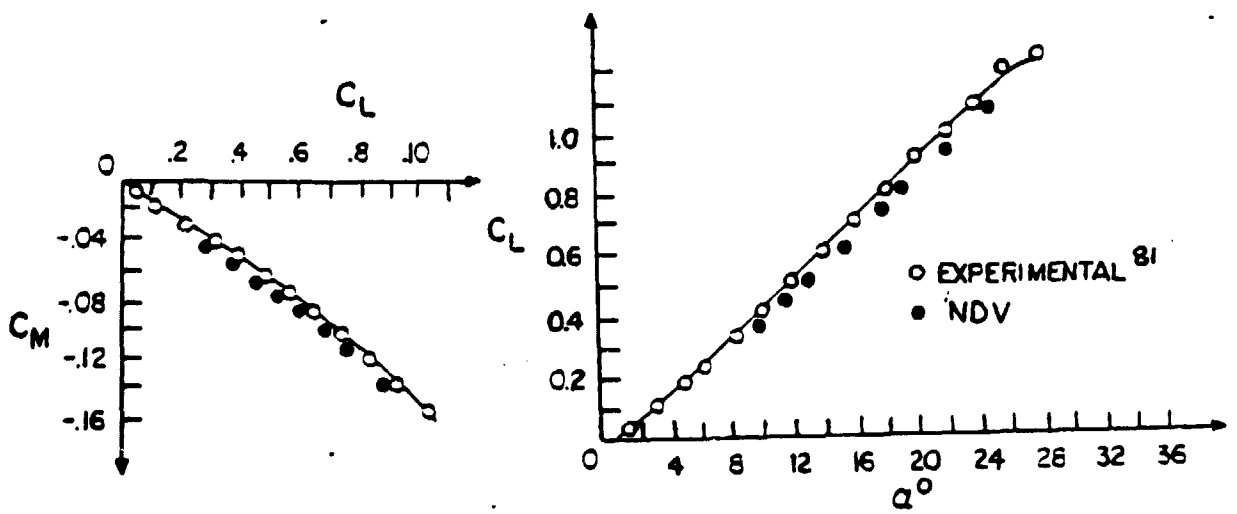

Figure 19. Lift and pitching-moment coefficients for a wing-body combination, AR=2, f=9.86, 9x9 lattice for wing, 25x16 lattice for body.

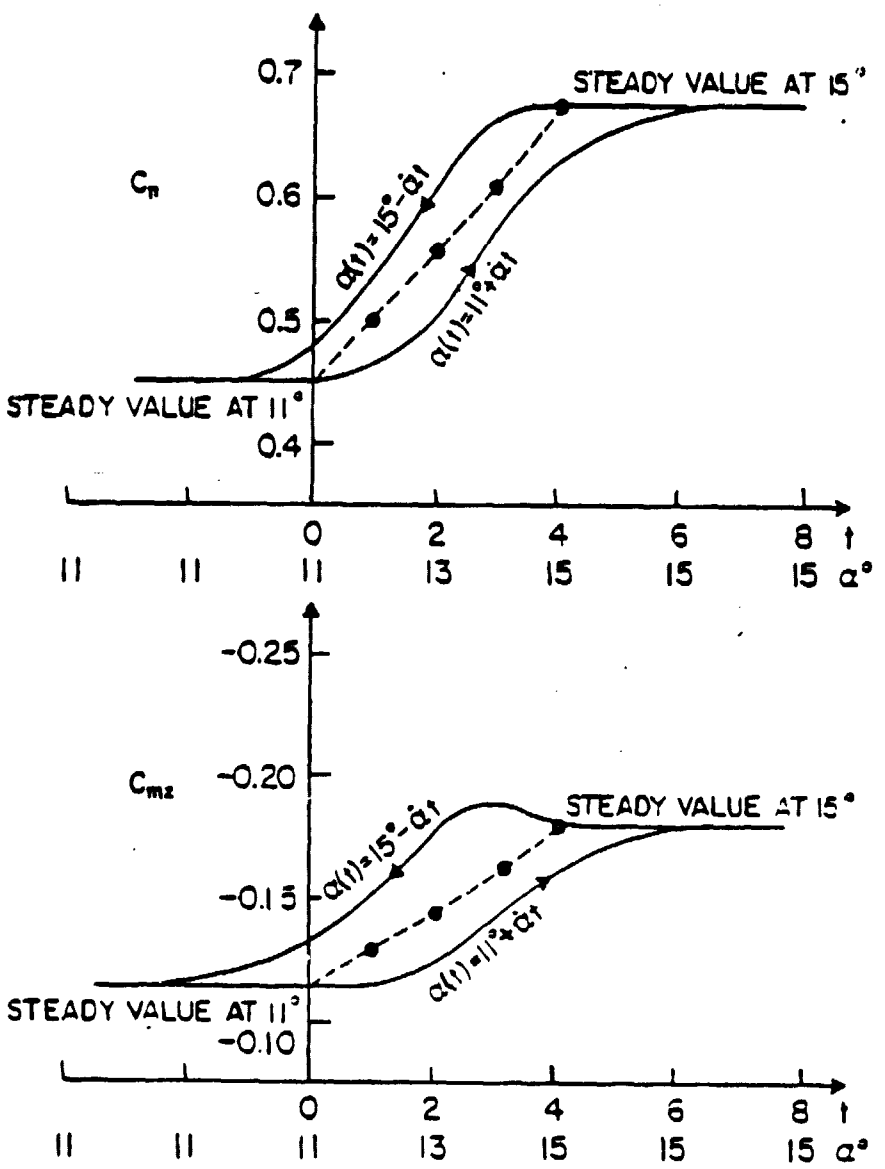

Figure 20. Variation of the normal-force and pitching-moment coefficients with increasing and decreasing angle of attack, rectangular wing, AR=1, α=1, 4x4 lattice, NDV-method.

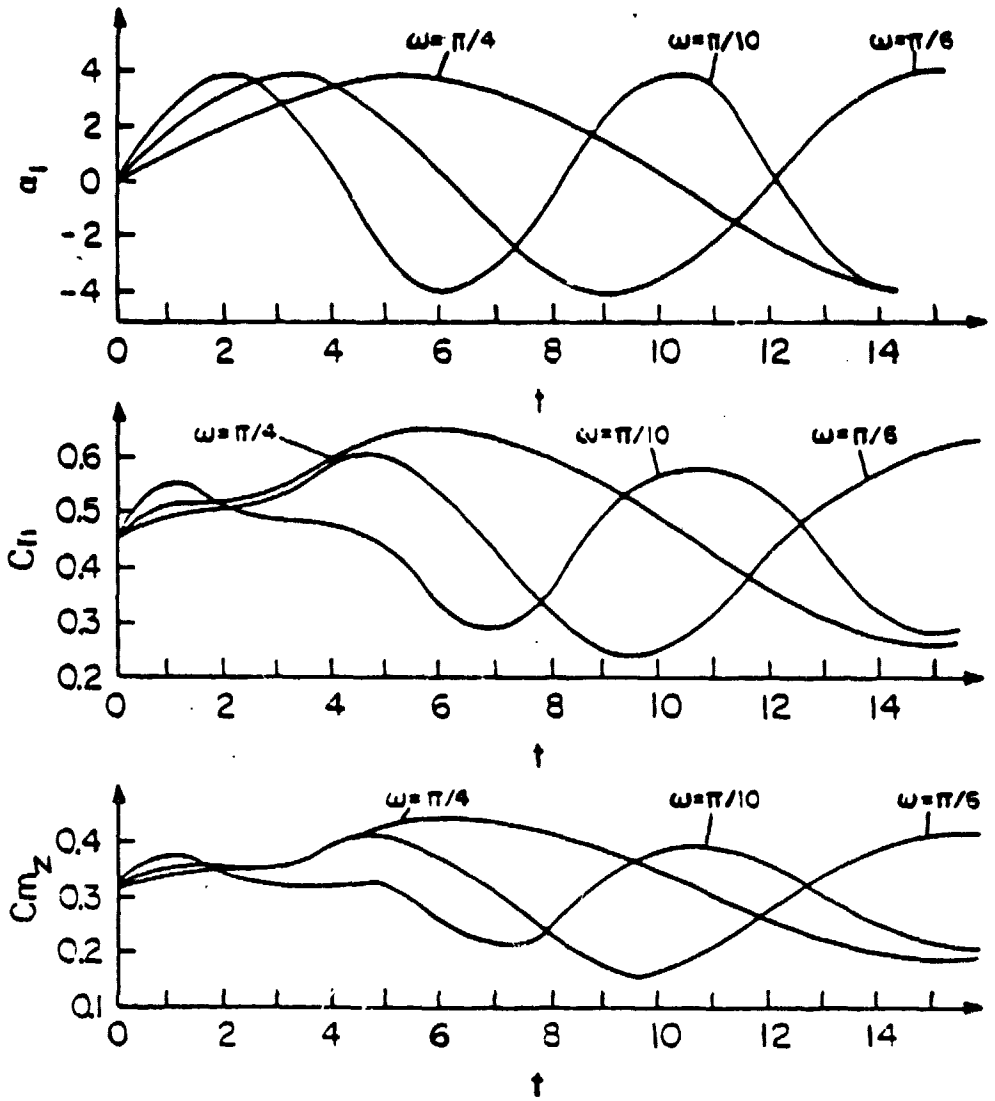

Figure 21. Variation of the pitching-moment and normal-force coefficients for a delta wing in pitching oscillation, AR=1, $\alpha=15°+4 \sin \omega t$, 4x4 lattice, NDV-method.

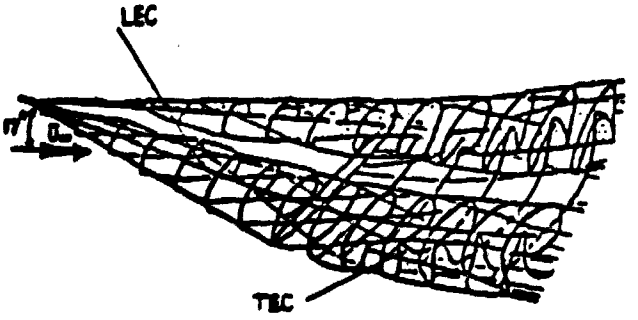

Figure 22. Typical solution of the leading- and trailing-edge vortex sheets, AR = 1, 7 x 7 lattice, NOV-Method.

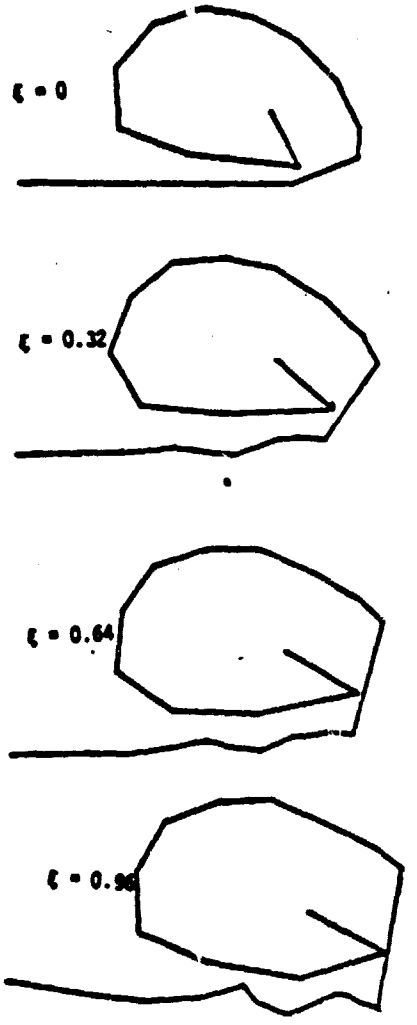

Figure 23. Leading- and trailing-edge sheets behind a delta wing in planes perpendicular to the wind direction, AR = 1, $\alpha = 17^0$, 7 x 7 lattice, NOV-Method, $\xi = x/b$ (origin at T.E.)

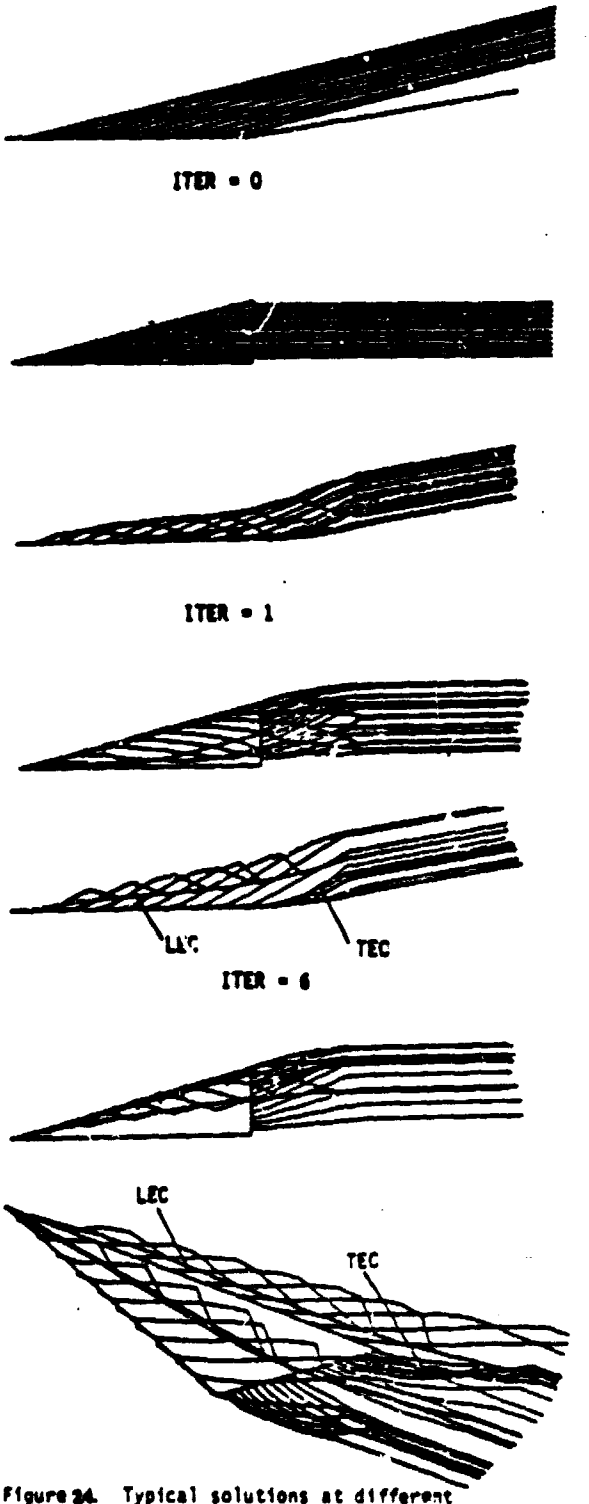

Figure 24. Typical solutions at different iteration steps; ITER = 6 is the converged solution showing the leading- and trailing-edge cores in two- and three-dimensional views; AR = 1, $\alpha = 20.5^0$, 10 x 10 lattice, 1/4 turn, NMOV-Method.

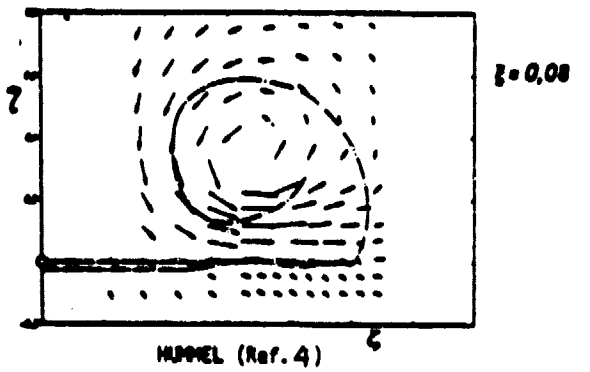

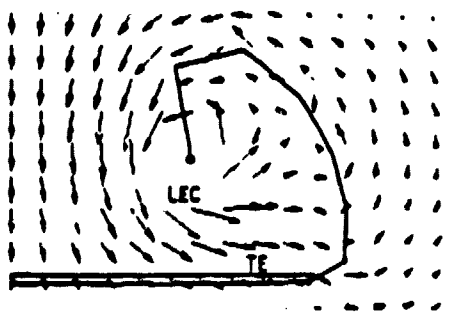

12 x 12 lattice, 1/4 turn

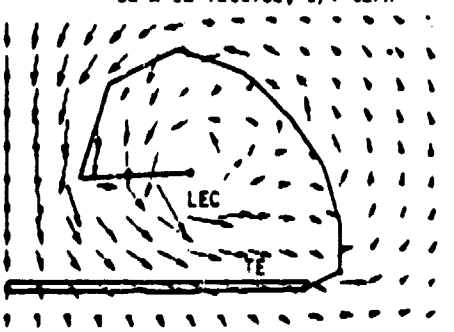

12 x 12 lattice, 1/2 turn

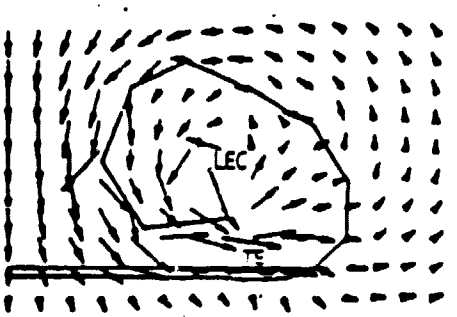

12 x 12 lattice, 3/4 turn

Figure 25. Leading- and trailing-edge sheets and flow direction in a plane perpendicular to the wind direction with different turns, AR = 1, α = 20.5°, ζ = 0.08, $|\overline{V_{zy}}/U_\infty| = 1$, MNDV-METHOD.

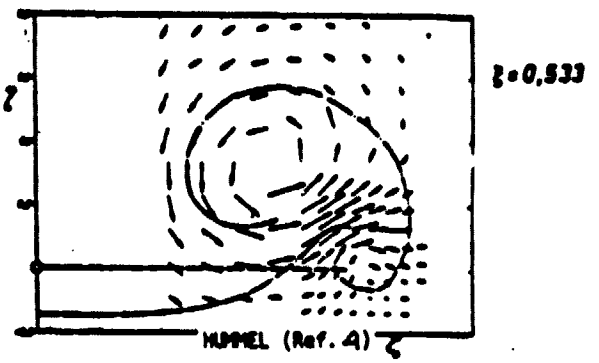

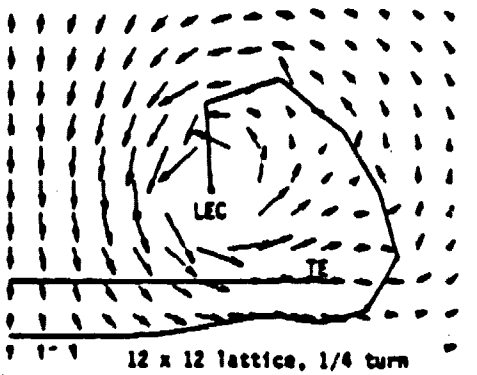

12 x 12 lattice, 1/4 turn

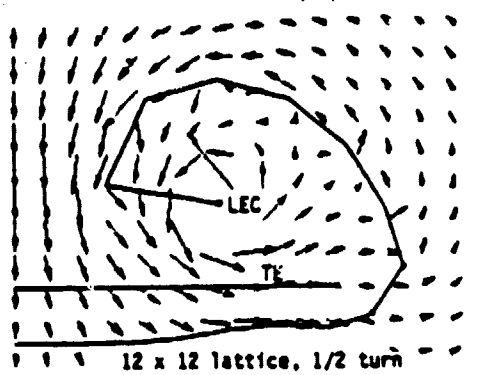

12 x 12 lattice, 1/2 turn

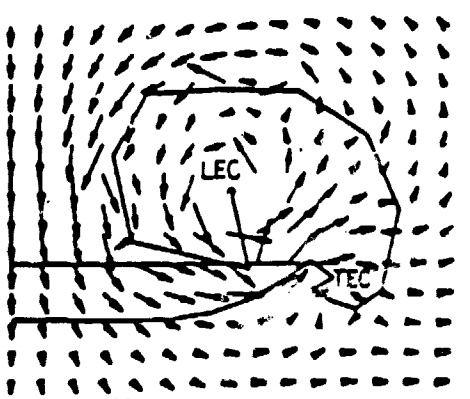

12 x 12 lattice, 3/4 turn

Figure 26. Leading- and trailing-edge sheets and flow direction in a plane perpendicular to the wind direction with different turns, AR = 1, α = 20.5°, ζ = 0.5333, MNDV-METHOD.

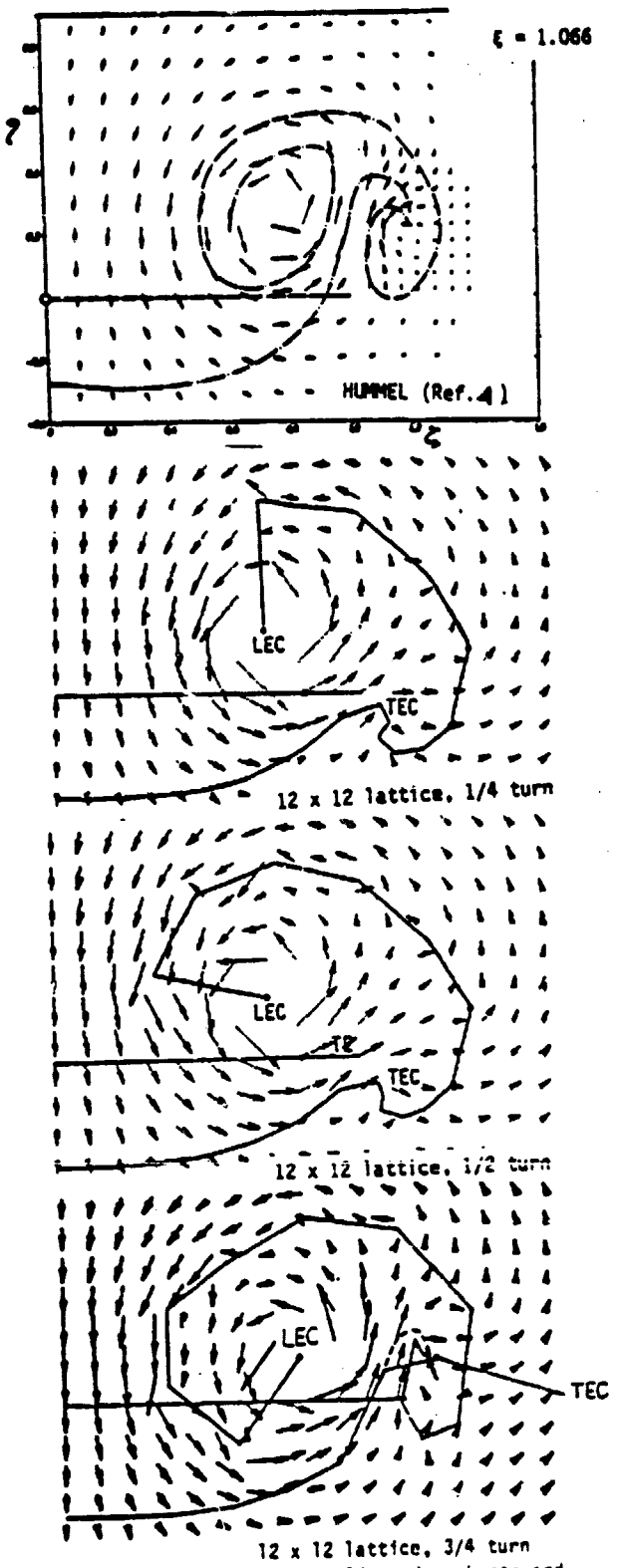

Figure 27. Leading- and trailing-edge sheets and flow direction in a plane perpendicular to the wind direction with different turns AR = 1, $\alpha = 20.5^{\circ}$, $\varepsilon = 1.066$, MNDV-METHOD.

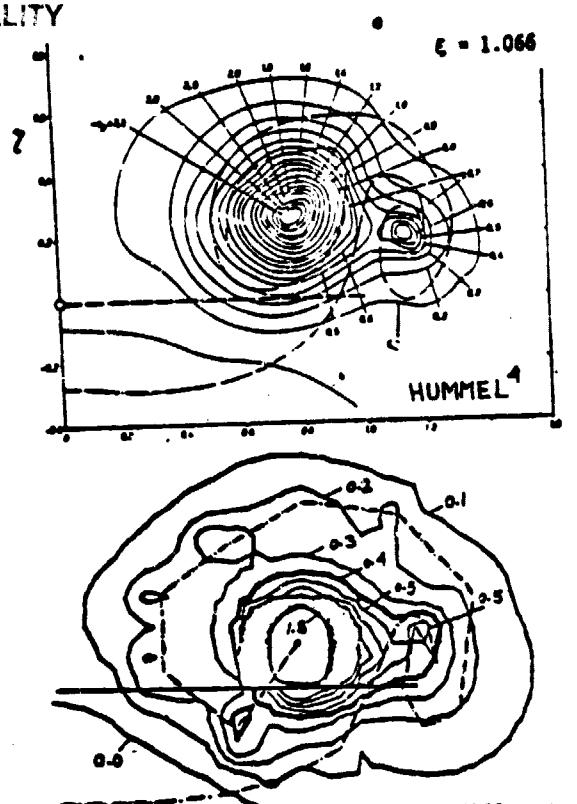

Figure 28. Static pressure contours in different planes perpendicular to the wind direction, AR = 1, $\alpha = 20.5^{\circ}$, 12 x 12 lattice, 3/4 turn, MNDV-METHOD.

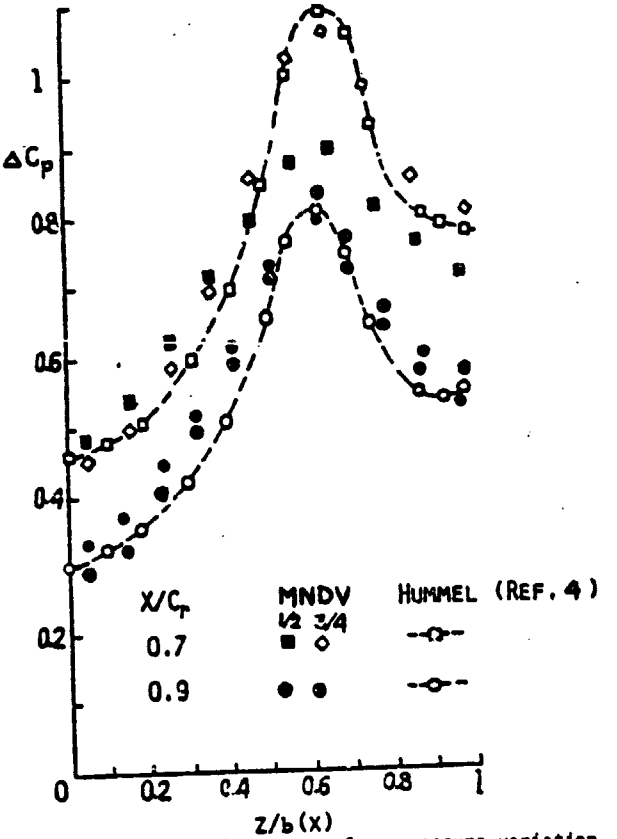

Figure 29. Spanwise net surface pressure variation, $\alpha = 20.5^{\circ}$, 12 x 12 lattice.

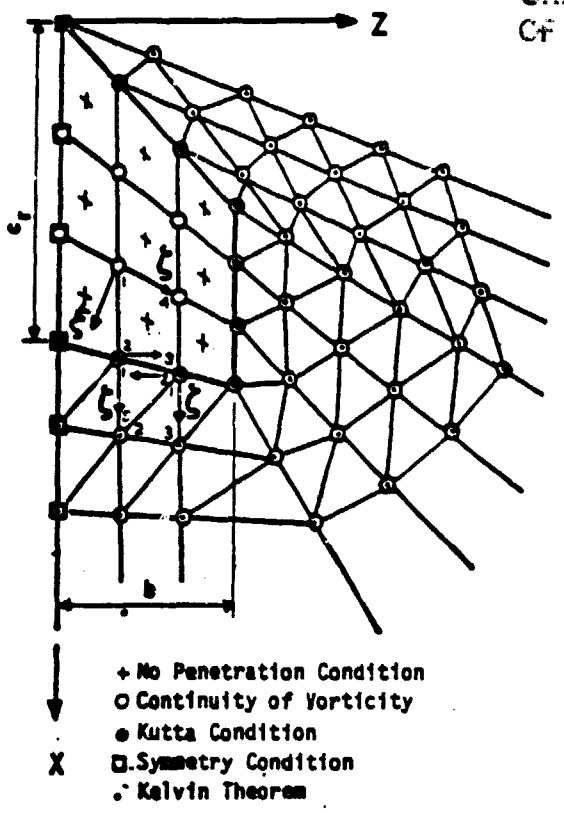

Figure 30. Boundary Conditions and Arrangement of Bound- and Free-Vortex Panels, NHV-METHOD.

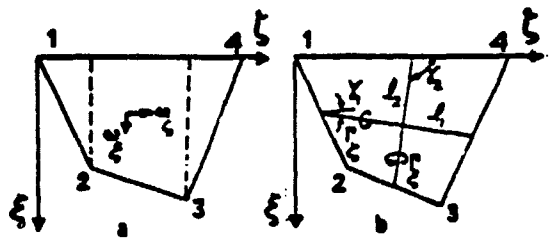

a. Quadrilateral Panel With Distributed Vorticity for the Near-Field Calculations

b. Equivalent Concentrated Vortex Lines for the Far-Field Calculations

Figure 31. Quadrilateral Vortex Panel Used on the Bound-Vortex Sheet

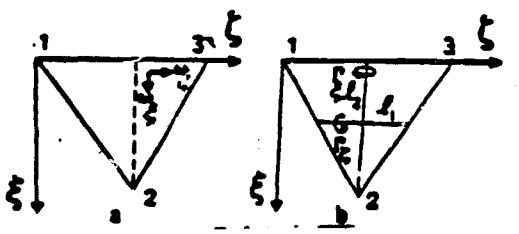

a. Triangular Panel With Distributed Vorticity for the Near-Field Calculations

b. Equivalent Concentrated Vortex Lines for the Far-Field Calculations

Figure 32. Triangular Vortex Panel Used on the Free-Vortex Sheet

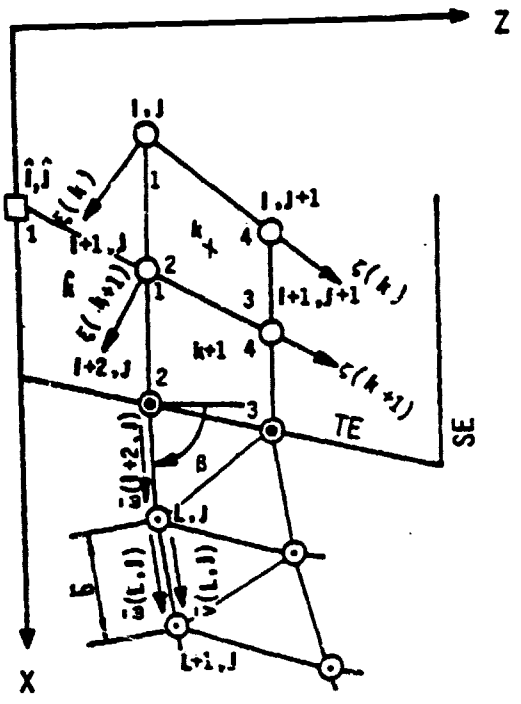

+ No-Penetration Condition
○ Continuity of Vorticity Condition
● Kutta Condition
□ Symmetry Condition
• Kinematic and Dynamic Conditions

Figure 33. Details of the Boundary Conditions for the Steady-Flow Problem.

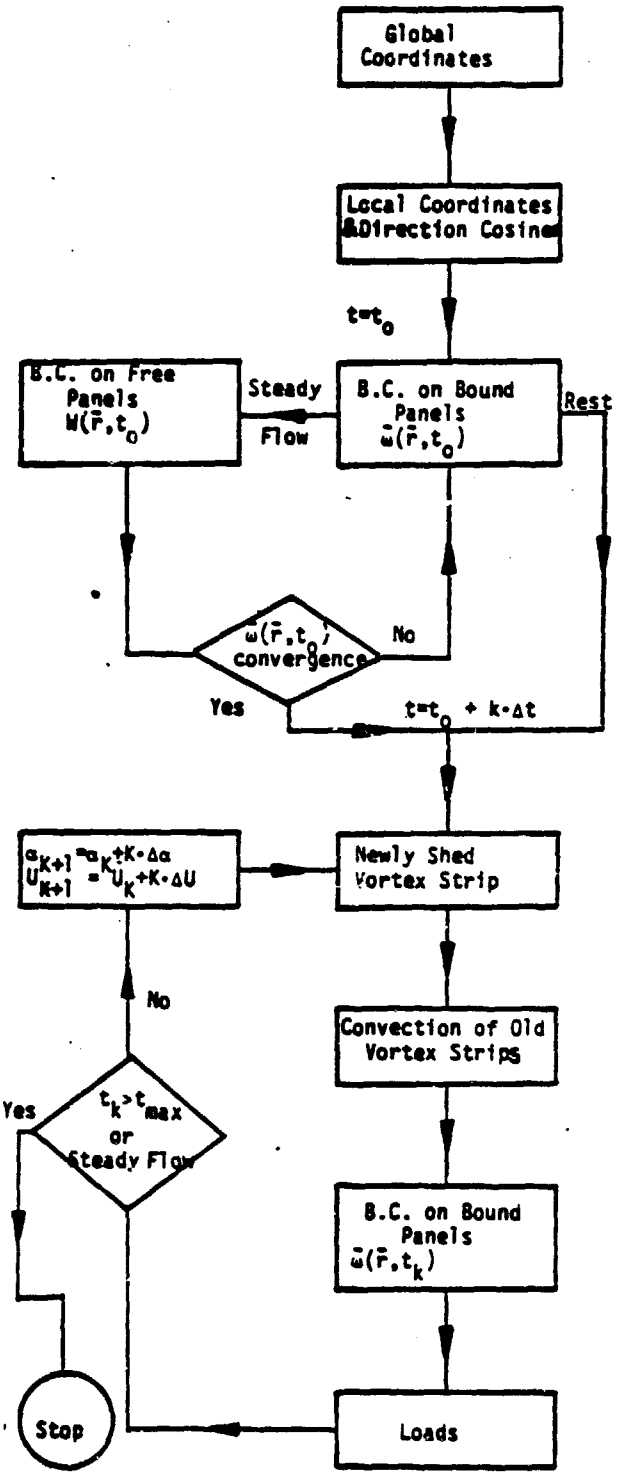

Figure 34. Flow Chart of the Computer Program For the Steady and Unsteady (Time Domain Approach) Flow Problems, NHV-METHOD.

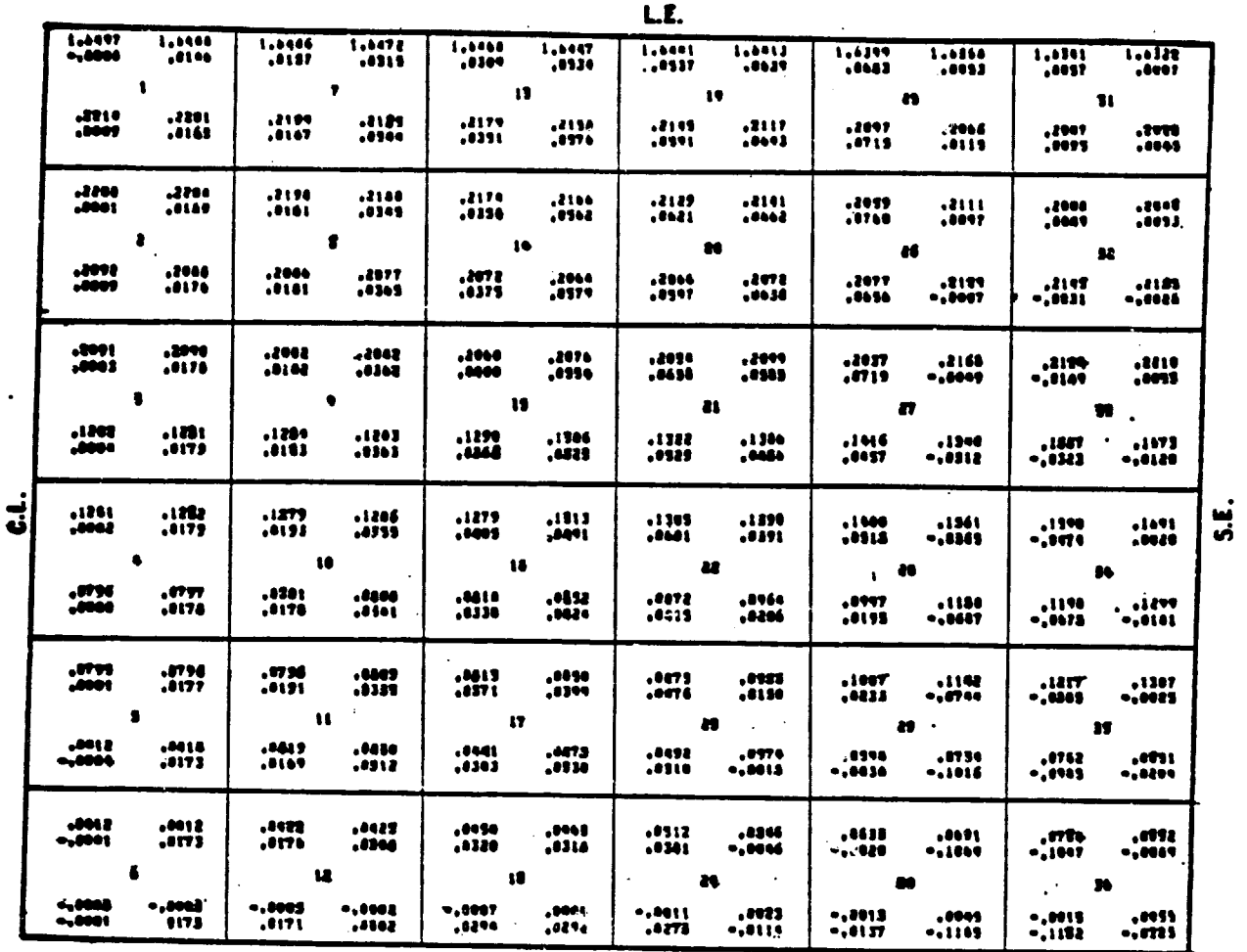

Figure 35. Typical Solution of Vorticity Distribution on the Wing, AR = 1, α = 9.7°, 6 x 6 panels.

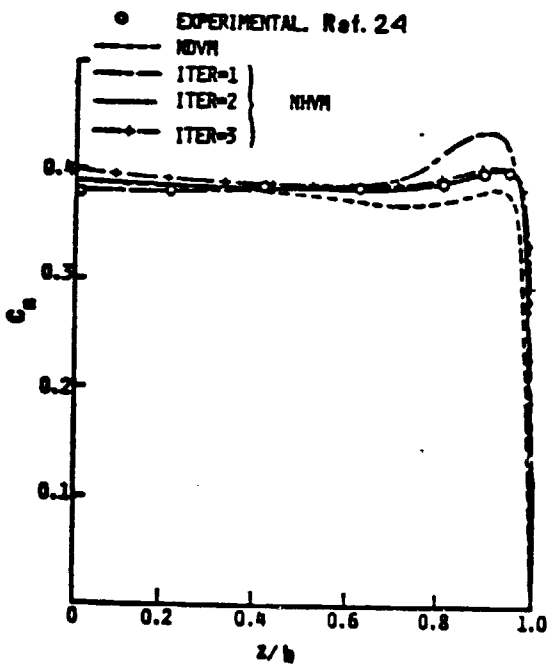

Figure 36. Spanwise variation of the section normal-force coefficient for a rectangular wing at 3 iteration steps, AR = 1, α = 9.7°, 6 x 6 panels.

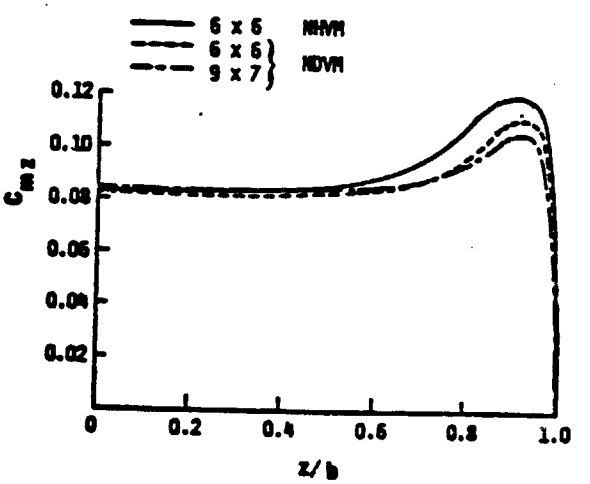

Figure 37. Spanwise variation of the pitching moment coefficient for a rectangular wing. AR = 1, α = 9.7°, 6 x 6 panels.

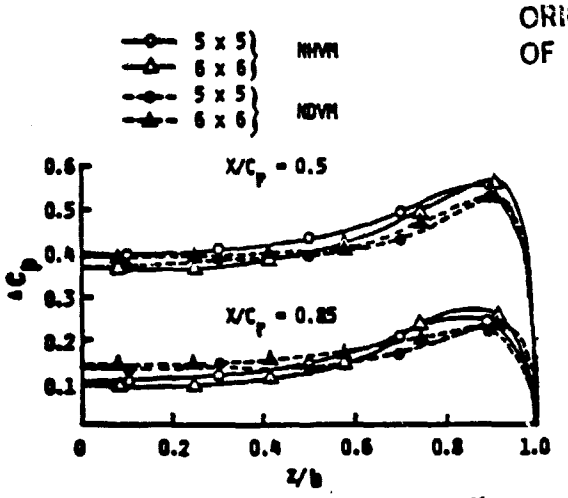

Figure 38. Spanwise variation of net pressure at different chordwise stations for a rectangular wing, AR = 1, α = 15°, 5 x 5 and 6 x 6 panels

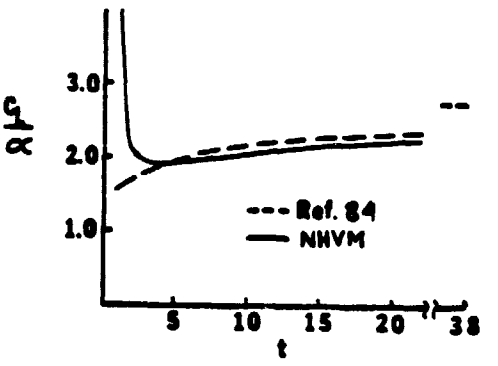

Figure 40. Growth of Indicial Lift for a Rectangular Wing, AR=3, α=5°, 5x5 Bound Panels, zero Thickness, No Tip Separation.

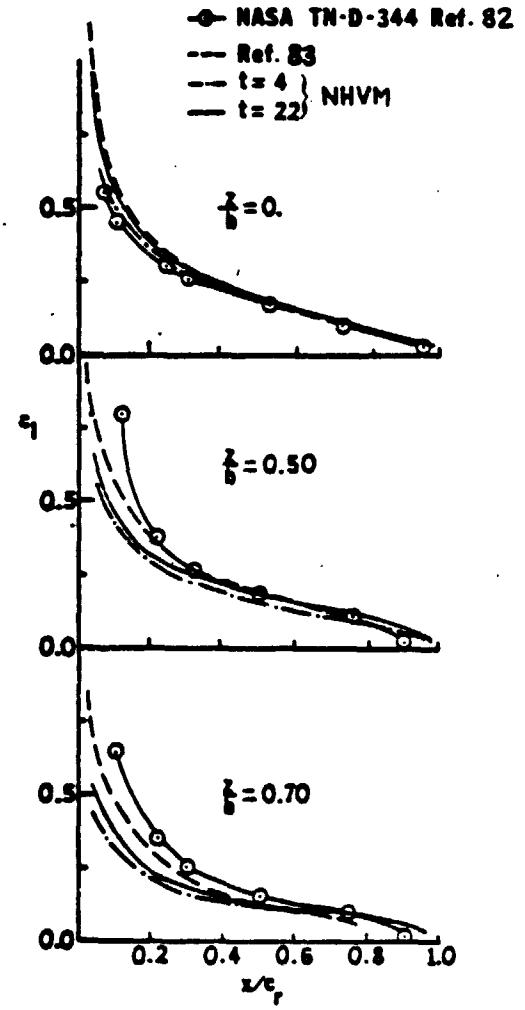

Figure 39. Chordwise Variation of the Lift Coefficient at Various Spanwise Stations for a Rectangular Wing, AR=3, α=5° 5x5 Bound Panels, zero thickness. No Tip Separation.

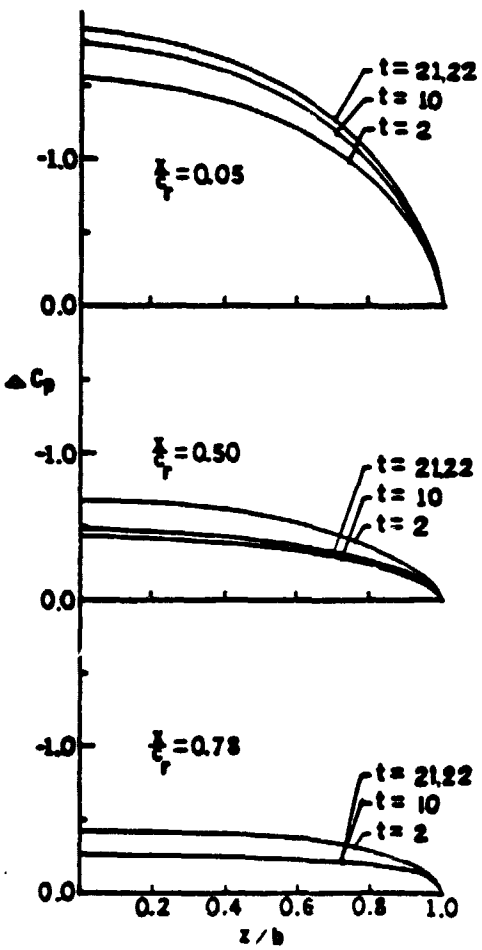

Figure 41. Spanwise Variation of net pressure coefficient at different chordwise station for a Rectangular Wing, AR=2, α=20.5°, 5x5 Bound Panels, zero-Thickness, No Tip Separation.